ELECTROCHEMICAL ANALYSIS SUPPORTED BY MACRO AND MICROELECTRODE ARRAY

DELCOURT-LANCON, ALICE

Durham University

ELECTROCHEMICAL ANALYSIS SUPPORTED BY MACRO AND MICROELECTRODE ARRAY

ALICE DELCOURT LANÇON

Ph.D Thesis *2011*

ABSTRACT

The purpose of this project was to investigate cyclic voltammetry (CV) and electrochemical impedance spectroscopy (EIS) analytical techniques for enantioselective sensing at both a macroelectrode and a microelectrode array. The scale of the electrochemical cell was reduced from macro to micro dimensions to improve both the electroanalytical detection and the efficient use of chemicals. A microdevice was fabricated using photolithography and plasma bonding and consisting of a microelectrode array (MEA) of 306 microelectrodes, each with a diameter of 45 µm supported by a polydimethylsiloxane (PDMS) slab engraved with microfluidic channels. The electroanalytical performances of the microdevice were characterised using cyclic voltammetry and it was established that the metallisation process influenced the surface roughness of the electrode, and also affected the final response of the array. The microdevice was used for flow injection analysis using chronoamperometry and provided the capability to detect small changes of analyte concentration. The selective electro-oxidation of phenylethanol catalysed by TEMPO and (-)-sparteine at a macroelectrode and MEA was investigated. The CV analysis showed a reproducible selective oxidation in favour of the (-)-phenylethanol enantiomer. The performances of the electrodes were enhanced to improve their enantioselective capability, and to extend their application to biosensors by functionalising their surface with Self-Assembled Monolayers (SAM). The electrodes were modified with glutathione and cysteine chiral molecules to investigate their ability to recognise the proline enantiomers using EIS analysis. The electron transfer rate of the ferricyanide analyte at the cysteine monolayer was less in the presence of D-proline than it was in the presence of L-proline, indicating the selective penetration of the enantiomer through the monolayer. The properties of the macroelectrode and MEA were extended to biological applications by modifying their surfaces with thiolated single stranded DNA.

ACKNOWLEDGMENTS

Thank you to my supervisors Dr. Ritu Kataky and Prof. David Wood.

Thank you Ritu for your precious scientific contribution, your rich creativity,
your kindness and your personal support.

Thank you David for having driven me to put it all together.
your consistency and methodology made it all happen.

Thank you Andrew for your training and help in the cleanroom.

Thank you to both, Sensor Group in the Department of Chemistry
and MEMS Group in the School of Engineering and Computing Sciences.
In particular, thank you to Paula and Rui, it was my luck to work with friends;
and to Belen, Rachael, Francesco, Darius, Mark and Linzi
for making work easier and enjoyable.

Thank you Jens Thies for having put me in the right place at the right moment.
Thank you Patrick Vrijaldenhoven for having being “ze” best teacher
confirming my interest for chemistry and research.

Thank you to all my friends, from Germany and everywhere,
who have always been supportive wherever I was :o)
Merci la famille et les amis pour votre présence et soutien.

DECLARATION

The research described in this thesis was undertaken in the Department of Chemistry of Durham University between October 2007 and September 2011. All work is my own, other than where stated otherwise. No part of this work has been submitted previously for a degree at this or any other university.

STATEMENT OF COPYRIGHT

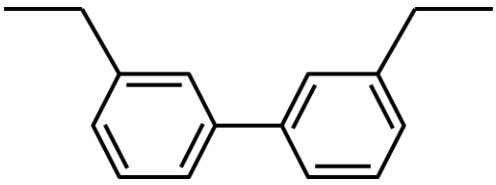

Celle là on dirait une paire de lunettes ☺

TABLE OF CONTENTS

TABLE OF FIGURES

ABBREVIATIONS

AFM	Atomic force microscopy
CV	Cyclic voltammetry
DNA	Deoxiribonucleic acid
ee	Enantiomeric excess
EIS	Electrochamical impedance spectroscopy
FIA	Flow injection analysis
GSH	Reduced glutathione
MEA	Microelectrode array
PAA	Polyacrylic acid
PBS	Phosphate buffer solution
PE	Phenyl ethanol
PEDOT	Poly 3,4-ethylenedioxythiophene
Ppy	Polypyridine
PRODOT	Poly 3,4-propylenedioxythiophene
SAM	Self-assembled monolayer
SEM	Scanning electron microscopy
SS	Steady state
TEMPO	2,2,6,6-tetramethylpiperidine-1-oxyl
WSC	Water-soluble carbodiimide

1. General Introduction

Enantiomers share the same atomic structure and atomic sequence. They only differ in their spatial organisation at their chiral centre (asymmetric centre). These differences make them interact differently towards other chiral compounds such as the chiral receptors of the human body. If one compound can cure a disease, its enantiomer may be inactive or even have a different effect, including undesirable side effects. In the most general case, enantiomers result from the same chemical synthesis where they are produced simultaneously. Hence the separation and detection of enantiomer purity is of great importance in the pharmaceutical industry and can be costly and resource intensive due to the similarity between the molecules. Well known analytical techniques, such as HPLC (high performance liquid chromatography) or NMR (nuclear magnetic resonance), require in-line sampling and are destructive and time consuming.

Electroanalytical techniques allow in-situ analysis with continuous monitoring. Cyclic voltammetry and chronoamperometry consist of characterising an electro-active species by the current it produces under potential. Electrochemical impedance spectroscopy (EIS) allows the study of the resistance and capacitance at the electrode surface. These techniques can be enantioselective when they are performed in the presence of chiral molecules, which interact selectively with one enantiomer and generate different current response for the enantiomers. The chiral molecule can be in bulk solution or immobilised at the electrode surface.

Furthermore, the electroanalysis allows miniaturisation of the electrochemical cell by reducing the size of the electrodes from macro to micro (micrometre scale). Using microelectrodes allows saving space, materials and chemicals while getting a better sensitivity in the measurements.

The ultimate aim of this project is to produce microelectrode arrays for industrial, biological and pharmaceutical applications, using electroanalytical techniques. The use of microelectrode arrays in electrochemistry is well established; extending the systems to chemical and biochemical chiral detection requires both innovative chemistry and engineering. The key problem of this research is to find the appropriate chiral agent to obtain enantioselectivity at the surface of the electrode. Whether it is in situ or immobilised at the surface of the electrode, the chiral agent must have time to interact selectively with one of the enantiomers and affect its electrooxidation rate. Furthermore, the selectivity should be significant to be applicable to industrial synthesis and efficiently probe chiral purity. Finally, the immobilisation of molecule at the surface of the electrode is more complex when the scale of the electrode is reduced from macro to micro. The modified surface should remain robust enough to support reliable and reproducible electroanalysis.

The enantioselective sensing was investigated using a chiral catalyst in bulk solution and immobilised at the surface of the electrode. In the first case, cyclic voltammetry analysis was used to detect the enantioselectivity of the phenylethanol oxidation in the presence of a radical nitroxyl catalyst (2,2,6,6-tetramethylpiperidine-1-oxyl) and a proton abstractor (sparteine) in solution. Additionally, impedance analysis was used to detect proline enantiomers at the surface of electrodes modified by a self-assembled monolayer, where the chiral molecules tested were glutathione and cysteine.

Concurrently, a microdevice consisting of a microelectrode array and microfluidic channels was developed as an alternative to a macroelectrode in order to optimise the electrochemical analysis. The microdevice was designed and fabricated in the cleanroom using photolithography techniques. The microfluidic channels were added to the microelectrode array in order to extend the competence of the device from sampling analyses (cyclic voltammetry, impedance) to inflow analysis such as chronoamperometry. Furthermore, the use of a microdevice is of great interest for analysis in biological applications where the sampling quantities have to be minimal, and so the possibility of DNA surface modification of the microelectrode was also investigated as a first step toward future work.

This project involved collaboration between the School of Engineering and Computing Sciences, where the microdevice was developed, and the Department of Chemistry, where it was tested alongside the macroelectrode, for cyclic voltammetry, chronoamperometry and impedance analysis. The following thesis presents the work achieved from the electrode design to its final application for electroanalysis.

The literature review and theory relative to the chemistry of this project are presented in Chapter 2, followed by a detailed description of the experimental protocol. Chapter 4 presents the first results and discussion about the enantioselective electro-oxidation of phenylethanol at macro and microelectrodes. The fifth chapter is dedicated to the engineering study and presents the theory, the experimental protocol and the results and discussion behind the microdevice fabrication and characterisation. Finally the last chapter describes the attempt of modifying the electrode surfaces to make them capable of chiral recognition and to enlarge their field of application.

2. TECHNICAL BACKGROUND AND LITERATURE REVIEW

This chapter presents the theory and the literature review relevant to the electrochemical sensing of chirality. At first, the basis of electrochemistry is presented along with the three analytical techniques used in this study: cyclic voltammetry, chronoamperometry and electrochemical impedance spectrometry. Then the notion of chirality is explained followed by the details of the phenylethanol electro-oxidation and the concept of a self-assembled monolayer for chiral sensing.

2.1. ELECTROANALYTICAL CHEMISTRY

2.1.1. Electrochemistry

The first experiments in electrochemistry date from the late 18th century when the Italian Luigi Galvani established the first relation between chemical reactions and electricity in his essay "De viribus electricitatis in motu musculari commentarius" which discusses the effect of electricity on muscular motion. Alessandro Volta rejected the Galvani idea of an "animal electric fluid" and, during his investigations, he elaborated the first electrochemical cell: the "voltaic piles". In 1800, William Nicholson and Johann Wilhelm Ritter succeeded in decomposing water into hydrogen and oxygen by electrolysis. Walther Hermann Nernst developed the theory of the electromotive force of the voltaic cell in 1888. In 1889, he showed how the characteristics of the current produced could be used to calculate the free energy change in the chemical reaction producing the current.

An electrochemical reaction[1-4] involves a transfer of charge via an electron or ion. A redox reaction implies the transfer of at least one electron from a chemical species to another one and induces the change of oxidation state of the species. This reaction can occur through the application of an external voltage or through the natural release of chemical energy. The process of redox reaction follows Faraday's law which states that the quantity of reacted species is directly proportional to the current passing through the cell. The two processes involved in a redox reaction are the oxidation, where the species loses electrons, and reduction, where it gains electrons:

Reduction: $\text{Oxidant} + e^- \longrightarrow \text{Product}$

Oxidation: $\text{Reductant} \longrightarrow \text{Product} + e^-$

Reactions are homogeneous when both media losing and gaining electrons are in the same phases (most commonly liquid). Reactions are heterogeneous when the reagent species are in different phases. The most common heterogeneous processes concern charge transfer between solid and liquid; in this case the redox reaction takes place at the solid/liquid interface.

An electrochemical cell which produces an electric current from energy released by a spontaneous redox reaction is a Galvanic cell (Fig. 1). When the reaction doesn't happen spontaneously but requires a potential supply, the electrochemical cell is called an electrolytic cell. Redox active chemicals are called analytes (Cu^{2+} and Zn^{2+}in Fig. 1) and are supported by the electrolyte (SO_4^{2-} and Na^{+} in Fig. 1) which consists of free non-reactive ions behaving as an electrically conductive medium.

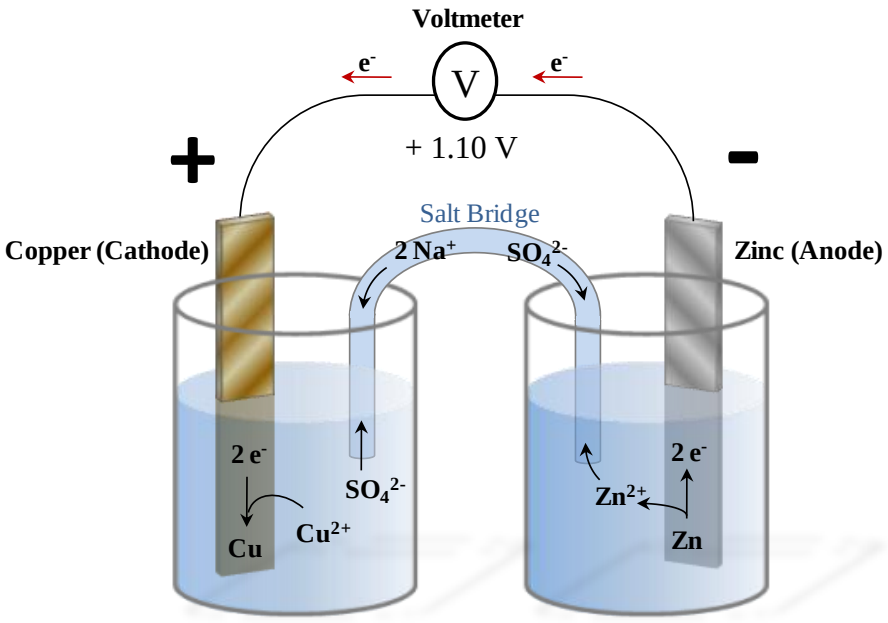

$Cu^{2+} + 2\ e^- \rightarrow Cu_{(s)}$ **+ 0.34 V** $\quad Zn_{(s)} \rightarrow Zn^{2+} + 2\ e^-$ **+ 0.76 V**

$$Cu^{2+} + Zn_{(s)} \longrightarrow Cu_{(s)} + Zn^{2+}$$

Fig. 1. Galvanic cell $Zn(s) \mid Zn^{2+}(aq) \parallel Cu^{2+}(aq) \mid Cu(s)$.

2.1.2. Electrode/Solution Interface

Interactions between solid and liquid electrolyte differ from interactions in a homogeneous liquid cell. Applying a potential to the electrodes would increase those differences because of the influence of the charge held at the electrode. The strong interactions between the molecules in solution and the electrode surface result in the formation of the electrical double layer[2,5]. Many attempts have been performed to model this double layer; the last one is presented in Fig. 2. Charges are immobilised on a surface because of complexion, adsorption or dissociation. To get back to a neutral interface, counterions attracted to the surface by electrostatics shield the surface charge. The counterions are not all in the same plane, however, because they are held in a dynamic balance by electrostatic attraction and the tendency to diffuse away. The concentration of ions in the diffusion layer decrease with distance from the surface. Thus the surface charge forms one layer and the diffuse shielding charge forms the other layer. This organisation is the basis of the electrical double layer.

The double layer has a certain structure:

- The Inner Helmholtz Plane (IHP) is the plane cutting through the centre of the adsorbed species.
- The Outer Helmholtz plane (OHP) is the plane cutting through the counterions at their position of closest approach.

Ions in the diffuse layer are always being exchanged at the surface, but the surface excess of counterions only exactly balances the total charge associated with the solid.

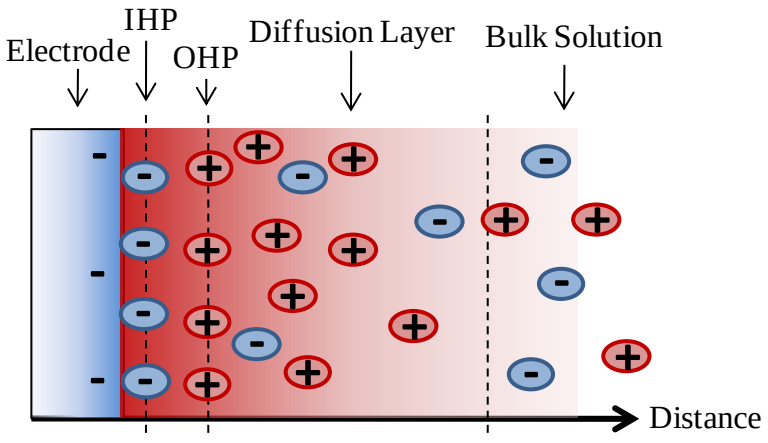

Fig. 2. Electrical double layer model.

The rate of the reaction depends on the slowest steps of the process. The kinetic of the reaction can be controlled by the **mass transport** step, where the reactant reaches (or the product leaves) the electrode surface, or by the electrode kinetics, where the heterogeneous electron transfer happens at the electrical double layer.

Mass transport

When the reaction is mass transport-limited, the rate of the reaction, *v*, is governed totally by the flux (*J*) at which the reagent is brought to the surface from the bulk solution, Eq. 1.

Eq. 1. $$J(x,t) = -\frac{i}{zFA}$$

where *J(x,t)* is the flux of species brought to the surface from the bulk solution ($mol.cm^{-2}.s^{-1}$), *i* is the current (A), *z* is the number of electrons involved in the reaction, *F* is the Faraday constant (96484.6 $C.mol^{-1}$) and *A* is the electrode area (cm^2).

There are three forms of mass transport which can influence an electrolysis reaction kinetic:

- Diffusion
- Convection
- Migration

Diffusion happens in all solutions where there is a gradient of concentration. Entropic forces act to even the concentration distribution. Diffusion is the main driving force in the electrolysis process as the reaction occurs only at the electrode surface and so provokes a rise in concentration at the interface.

Natural **convection** is generated by a thermal or density gradient and acts to mix the solution in a random way. Convection phenomena can be controlled by introducing artificial convection forces, using a rotating disc or stirrer for example.

Migration is essentially an electrostatic effect. When a potential is applied to the electrodes, the interface becomes charged and any charged species near that interface will be either attracted or repelled from it by electrostatic forces. However, because of the ion solvation effects and the diffuse layer interactions in solution, the migration is very difficult to calculate.

Taking those three processes in account, the rate of mass transport is described by the Nernst-Planck equation (Eq. 2).

Eq. 2
$$J(x,t) = \underbrace{-D\frac{\partial C(x,t)}{\partial x}}_{\text{Diffusion}} \underbrace{-\frac{zFDC_{\infty}}{RT}\frac{\partial \theta(x,t)}{\partial x}}_{\text{Migration}} \underbrace{+C(x,t)V(x,t)}_{\text{Convection}}$$

where D is the diffusion coefficient ($m^2.s^{-1}$), R is the ideal gas constant (8.314 $J.K^{-1}.mol^{-1}$), T is the temperature (K), C is the concentration of reagent ($mol.L^{-1}$), V is the velocity of the solution, $\frac{\partial \theta(x,t)}{\partial x}$ is the potential gradient in solution and $\frac{\partial C(x,t)}{\partial x}$ is the concentration gradient.

As illustrated in Eq. 2, the situation becomes very complex when the three processes - migration, convection and diffusion - happen simultaneously. To simplify the situation during electroanalysis, a strong supporting electrolyte is added to the media and the solution remains unstirred so that the migration and the convection processes can be considered negligible in comparison to the diffusion effect. The kinetic of the reaction is then limited by the diffusion process, based on concentration gradients, and Eq. 3 can be simplified to become the first Fick's law:

Eq. 3
$$J(x,t) = -D\frac{\partial C(x,t)}{\partial x}$$

The current resulting from an oxidation can be expressed as a function of the concentration gradient by combining Eq. 1 and Eq. 3.

Eq. 4
$$i = zFAD\frac{\partial C(x,t)}{\partial x}$$

2.1.3. Electroanalytical Chemistry

Quantitative and qualitative analysis can be performed in the following two ways:

Potentiometry

In potentiometry, no external potential is applied and no current flow occurs. The voltage measured results from the difference in free Gibbs energy ($\Delta G = -zF\Delta E$) of the electrons in equilibrium between the two half-cells. This difference is called the electrode potential difference, or the redox potential difference. The set up to perform potentiometry consists of 2 electrodes; the working electrode and the reference electrode.

Voltammetry

This technique consists on applying a controlled external potential (or current) to the cell and measuring the resulting flow current (or potential)[5]. Voltammetry techniques can be divided in two categories, the potential sweep techniques (e.g. cyclic voltammetry), where the potential of the working electrode is linearly scanned, and the step or pulse techniques (e.g. chronoamperometry), where the potential is stepped, allowing removal of the capacitive current. The set up is composed of 3 electrodes; the working electrode, the reference electrode and the counter electrode. The potential applied to the working electrode is controlled with respect to the reference electrode. The redox reaction takes place at the surface of the working electrode and the current passes between the working electrode and the counter electrode. A two electrodes system (working + reference) can be used in the case of measuring very small currents that do not perturb the potential of the reference electrode.

2.1.4. Electrodes

The working electrode responds to the target analyte[6]. It exists in various geometries and materials and usually consists of inert metals (e.g. gold, platinum), inert carbon (e.g. glassy carbon, pyrolytic carbon) or a mercury drop. The counter or auxiliary electrode serves merely to carry the current flowing through the cell as no processes of interest occur at its surface. This electrode must have a very large surface area to lower the current density and be made of an inert metal (e.g. gold, platinum).

Voltammetric analyses measure a difference of potentials, and so the potential of the system working/counter electrodes must be measured against a reference electrode, from which a well known potential can eventually be subtracted to have access to the analyte potential. Therefore the reference electrode, ideally non-polarisable, must have a constant potential no matter the species used or their concentrations. The most commonly used standard electrodes are the Standard Hydrogen Electrode (SHE), the silver/silver chloride electrode and the Standard Calomel Electrode (SCE). Pseudo-reference electrodes can alternatively be used.

Standard Hydrogen Electrode

The standard established to measure relative electrode potentials is the Standard Hydrogen Electrode (SHE). Under standard conditions (T = 298 K), the standard electrode potential (H^+ / H_2) is zero. As the hydrogen gas flows over the porous platinum, an equilibrium is set up between hydrogen molecules and hydrogen ions in solution.
The reaction is catalysed by the platinum:

$$2H^+_{(aq)} + 2e^- \rightleftharpoons H_{2(g)}$$

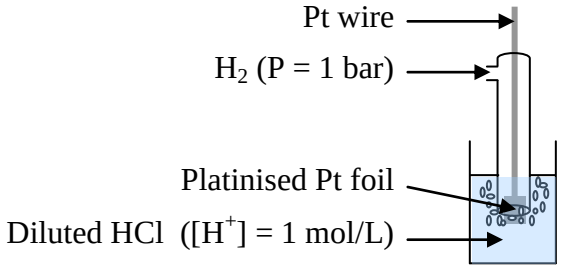

Fig. 3. Standard hydrogen electrode.

Silver/Silver Chloride Reference Electrode

The silver/silver chloride electrode is much easier to handle than the SHE. It consists of a silver wire, coated with silver chloride, which is immersed in a saturated potassium (or sodium) chloride solution. A porous frit is used for the junction between the reference electrode solution and the sample solution.The redox process for this electrode is:

$$AgCl_{(aq)} + e^- \rightleftharpoons Ag_{(s)} + Cl^-_{(aq)} \qquad \text{Potential vs. SHE, } E^0 = 0.22 \text{ V}$$

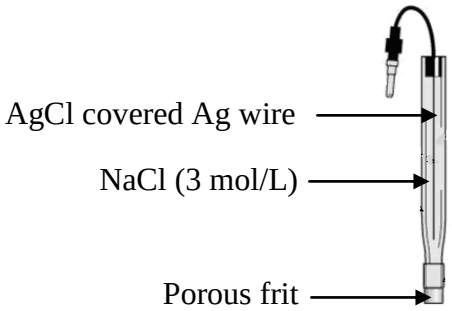

Fig. 4. Silver/silver chloride reference electrode.

Standard Calomel Electrode (SCE)

The calomel electrode is comparable to the silver/silver chloride electrode, with mercury replacing the silver. It was also commonly used as a reference electrode before mercury was judged to be too toxic.

$$Hg_2Cl_{2\,(s)} + 2e^- \rightleftharpoons 2Hg_{(aq)} + 2Cl^-_{(aq)}$$

Pseudo-Reference Electrodes

Instead of the references electrodes described earlier, pseudo-reference electrodes can be used[7]. They consist of simple metal wires (e.g., platinum or silver) having good inoxidable properties, directly immersed in the sample solution. Although the pseudo-reference potential is unknown, and is dependent on the composition of the sample solution, these electrodes provide a stable reference potential when the samples to analyse are made of the same chemicals. Consequently, redox potentials measured using a pseudo-reference electrode should be quoted relative to the redox potential of the reference compound. The main advantages of pseudo-reference electrodes are their low impedance and their ease of use.

Fig. 5. Different shape of platinum pseudo-reference electrode.

2.1.5. Cyclic Voltammetry

Cyclic voltammetry (CV)[8] belongs to the group of potential sweep techniques and can be employed to study electron transfer kinetics and transport properties of electrolysis reactions. The current is measured as a function of the linear potential applied. As species react at different potentials and with different intensity, the CV enables multiple detections in one measurement (qualitative), and estimation of their concentration in solution (quantitative). The current resulting from the potential application is due to the occurrence of redox reactions in the solution (Faradic current) and to the double layer charging (capacitive current). The current response is plotted as a function of voltage rather than time, unlike potential step measurements. In the case of a reversible reaction, the species is consecutively oxidised and reduced (or vice versa). The voltage is scanned using a triangular waveform shown in Fig. 6:

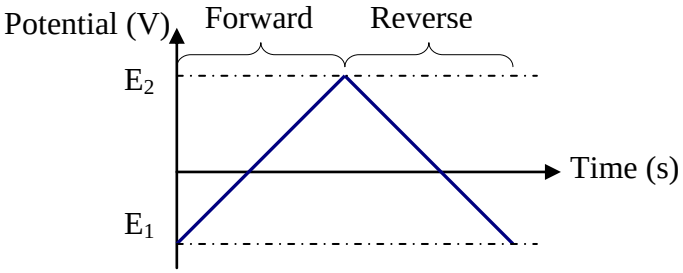

Fig. 6. Potential applied to the cell versus time.

In this case the voltage is swept between two values (see above) at a fixed rate, starting from E_1; when the voltage reaches E_2 the scan is reversed and swept back to E_1. The time taken to sweep the potential range is the voltage scan rate (v), calculated from the slope of $V = f(t)$.

Macroelectrodes

The diffusion layer at the surface of the macroelectrode is linear and the cyclic voltammogram recorded for a reversible electrochemical reaction using macroelectrodes (Fig. 7) can be characterised as follows:

- The ratio of the peak currents at the anode (I_{pa}) and at the cathode (I_{pc}) is equal to one:

$$|I_{pa}/I_{pc}| = 1$$

- The peak currents are proportional to the square root of the scan rate, $\upsilon^{1/2}$, as expressed by the Randles-Sevcik equation:

$$I_{pa} = 0.4463\ zFCA(^{zF\nu D}/_{RT})^{1/2}$$

Which is simplified in:

Eq. 5 $$I_{pa} = 2.69 \times 10^5 z^{3/2} CAD^{1/2} \nu^{1/2}$$

where z is the number of electrons involved in the reaction, F is the Faraday's constant (96485 C/mol), C is the bulk concentration (mol/dm^3), A is the electrode surface area (dm^2), υ is the scan rate (V/s), D is the diffusion coefficient (dm^2/s), R is the universal gas constant (8.314 J/mol.K), T is the temperature (K) and I_{pa} is the anodic peak current (A).

- The peak potential and the redox couple potential E_p (against SHE) are related as follows:

$$E_p = (E_{pc} + E_{pa})/2$$

- The positions of peak potential are independent from the scan rate.

- When z electrons are involved in the reaction, the voltage separation between the two peak potentials can be estimated as follows:

$$E_{pc} - E_{pa} = 2.218RT/F$$

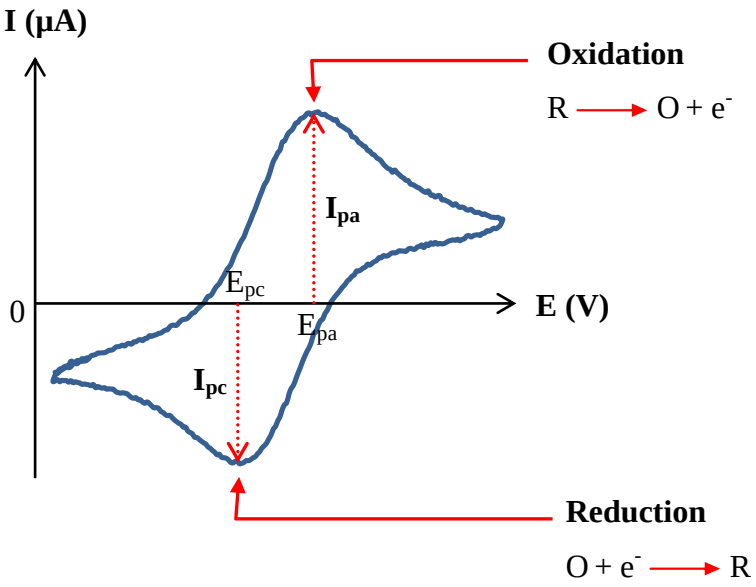

Fig. 7. Cyclic voltammogram of a reversible reaction using a macroelectrode. E_{pc} and E_{pa} are the peak potentials at the cathode and at the anode, respectively. I_{pc} and I_{pa} are the peak current at the cathode and at the anode, respectively.

The size of the diffusion layer at the electrode surface will be different depending on the voltage scan rate. In a slow voltage scan, the diffusion layer will grow much further from the electrode in comparison to a fast scan. Consequently, the flux to the electrode surface is considerably smaller at slow scan rates than it is at faster ones. As the current is proportional to the flux towards the electrode, the magnitude of the current will be lower at slow scan rates and higher at high rates. The influence of the voltage scan rate on the current for a reversible electron transfer is illustrated in Fig. 8.

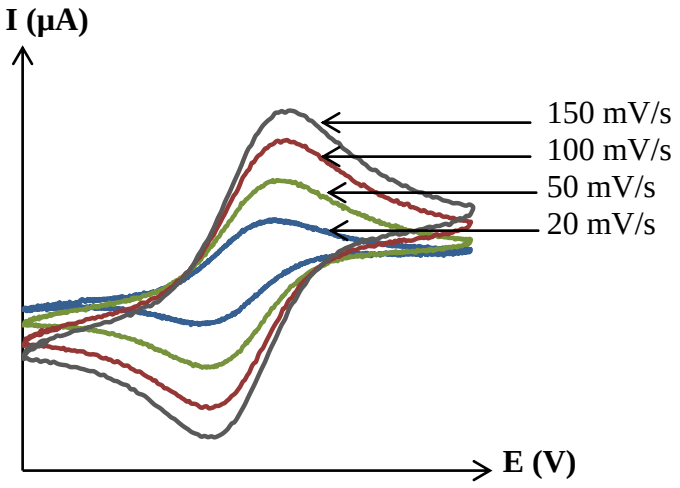

Fig. 8. Influence of the voltage scan rate on the current response.

Microelectrodes Array [9-11]

A microelectrode is one whose surface dimension is smaller than the scale of the diffusion layer. Other definitions describe microelectrodes as electrodes which have at least one dimension on the micron scale[10]. In the case of microdisc electrodes, the mass transport is dominated by radial diffusion, which differs from the planar diffusion of the macroelectrodes. For this reason, the cyclic voltammogram recorded for a reversible electrochemical reaction using microelectrodes does not have the same nernstian shape as seen previously, but a sigmoidal shape, with no peaks, where the constant current is called the steady-state current and is noted I_{ss} (Fig. 9).

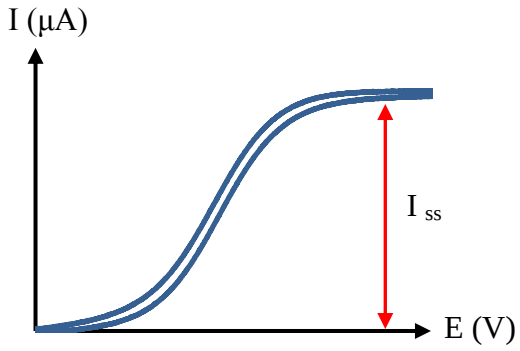

Fig. 9. Cyclic voltammogram at microelectrode.

I_{ss} does not depend on the scan rate υ. It can be determined by the following equation:

Eq. 6 $$I_{ss} = 4zFDCa$$

where a is the electrode radius (dm) and I_{ss} is the steady-state current (A).

Fabrication processes can imply the electrodes to be recessed or protruding. Depletion or relief brings variations of the diffusion layer shapes at the edge of the electrode. It is acknowledged that the current measured using a recessed electrode must be corrected to take this variation into account[12-15]. For recessed microdisc electrodes, the final steady state current follows Eq. 7:

Eq. 7 $$I_{lim} = I_{ss} \times \pi a/(\pi a + 4L)$$

where L is the depth of the recess (dm).

For shallow recessed microdisc electrodes (L/a <1), Eq. 7 can be improved further[16]:

Eq. 8 $$I_{lim} = I_{ss} e^{(-0.96L/a)}$$

Using microelectrodes not only permits a steady state current but it also allows a reduction in both the capacitive current and the ohmic drop. The capacitive current is proportional exponentially to the electrode area as showed in Eq. 9. It is strongly diminished when using microelectrodes and the current measured is mainly faradic current. The potential generated by the current running through the cell interferes with the supplied potential and diminishes it by iR (where i is the total current and R the cell resistance). The consequences on CV analyses are shifts of peak potential, decrease of the current magnitude and increase of the peak separation. The miniaturisation of the electrode reduces the currents measured, and therefore the ohmic drop.
Finally, the microelectrodes are more sensitive than macroelectrodes, as the signal-to-noise ratio is much higher.

Eq. 9 $$i_c = \frac{\Delta E}{R} e^{(\frac{-t}{RC})} \quad \text{with} \quad RC \propto a^2$$

where i_c is the capacitive current (A), R is the cell resistance (Ω), C is the capacitance of the microelectrode (F), ΔE is the potential difference (V), t is the time (s) and a the electrode radius.

The main inconvenience of using microelectrodes is the very low amplitude of the signals detected due to their dependence on the surface area. This makes the signal very sensitive to external perturbations. A solution to conserve the radial diffusion advantages of the microelectrodes while increasing their current magnitude is to use microelectrode arrays.

Microelectrodes arrays (MEAs) consist of microelectrodes built in series. Even though their development is still recent compare to the use of an individual microelectrode, MEAs have found applications in very diverse areas, such as the study of reaction mechanisms, as well as high-performance liquid chromatography detection, scanning electrochemical microscopy, or in vivo measurement on biological objects[1,2,17]. Many

studies have been reported describing the correlation between the current and the diffusion layer geometry and thickness at microelectrode surfaces of various shapes, the most common ones being the microband and the microdisc arrays[9,18-27]. In ideal conditions, the current response of a microdisc electrodes array has a sigmoid shape where the steady state current is the sum of the individual microelectrode responses (Eq. 10). As a result, the final current may have the same amplitude as a macroelectrode but it is still dominated by radial diffusion.

Eq. 10 $$I_{ss} = n4zFDCa$$

where *n* is the number of microelectrode supported by the array.

In the case of recessed microdiscs:

Eq. 11 $$I_{lim} = n4zFDCae^{(-0.96L/a)}$$

Those equations are applicable when the individual properties of the microelectrodes are preserved and there is no overlapping between their diffusion layers[28,29]. The merging of the diffusion layers would change the diffusion profile from radial to linear diffusion. CV responses of overlapping diffusion layers have a nernstian shape with peaks which tend to be scan rate dependent (comparable to macroelectrode behaviour). Therefore the electrodes must be separated enough so that their diffusion layers do not interact (Fig. 10). Even though different opinions exist concerning the exact distance required between the microdiscs[30], it is ~20 times the radius of the microdisc. This distance must remain small to not waste material and chemicals.

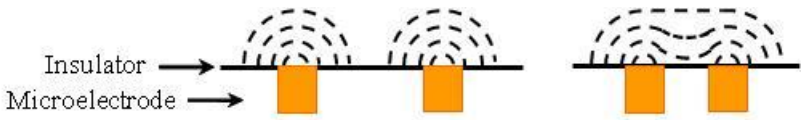

a. separated enough b. too close

Fig. 10. Diffusion at microdisc array.

The scan rate is also a parameter to take into account for CV measurement on MEAs. If the scan rate is too fast (Fig. 11.a), the diffusion layer thickness is small compare to the electrode size. The resulting mass transport is dominated by linear diffusion and the current response is the same as the macroelectrode response (Nernstian shape). If the scan rate is too slow (Fig. 11.c), the diffusion layer has time to grow and to become big enough to overlap with more distant electrodes, losing the radial diffusion profile. When the scan rate is slow or intermediate (Fig. 11.b), the diffusion layer is larger than the microelectrode, but yet does not interfere with another one. The response of the microdisc array is the response of one individual microelectrode multiplied by the total number of electrodes.

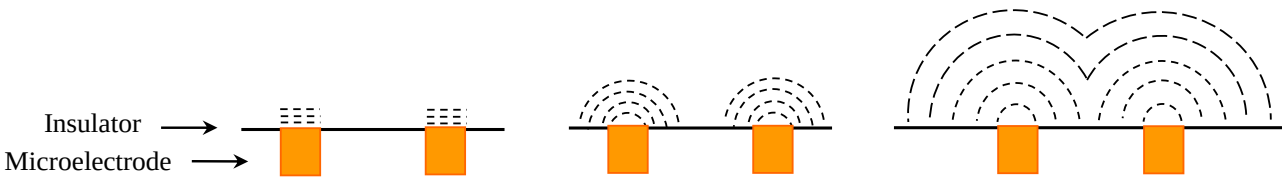

a. high scan rate b. medium c. very low scan rate

Fig. 11. Diffusion at microdisc array for various scan rates.

The optimum arrangement for an array is the hexagonal configuration, where the electrodes are at equal distance from each other and minimum space is wasted.

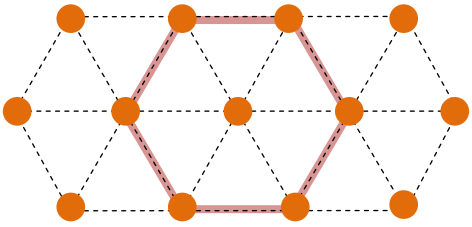

Fig. 12. Hexagonal arrangement.

CV Analysis: Electrolyte influence on potential window

In CV analysis, the supporting electrolyte is a non-reactive ion that behaves as an electrically conductive medium. It is present in high concentration in comparison with the reactive species in order to minimise the solution resistance and to prevent charged species migration caused by the electric field. The potential window of the analysis is defined as the potential range in which an electrode can be polarised in a solution without the passage of faradic current (Fig. 13).

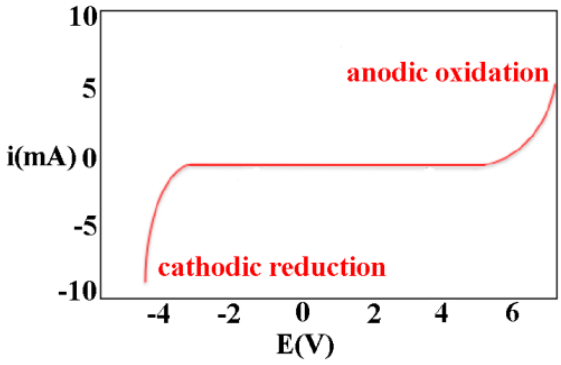

Fig. 13. CV voltammogram of an electrolyte.

This current is due to the oxidation or reduction of the supporting electrolyte or solvent. In practical work, the potential window depends on the nature of the solvent, the nature of the electrolyte, the nature of the electrode material and on the presence of contaminants[31]. Materials, solvents and electrolytes should be chosen in order to have a potential window large enough such that the analyte response is not obstructed by the limit of the potential window. Water gets oxidised and reduced at +1.23 V and -0.83 V, respectively. When non-aqueous solvents with a larger potential window such as acetonitrile are used, the limits depend on the supporting electrolyte. The more resistant the electrolyte's ions are to reduction and to oxidation, the wider the potential window is. Oxidation and reduction potentials for electrolyte in standard cyclic voltammetry analysis conditions can be found in the literature[32,33].

2.1.6. Chronoamperometry

Chronoamperometry belongs to the potential pulse techniques, and can be employed to measure the current which arises after the capacitive current. Contrary to cyclic voltammetry where the potential is applied linearly, in chronoamperometry the potential is applied in steps (Fig. 14), from a value where the analyte is not oxidised or reduced, E_1, to a value where it is (E_2). In this step technique, the current is diffusion-controlled and plotted as a function of time (Fig. 14).

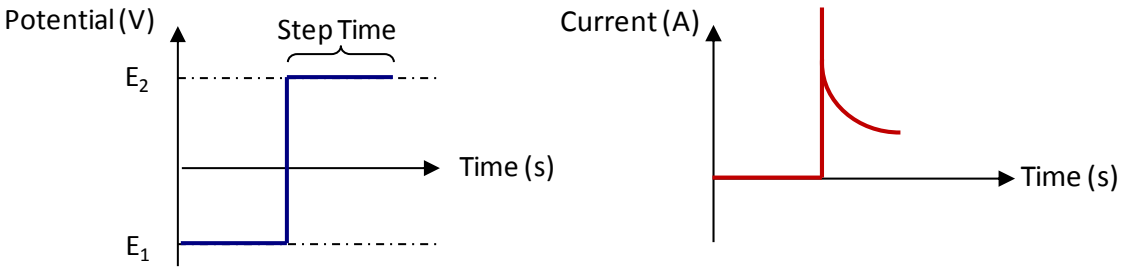

Potential applied to the cell versus time. Current response versus time.

Fig. 14. Chronoamperometry voltammogram.

The step time τ is the time for which the potential is maintained at the same value. It should be neither too short nor too long so that the current remains controlled by diffusion. If the step time is too short, the current measured includes the charging current. As the charging current decreases exponentially in time, it is negligible after a few milliseconds. At long times (of the order of 100 s), convection develops in the solution (from density gradients arising from the electrolysis products) causing positive deviations from the theoretical current.

When mass transport is only happening by diffusion, the current-time curve reflects the change in the concentration gradient at the electrode surface. This involves a gradual expansion of the diffusion layer associated with the diminution of the analyte, and hence decreased slope of the concentration profile as time progresses (Fig. 15). The environment is maintained still to observe no effects other than diffusion.

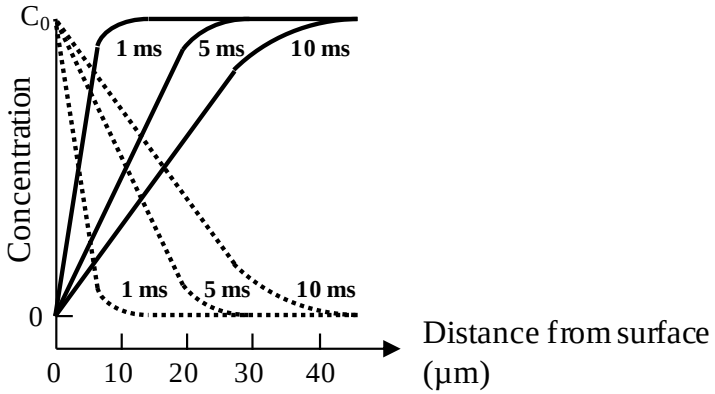

Fig. 15. Concentration gradient at the electrode surface for different step times.

The Cottrell equation (Eq. 12) describes the current decays with time, at a planar electrode. Typically, the current measured is then plotted versus $t^{-1/2}$ (Fig. 16) to get back to the concentration, the diffusion coefficient, the number of electrons transferred or the surface area.

Eq. 12 $$I(t) = zFACD^{1/2}/\sqrt{\pi t}$$

where z is the number of electrons involved in the reaction, F is the Faraday constant (C.mol^{-1}), A is the surface area (dm^2), C is the analyte concentration (mol/dm^3), D is the diffusion coefficient (dm^2/s) and t is the time (s).

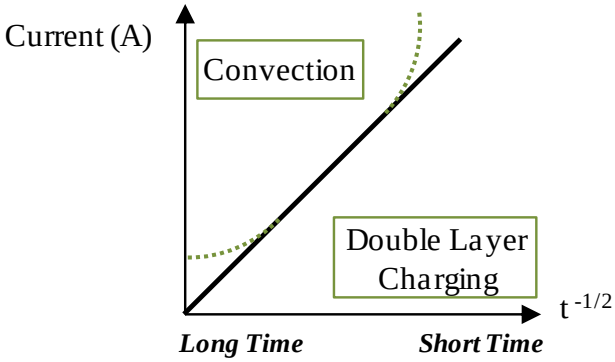

Fig. 16. Cottrell plot where the slope is $zFACD^{1/2}/\sqrt{\pi}$.

2.1.7. Electrochemical Impedance Spectroscopy

Electrochemical Impedance Spectroscopy (EIS)[1,34] was initially used for the determination of the double-layer, and became very popular in recent years as a complementary technique for the characterisation of electrode processes at complex interfaces. EIS consists on studying the response of an electrochemical cell to a small current perturbation around its equilibrium point. These measurements are carried out using sinusoidal voltage at different frequencies. To be analysed and correlated to physical properties, the impedance response measured is mimicked in an equivalent electronic circuit. EIS analysis provides information about the interface, its structure and the reactions taking place there.

The introduction to the notion of impedance is presented here for a standard electronic circuit composed of a resistor and a capacitor because they are the main elements used in the construction of an equivalent circuit for electrochemistry.

Electronic Introduction

In EIS the potential signal applied is sinusoidal:

Eq. 13 $$E(t) = E_0 \sin(\omega t)$$

where E_0 is the signal amplitude (V), ω is the angular frequency ($2\pi f$) (rad.s^{-1}), f is the frequency (Hz) and t is the time (s).

The phase relationship between voltage and current is usually described by a phasor diagram. In this, voltage (or current) is represented as a vector travelling anti-clockwise about the origin. Phasor diagram can describe magnitude and phase relationship between voltage and current.

The current passed by a resistor is directly proportional to the voltage given by Ohm's law. The relationship is independent of time and so the current and voltage are always in phase, as shown in Eq. 15 and in phasor diagram Fig. 17. On the other hand, a capacitor opposes changes in voltage by drawing or supplying current as it charges or discharges. The flow of electrons across the capacitor is directly proportional to the rate of these

changes, causing a phase shift between current and voltage, as shown in Eq. 17 and in phasor diagram Fig. 18. For a capacitor, current leads voltage by π/2.

Resistor:

Eq. 14 $$E_R(t) = I_R(t)R$$

where *R* is the resistance of the resistor (Ω).

Eq. 15 $$I_R(t) = \frac{E_R(t)}{R} = \frac{E_{0R}}{R} sin(\omega t)$$

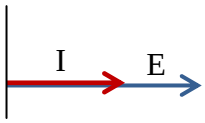

Fig. 17. Phase diagram for a resistor, where the potential and current are represented as vectors, respectively E (blue) and I (red).

Capacitor:

Eq. 16 $$E_C(t) = \frac{Q(t)}{C} = \frac{1}{C}\int_0^t I_C(t)dt$$

where *C* is the capacitance of the capacitor and Q is the amount of charge.

Eq. 17 $$I_C(\mathrm{t}) = C\frac{dE_C(t)}{dt} = CE_0\,\omega cos(\omega t) = \omega CE_0\, sin(\omega t + \pi/2)$$

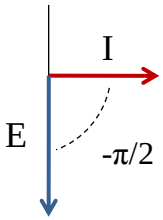

Fig. 18. Phase diagram for a capacitor, where the potential and current are represented as vectors, respectively E (blue) and I (red).

The relationship between the current and the voltage within the circuit depends on the connections between the elements. For a series RC circuit, the current is the same through each element and the total potential is the vector sum of the individual potentials. For a parallel RC circuit, the potential is the same across each branch and the total current is the vector sum of the branch currents.

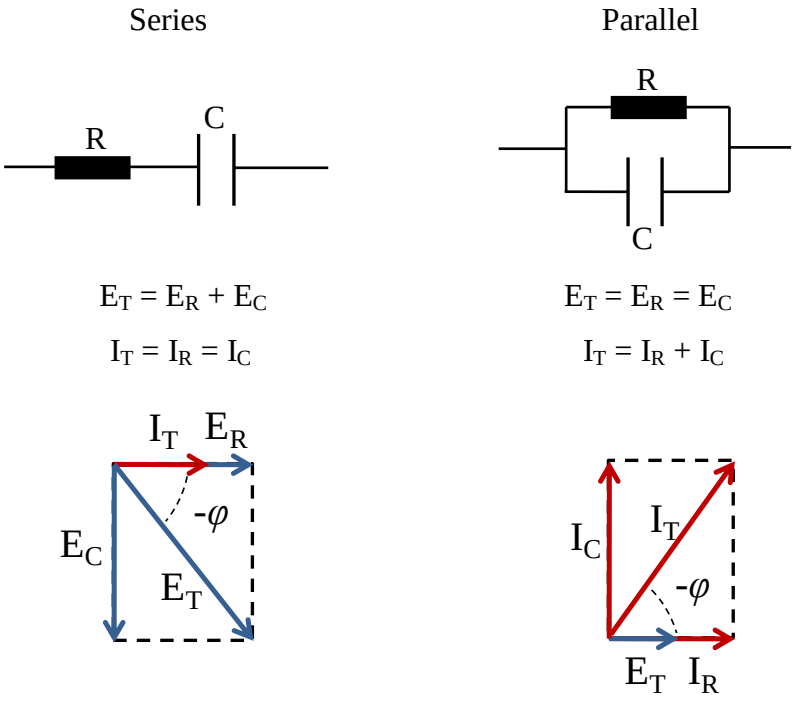

Fig. 19. Phase diagram for series (left) and parallel (right) RC circuit.

Fig. 19 illustrate that the response of a RC circuit to a potential perturbation is a current with the same frequency, f, but a different phase angle φ:

Eq. 18 $$i(t) = i_0 \sin(\omega t + \varphi)$$

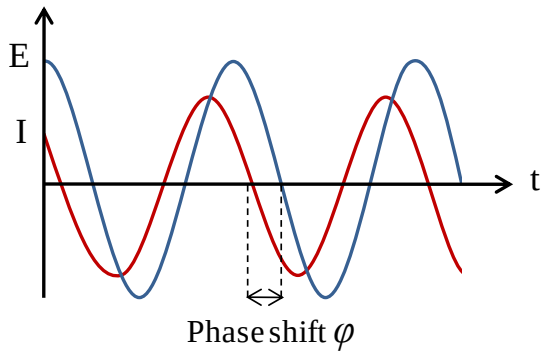

Fig. 20. Relationship between *E(t)* and *i(t)* with a phase shift φ.

Impedance Definition

As introduced earlier, the total potential in a series RC circuit is the vector sum of the individual potential of each element.

Eq. 19 $$E(t) = I(t)R + \frac{Q(t)}{C} = I(t)R + \frac{1}{C}\int_0^t I(t)dt$$

The combined effect of the resistor and capacitor to oppose the current flow can be expressed as a complex sum where the real part relates to the resistance and the imaginary part to the capacitor reactance. This sum, expressed in the units of resistance, Ω, is called impedance, Z, and characterises the ratio between total potential and total current in the circuit. The impedance complex includes both, magnitude, $|Z|$, and phase shift, φ, information.

Eq. 20 $$E = Z\, i$$

Eq. 21 $$Z(t) = \frac{E_0 \sin(\omega t)}{i_0 \sin(\omega t + \varphi)}$$

The impedance can be represented as a vector where Z' and Z'' are the real and imaginary part of the impedance and j is the imaginary number ($\sqrt{-1}$). The phase angle between real and complex impedance is $\varphi = \arctan(-1/\omega RC)$.

Eq. 22 $$Z(\omega) = Z' + jZ''$$

$$Z(\omega) = R - j\,\frac{1}{\omega C}$$

$$|Z| = \sqrt{R^2 + (1/\omega C)^2}$$

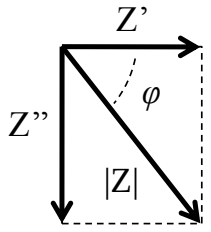

Fig. 21. Vector representation of the impedance.

In general cases, which involve more than a resistor and a capacitor, the impedance includes the resistance (*R)*, the capacitive reactance (*1/jωC)* and the inductive reactance (*jωL* with *L* being the inductance). The real part of the impedance is pure resistance and the imaginary element includes the capacitance and the inductance. Eq. 23, Eq. 24 and Eq. 25 illustrate the difference in impedance calculation for various type of circuit made of resistor and capacitors.

Eq. 23 $$Z(\omega) = R - j\frac{1}{\omega C}$$

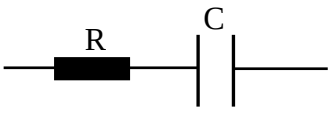

Eq. 24 $$Z(\omega) = \frac{1}{1/R + j\omega C}$$

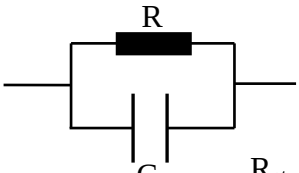

Eq. 25 $$Z(\omega) = R_s + \frac{1}{1/R_{ct} + j\omega C_{dl}}$$

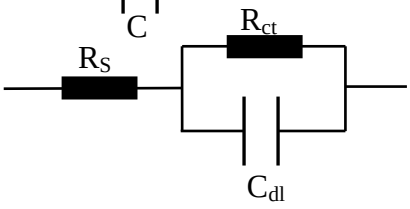

Impedance at solid electrodes

The model presented in Eq. 25 describes the ideal behaviour of the impedance for an ideally polarisable liquid electrode in the presence of a faradic reaction. In the case of solid electrodes, which are used in this project, the impedance behaviour often varies from this model and cannot be represented as a series connection of the solution resistance (R_S) and the double-layer capacitance (C_{dl}). Using a solid electrode implies the possible presence of frequency dispersion (due to ion adsorption and chemicals inhomogeneities) and microscopic roughness. The impedance for such a system is approximated by an infinite series of parallel R-C circuits where the double-layer capacitance is expressed as a Constant Phase Element, CPE (Eq. 26).

Eq. 26 $$Z_{CPE} = \frac{1}{Q(j\omega)^{\phi}}$$

where Q is a constant and ϕ is a number comprised between 0.5 for ideally porous electrodes and 1 for a perfectly smooth electrode. When ϕ= 1, the CPE is ideal and $Q = C_{dl}$.

The two most common plots to interpret the results and relate them to physical properties are the Nyquist plot and the Bode plot.

The Nyquist plot (Fig. 22) displays *-Z''* against *Z'*. It is the most frequently used in electrochemical literature as it allows an easier prediction of the equivalent electronic circuit. However, it does not represent the frequency dependence and therefore it is complemented by the Bode plot.

The Bode plots (Fig. 23, Fig. 24) display the impedance or phase angle against the frequency which allows the determination of the absolute value of the impedance $|Z|$ and the phase shift φ.

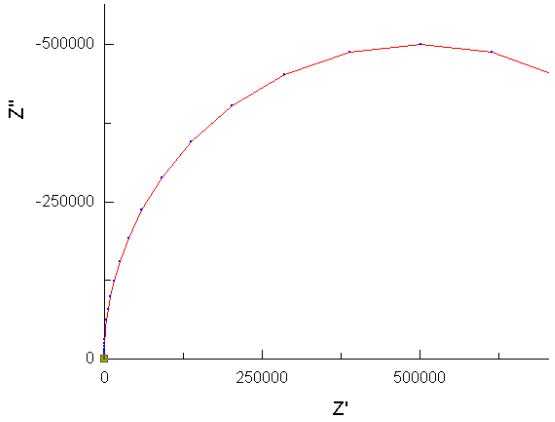

Fig. 22. Nyquist plot, imaginary part of the impedance, Z'', versus its real part, Z'.

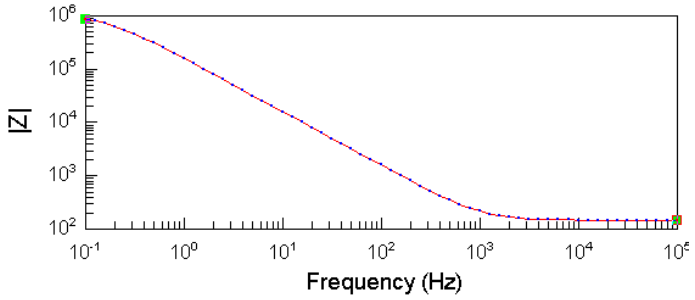

Fig. 23. Bode plot, absolute value of the impedance, $|Z|$, versus the frequency.

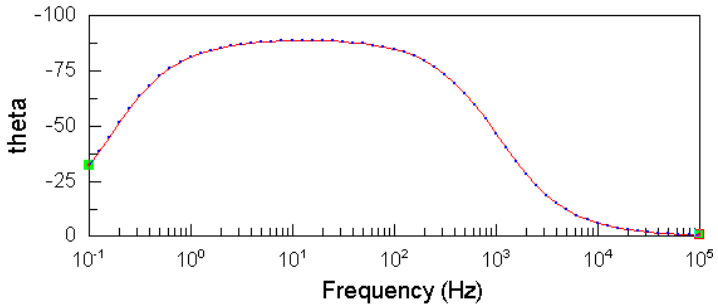

Fig. 24. Bode plot, phase angle, φ, versus the frequency.

2.2. CHIRALITY

Molecules which differ because of their chirality have the same structure, the same atom arrangement, and they usually result from the same synthesis. They react in the same way toward achiral molecules but they have specific behaviour toward other chiral molecules. Many biologically active molecules are chiral such as amino acids, sugars or enzymes. Therefore, the same molecule would be received differently by the biological system depending on its chirality. This biological differentiation motivates the need for chiral discrimination.

2.2.1. Isomerism

Isomers[35,36] are compounds with the same molecular formula but different structural or geometric organisation of their atoms. The diagram below presents the different types of isomers.

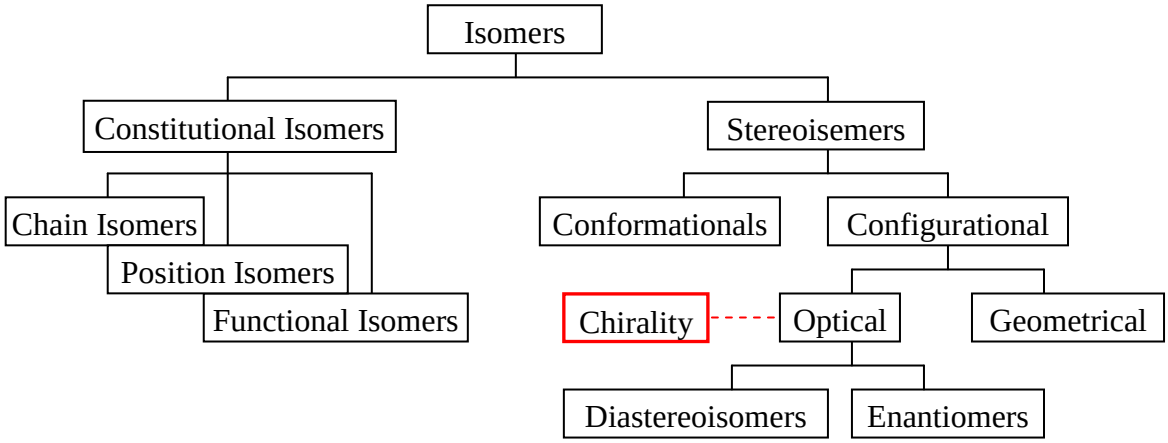

Isomers can be constitutional isomers (structural isomers) or stereoisomers (spatial isomers).

Constitutional Isomers

Constitutional isomers have their atoms and functional groups bonded together in different orders. There are three types of structural isomers; the chain, the position and the functional isomers.

Stereoisomers

Stereoisomers have the same atomic connectivity, but a different arrangement in space. They are either conformational or configurational isomers. Contrary to structural isomers, which typically have different chemical properties, stereoisomers behave identically in most chemical reactions, except when they react with other stereoisomers.

- Conformational isomers:

Conformers can interconvert by rotation around sp3 hybridised carbon sigma bonds, without breaking any chemical bonds. The rotations which allow the reduction of steric repulsions and make the conformer more stable happen preferentially.

- Configurational isomers:

Configurational isomers are not interconvertable. They differ by the way the atoms are arranged in space but this way is invariable. This category regroups the geometric isomers and the optical isomers.

- Geometrical isomers:

Also named “Cis-trans” or “Z-E” isomers, the geometric isomers have a different orientation of their functional groups. In general, such isomers contain double bonds which cannot rotate, or ring structures, wherein the rotation of bonds is greatly restricted. They often have some differences in their physical and chemical properties due to the fact that differences in the shape of the molecule change the overall dipole moment, which may result in a change of boiling point.

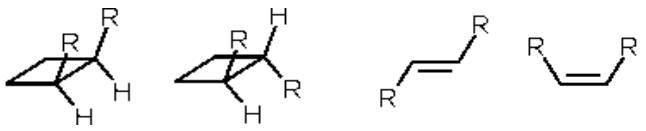

“Cis” “Trans” “E” “Z”

Fig. 25. Cis/Trans, Z/E isomers.

- Optical isomers:

The optical isomers are the diastereoisomers and the enantiomers. They contain at least one asymmetric centre in their structure, i.e. one tetravalent atom (or equivalent) with four different substituents.

Diastereoisomers are stereoisomers that are not mirror images of each other and are non-superimposable as illustrated in Fig. 26. They have different physical properties.

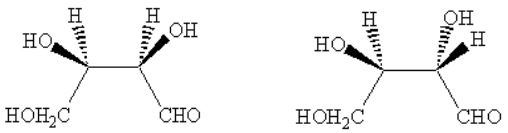

Fig. 26. Diastereosimers.

Enantiomers are mirror-images of each other and are non-superimposable as illustrated in Fig. 27. They have identical chemical and physical properties except for their ability to rotate plane-polarised light by equal amounts but in opposite directions. A mixture of equal parts of an optically active isomer and its enantiomer is named racemic and has a net rotation of plane-polarized light of zero. Symmetrical enantiomers often have different reactivity with other enantiomers. Since many molecules in living bodies are enantiomers themselves, there is often a difference in the way enantiomers react in vivo.

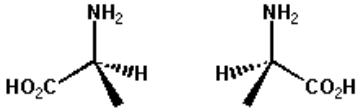

Fig. 27. Alanine enantiomers.

2.2.2. Chirality

Definition

A chiral centre can be defined as an sp3 hybridized atom which is bonded to four different groups in such a manner that it has a non-superimposable mirror image. The most prevalent chirality centres in organic chemistry are carbon atoms (Fig. 28, where the chiral carbon is marked with a red star) but they can also be Si, N and P where a lone pair is included as one of the four different groups.

Molecules are chiral if they contain one or more chiral centres and have a non-superimposable mirror image (also referred as enantiomers): if not they are achiral molecules.

Meso compounds have chiral centres but are still achiral compounds since they are superimposable to their mirror image because of the presence of a plane of symmetry. An example is given in Fig. 29.

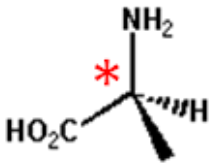

Fig. 28. Chiral centre of the alanin.

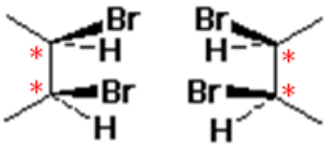

Fig. 29. Meso compound, 2,3-dibromobutane.

The number of possible configurations for a molecule having n chiral centres is equal to 2^n. This rule works as long as the compound doesn't have meso form.

Nomenclature

Chiral centres can be named depending on their configuration (convention R/S or D/L) or depending on their optical activity (convention (+) and (-)). There is no correspondence between those conventions.

- R/S nomenclature:

Chiral centres are characterised by the relative position of their surrounding atoms. Groups linked to the chiral centre are ranked depending on their atomic number (Cahn-Ingold-Prelog priority rules), where the higher atomic numbers are given higher priority.

Chiral centres are labelled R (Rectus) or S (Sinister). When the centre is oriented so that the atom having the lowest-priority is pointed away from a viewer, there are two possibilities:

- If the priority of the remaining three substituents decreases in a clockwise direction, the chiral centre is labelled R (Fig. 30.a).
- If the priority decreases in a counterclockwise direction, the chiral centre is labelled S (Fig. 30.b).

a. R-glyceraldehyde **b.** S-glyceraldehyde

Fig. 30. Different chirality of the glyceraldehyde.

The R/S system has no fixed relation to the (+)/(−) or to the D/L system.

- D/L nomenclature:

The D/L system relates the molecules to the glyceraldehyde configuration. Glyceraldehyde is chiral, and its two isomers are labelled D (Dextrorotatory) and L (Levorotatory) as shown in Fig. 31. The D/L labelling is unrelated to (+)/(−). Rather, it says that the compound's stereochemistry is related to that of the dextrorotatory or levorotatory enantiomer of glyceraldehyde. D- or L- naming scheme is called relative configuration as opposed to the absolute configuration (+)/(-) and (R)/(S).

D-gluceraldehyde L-glyceraldehyde

Fig. 31. D and L glyceraldehyde enantiomers.

Molecules are assigned the D- or L- configuration if the chiral centre can be obtained from glyceraldehyde substitution. For the groups COOH, R, NH_2 and H (where R is a variant carbon chain) arranged around the chiral centre, and the molecule placed with the hydrogen atom away from the viewer, the molecule is named D when the groups are

arranged clockwise around the carbon atom and L when they are arranged counter-clockwise.

- (+)/(−) nomenclature:

This system names the molecules after their optical activity depending on the direction in which they rotate the plane of polarised light. If they rotate the light clockwise (as seen by a viewer towards whom the light is travelling), that enantiomer is (+). Its mirror-image is labelled (−). The (+) and (−) isomers can also been termed d- and l-, respectively for dextrorotatory and levorotatory.

2.3. INDUSTRIAL CHIRAL ANALYSIS

The most frequently used analytical techniques to probe chirality in industry are chromatographic processes such as[37] :

High-performance liquid chromatography (HPLC)
Gas chromatography (GC)
Supercritical fluid chromatography (SFC)
Capillary electrophoresis (CE)

Chromatographic processes imply that the enantiomers are separated before their detection. In HPLC, GC and SFC analyses the chiral separator consists of a column, which intern wall are covered with a chiral stationary phase. The enantiomers migration time differs based on the amount of interaction between the individual analytes and the stationary phase. The mobile phase carrying the enantiomers is a liquid in HPLC, a gas in GC and a supercritical fluid in SFC.

The most common chiral detectors are polarimeters and circular dichroism[38]. Polarimeters measure the angle of rotation of the light when it passes through optically active substance such as enantiomers. Circular dichroism characterises an optically active compound based on its absorption of right and left hand circular polarised light.

The main non-chromatographic analyses include NMR (nuclear magnetic resonance) and enzyme techniques, used in specific biomedical applications.

2.4. PHENYLETHANOL ELECTRO-OXIDATION

An alternative to post reaction purification is to orientate the chemical synthesis in order to synthesise only one enantiomer. This can be done by using a chiral reagent or incorporating a chiral molecule to the reagent in order to force the reaction in one direction and produce just one of the enantiomers. Chiral agents are in high demand from the pharmaceutical industry for the bulk synthesis of drugs and they require regular control of the reagent's and product's chirality. As a result, the synthesis of enantiopure intermediates and the associated chiral recognition remain of high interest. 1-phenylethanol (PE) is a common precursor for chiral building blocks in drug syntheses.

Being able to discriminate the two PE enantiomers using electroanalysis as an alternative technique to standard instrumental techniques such as column chromatography methods is part of this project. Electroanalysis allows a potential reduction in analysis fees and an answer in real time. The loss of chemicals imposed by sampling and destructive techniques is minimised or fully avoided in the case of a reversible reaction.

2.4.1. Phenylethanol Electro-Oxidation

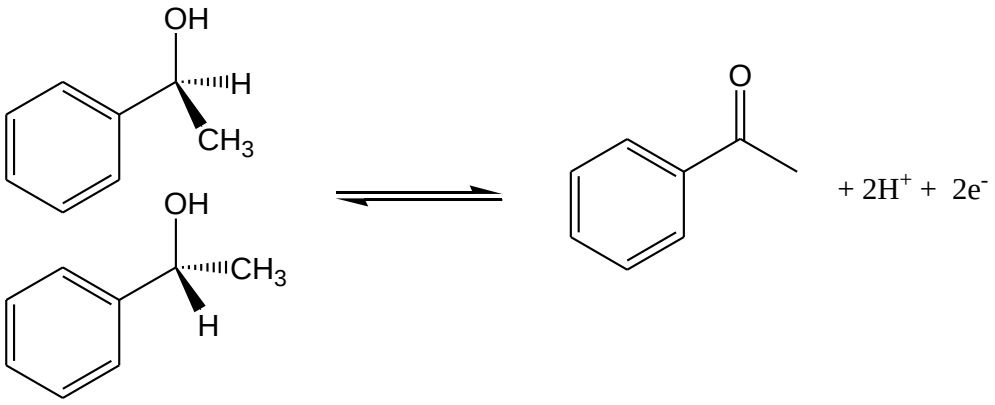

Fig. 32. PE oxidation.

The PE can be oxidised in acetophenone (Fig. 32) in the presence of a nitroxyl radical, which is a common oxidising agent for alcohol electro-oxidation[39-43], and a base, which facilitates the proton transfer. Even though the details of this reaction have been studied [44-48], certain aspects of the reaction mechanism remain dark and can still be the source of many investigations. The highlights of the oxidation are shown schematically in Fig. 33, where the nitroxyl radical is 2,2,6,6-TEtraMethyl-Piperidin-1-Oxyl (TEMPO) and the base is lutidine.

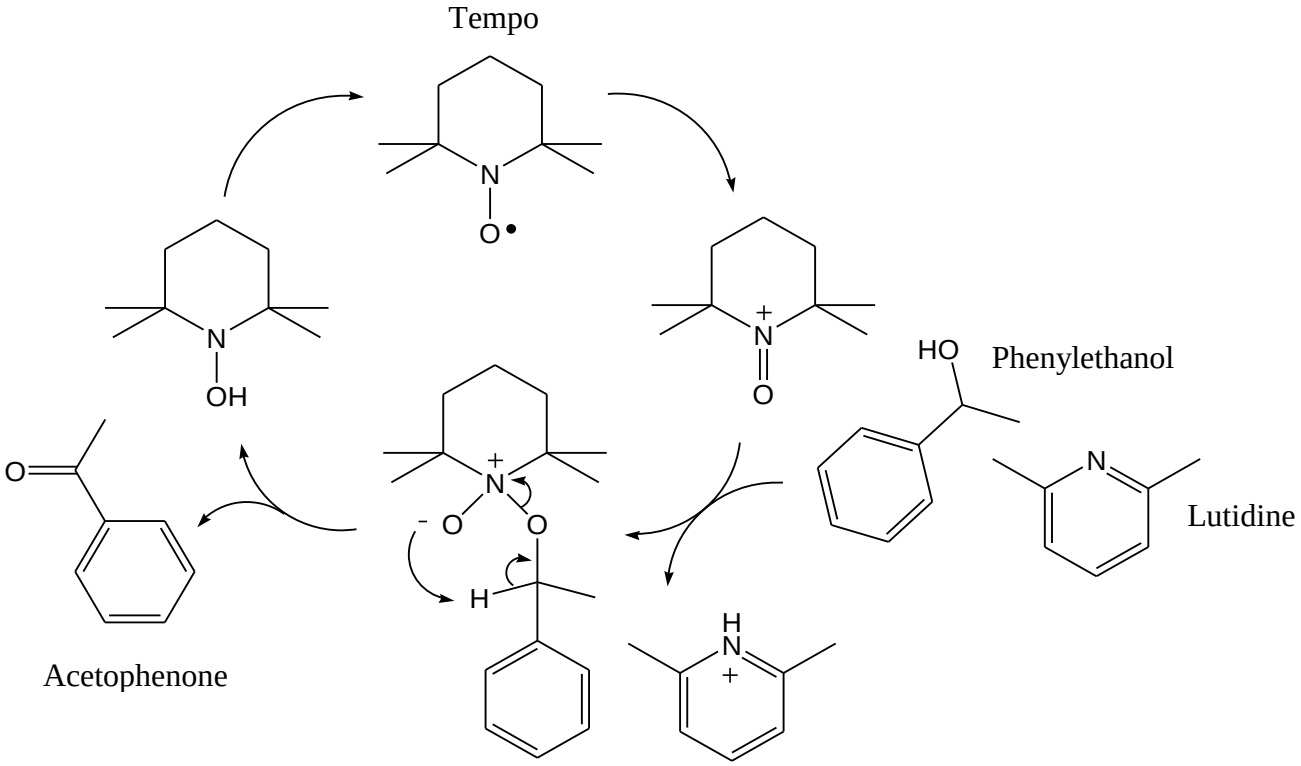

Fig. 33. Mechanism of the PE oxidation reaction.

The TEMPO radical (Fig. 34.a) is a weak oxidant. It must be oxidised in the presence of a primary oxidant such as sodium perchlorate in its cationic form (Fig. 34.b) to increase its oxidising power and to catalyse the alcohol oxidation. After complexion with the PE, the hydroxylamine is released (Fig. 34.c) and regenerated in the TEMPO radical[49].

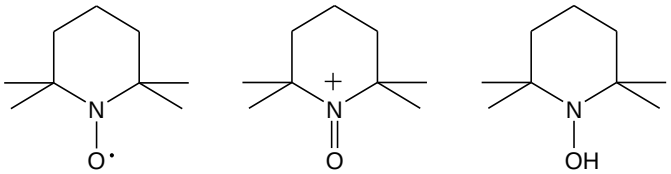

a. TEMPO Radica **b.** TEMPO cation **c.** Hydroxylamine

Fig. 34. TEMPO derivatives.

The work of both Deronzier et al.[50] and Osa et al.[51] compared the stability of the nitroxyl catalyst in bulk solution and immobilisation at the surface of the electrode via electropolymerised films on metal and polymers on graphite felt electrode. Conclusions showed that the nitroxyl catalyst tends to be more stable when it is immobilised at the electrode surface. Following this path, most of the alcohol electro-oxidation processes are conducted with the nitroxyl radical being immobilised at the electrode surface[52-54].

2.4.2. Enantioselective Oxidation

The PE oxidation as described above is not enantioselective. TEMPO is achiral and reacts without preferences with (R)-PE and (S)-PE. The reaction can be orientated to oxidise preferably one enantiomer by introducing chirality to the process. The enantioselectivity of the response is achieved by kinetic resolution due to the formation of molecular complexes of the chiral selector with preferentially one of the analyte's enantiomers. Diverse methods have been explored for electrochemical chiral sensing with variable efficiency[39,55] such as, membrane technologies (potentiometric sensors), biosensor using enzyme substrates, highly organised materials where the chirality is intrinsic to the electrode[56-59] and techniques involving chemical modification of a metal electrode surface. The latest one includes physical sorption and covalent binding in thin surface films[60,61], self-assembled layers or electropolymerised materials[62,63].

In the case of the enantioselective oxidation of PE, the two enantiomers can be selectively oxidised using chiral TEMPO derivatives[63-70] immobilised at the surface of the electrode, chemically adsorbed on metal by electropolymerisation (Fig. 35) or covalently attached to graphite through poly(acrylic acid) (PAA) (Fig. 36).

The electropolymerisation at metal electrodes engages a derivative of pyrrole monomer containing nitroxyl radical group[63]. This procedure is successful but requires heavy organic synthesis steps to produce monomers that are not available on the market.

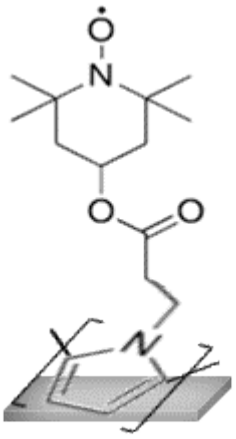

Fig. 35. Example of metal electrode modified with TEMPO derivative.

In the case of glassy carbon (GC) electrode modification, the PAA binds to the surface via a carbon-carbon bond. The TEMPO derivative is immobilised on PAA via an amido bridge[45,52] (Fig. 36).

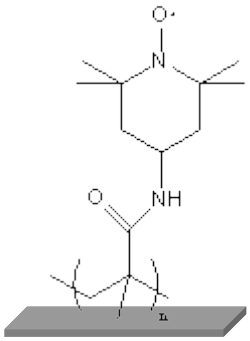

Fig. 36. Example of GC electrode modified with TEMPO derivative.

Bringing chirality to the base instead of the nitroxyl radical was also investigated and the PE electro-oxidation could be orientated with variable success by using a chiral base such as (-)-sparteine[64,70,71] in bulk solution.

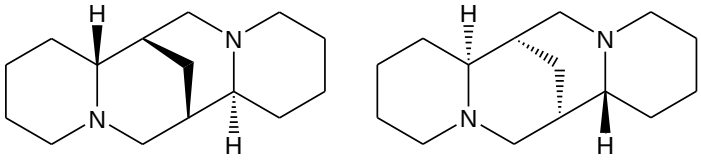

(-)-sparteine (+)-sparteine

Fig. 37. Sparteine enantiomers.

The efficiency of the amperometric chiral sensor can be quantified by the calculation of the selectivity coefficient, K_{ij}[55], defined in Eq. 27. When its value is larger than 10^{-3}, the coefficient is considered representative of the interfering effect between the chiral agent and the enantiomer. When K_{ij} value is less than 10^{-3}, the effect is not manifest.

Eq. 27 $$K_{ij} = (\Delta i_j / C_j)/(\Delta i_i / C_i)$$

where $\Delta i_j = i_j - i_b,\ \Delta i_i = i_i - i_b$, i_i and i_j are the currents of the different enantiomers, i_b is the residual (background) current at the electrode, and C_i and C_j are the concentrations of the corresponding enantiomers.

2.5. SELF-ASSEMBLED MONOLAYER

Self-Assembled Monolayer's (SAM) are of interest as a way to functionalise the electrode surfaces to give them specific properties and extend their field of application.

2.5.1. SAM Definition

A self-assembled monolayer can be defined as a layer of molecules that spontaneously organise themselves side by side into a specific and reproducible arrangement at the interface between two phases. The process is driven by the minimisation of the interaction energy between the molecules.

The first molecular monolayer films studies were conducted by Irving Langmuir and Katherine Blodgett in the 30's[72,73]. The so called Langmuir-Blodgett films consisted of a layer(s) of amphiphilic molecules transferred from liquid to solid surfaces. Irving Langmuir was awarded the Nobel Prize in 1932 for his discoveries and investigations in surface chemistry [74]. The first Self-Assembled Monolayers of surfactant molecules on metal surfaces were reported by Zisman et al.[75] in 1946.

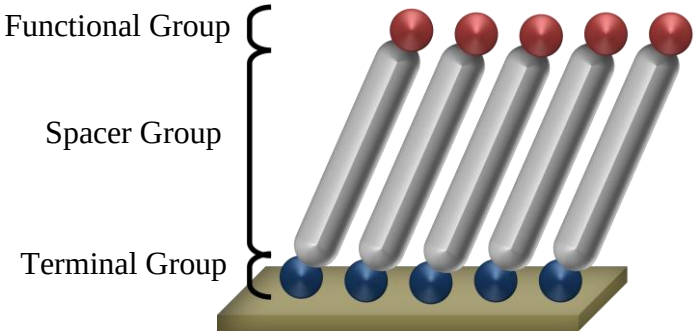

Fig. 38. Self-assembled Monolayer.

SAM at a solid-liquid interface can be represented as shown in Fig. 38, where the molecules are defined by 3 different entities: the terminal group, the spacer group and the functional group. The terminal, or anchoring, group is covalently bonded to the substrate

by spontaneous exothermic chemisorptions. The SAM organisation is driven by the forces of interactions between the molecules such as van der Waals forces or dipole interactions. Therefore the nature of the spacer group essentially defines the arrangement of the final layer. The properties of the functional group define the surface properties as the group interacts directly with the chemicals in the liquid phase.

SAMs can be formed on various substrate such as glass (silane anchoring group)[76], oxidised silicon, liquid mercury, gold, silver, copper or iron. Thiol SAMs on gold were reported by Nuzzo and Allara[77] in 1983. Since then thiol SAMs have been studied extensively[78-83] and are now probably the most common SAM used. In this case, the terminal group binding with gold is sulphur. The free energy of alkanethiol SAMs is minimum when the van der Waals interactions between the carbon chains are maximum. The alkyl tails tilt in such a way as to maximise the van der Waals interaction. The lowest free energy of alkanethiol SAM is obtained for layers where the molecule backbones are tilted by ~30 degrees from normal with a rotation of ~55 degrees[84]. The distance between sulphur atoms is 5 Å and the molecules are organised in an hexagonal lattice as showed in Fig. 39.

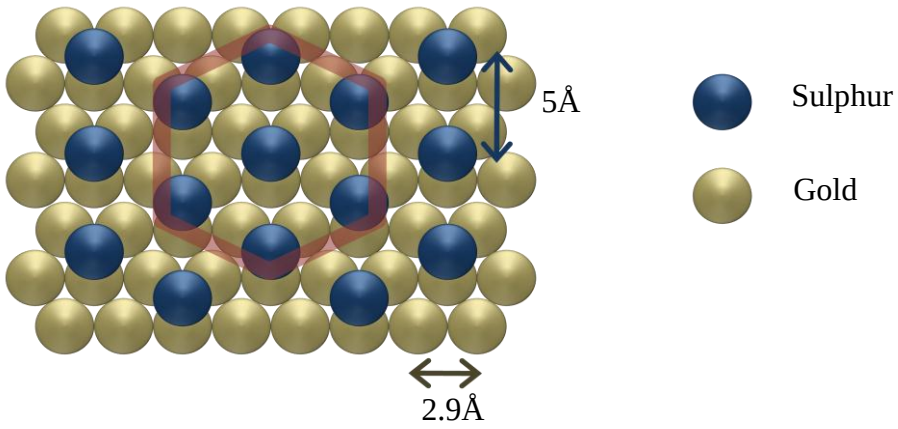

Fig. 39. Lattice model showing the surface projection of an alkanethiol on Au(111). The hexagonal structure is highlighted in red.

The preparation of thiol SAMs consists of a simple immersion of an extremely clean gold substrate in a diluted solution of alkanethiol. The monolayer spontaneously forms at the surface of the gold within the next 1 to 24 hours.

The formation of the self-assembled monolayer from thiol in solution involves the breaking of a S-H bond which is driven by the simultaneous formation of a strong Au-S bond energy of ~45kcal/mol [80] (Eq. 28).

Eq. 28 $$RS\text{-}H + Au \longrightarrow RS\text{-}Au + \tfrac{1}{2} H_2$$

The S-Au bond created is strong and the resulting monolayer very stable in both organic and aqueous solvent. Moreover the resistance of the bond to a large range of potential makes it very well adapted to electrochemistry applications.

In electroanalysis using a SAM modified electrode, the electron transfer between the solution species and the electrode surface through the SAM can occur in three ways[85]:

- The electron can transfer through the film via a tunneling process
- The electroactive species can permeate through the monolayer and react at the electrode surface
- The electroactive species can diffuse to a bare spot, e.g. a pinhole, on the electrode.

The nature of the molecule and the SAM structure determine how much of each process is happening.

Defect and pinholes are frequent for short alkyl chain SAM[85] which imposes the need for characterisation of the monolayer. Electroanalysis such as CV and EIS analyses allow the definition of kinetics parameters, surface coverage and structure of the SAM. When the shapes and the sizes of the pinholes vary in the micrometre range, they can be characterised and used as a proper random microelectrode array[79,86]. For a pinhole free SAM, the current is attributed to the electron tunneling across the monolayer and decreases as the thickness increases, as describes by Marcus theory[87]. For a compact SAM made of a long hydrocarbon chain (n>9) any electrochemical processes can be suppressed[85]. The variation of the tunneling effect due to the presence of unsaturation or aromatics character in the molecule can be calculated via impedance spectroscopy[88].

2.5.2. SAM Application

SAMs can be applied to electrodes to create selectivity at their surface and interactions can be designed with a targeted molecule by choosing the appropriated head groups and monolayer organisation. This applies to a macroelectrode but also to a microelectrode array[89] for biomedical applications, such as in vitro cell culture[90], biosensors[91], molecular electronics[92], where reducing the sampling quantities is always of interest. The process of deposition is the same as the one described above and can be optimised in the case of closely spaced microelectrodes (6 µm)[93].

SAMs of peptides and active moieties on gold surfaces is of great interest as it allows the study of the effect of fundamental surface properties on biological interactions[94,95].
For example, the cysteine and its derivatives compose an important group that can be used in SAM[82,96,97] for biomolecule sensing[98]. The glutathione (tripeptide y-glu-cys-gly, GSH) (Fig. 40), is the major low-molecule-mass thiol compound in plants and animals[99,100]. It is a natural reducing molecule with many physiological functions, such as redox buffering, detoxification, and antioxidant activity. Those properties, along with its low price, make it very attractive for surfaces and electrodes modification[94,101-104]. The different parameters involved in the GSH chemisorptions and their effects on the resulting SAM have been studied extensively[95,105-108].

Burgi et al. worked on the chiral differentiation at SAM surfaces[109,110] and developed Attenuated Total Reflection Infrared (ATR-IR) and Modulation Excitation Spectroscopy to show the potential of a L-Glutathione (Fig. 40) SAM on gold macroelectrode to react enantioselectively with proline[111]. Cysteine (Fig. 41) SAM also showed the ability to distinguish enantiomers such as proline[112] or 3,4-dihydroxyphenylalanine (DOPA)[113] .

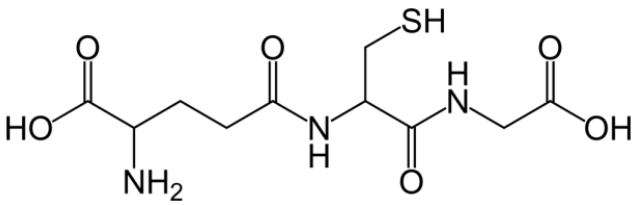

Fig. 40. Glutathione.

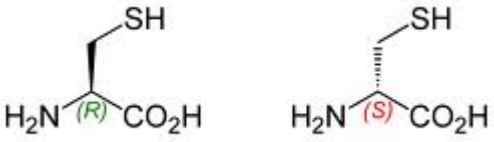

Fig. 41. Cysteine.

Another growing application of SAM in biological analysis is the immobilising of DNA at the electrode surface in gene mapping technology[114]. The structure of the DNA monolayer can be analysed electrochemically once immobilised at an electrode[115,116]. A monolayer of thiol modified single-stranded oligonucleotides on gold electrode can be formed following a similar protocol as for an alkanethiol layer. The need of miniaturisation is also constant for bio-sensing where sample quantities are limited.

3. EXPERIMENTAL WORK

3.1. ELECTROANALYSIS:

CYCLIC VOLTAMMETRY AND IMPEDANCE

The experimental set up was composed of three electrodes; the reference electrode, the counter electrode and the working electrode. The working electrodes used were platinum, gold and glassy carbon macroelectrode from BASi (Fig. 42), and a gold microelectrode array (fabricated in the School of Engineering and Computing Sciences). The reference electrodes were pseudo references. They consisted of platinum wire[117] (Aldrich) and gold flag. The counter electrodes were platinum and gold flags.

Fig. 42. Macroelectrode.

When using macroelectrodes, the analyses were performed in a glass reactor placed in a faradic cage to minimise the interference from external source. The solution was unstirred to favour diffusion as main contributor of mass transport, and the reactor was maintained under nitrogen (Fig. 43).

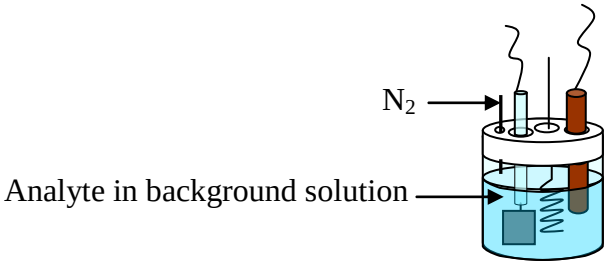

Fig. 43. Electroanalysis supported by macroelectrode.

Substrate Preparation

Prior to analysis, the surfaces of the different electrodes were cleaned of particles and organic material. The platinum flag was cleaned in piranha solution, made of sulphuric acid (Aldrich) and hydrogen peroxide (Aldrich), (3:2 H_2SO_4:H_2O_2 v/v), for 20 minutes. The electrode was then rinsed in water and acetone, and dried under N_2. The glassy carbon macroelectrode was polished using 0.3 µm silica particles (Buehler). The electrode was then rinsed in water and acetone and dried under N_2. The gold and platinum macroelectrodes were polished on microcloth (BASi) using diamond polish slurry (BASi) of different sizes (successively 15 µm, 6 µm, 3 µm and 1 µm). The electrodes were rinsed in water and acetone and dried under N_2.

The cleanliness of the gold and platinum electrodes was confirmed by running CV analysis in a 1 mol/L sulphuric acid solution between 0 and 1.5 V (vs Ag/AgCl/KCl 3.5 mol/L reference electrode). The measurement was repeated until a stripping charge higher than 1.4 $\mu C.cm^{-2}$ was obtained. The electrodes were rinsed in water and acetone and dried under N_2.

Background electrolyte comparison

The potential windows of the electrolytes $NaClO_4$ (Aldrich) and $NaPF_6$ (Fluka) were compared using a gold working electrode, a platinum wire as a pseudo reference electrode, and a platinum flag as a counter electrode. The salts were dissolved in acetonitrile (HPLC gradient grade) with a concentration of 0.1 mol/L. The cyclic voltammetry measurements were carried out between 0 and 3 V.

Catalysed electro-oxidation of 1-phenylethanol

The following analytes and mixtures were dissolved in acetonitrile solution containing $NaClO_4$ (0.1 mol/L) as background electrolyte. The auxiliary electrode was a platinum flag, the working electrode was a glassy carbon, gold or platinum electrode and the pseudo reference electrode was a platinum wire.

The components involved in the 1-phenylethanol (PE) oxidation were analysed individually.
CV characterisation was performed, at varying scan rates, on solutions containing 0.15 mmol/L of 2,2,6,6-tetramethyl-piperidin-1-oxyl (TEMPO, Aldrich), on solutions containing 0.02 mmol/L of sparteine (Aldrich), on solutions containing 0.02 mmol/L of lutidine (Aldrich), on solutions containing 0.01 mmol/L (+)-PE (Fluka), and on solutions containing 0.01 mmol/L (-)-PE (Fluka).
CV analyses for mixtures of the different components with the same concentrations were also performed.
Finally, the catalysed electro-oxidation of PE was analysed in solutions containing TEMPO (0.15 mmol/L), (-)-sparteine (0.02 mol/L) and (-)-PE or (+)-PE (0.01 mol/L), and in solution containing TEMPO (0.15 mmol/L), 2,6–lutidine (0.02 mol/L) and (-)-PE or (+)-PE (0.01 mol/L).

Flow Injection Analyses (FIA) by chronoamperometry

In the case of FIA measurements, the analyte was injected into the microfluidic channel using a syringe micro pump (KDS100 , Kd Scientific). To create a gradient of concentration, a closed reservoir containing solvent and background electrolyte was

inserted between the syringe and the device via tubing. As the analyte was pumped in the circuit, its concentration in the reservoir increased, until reaching its source value, when the reservoir content has been fully replaced with the syringe solution. The analyte probed was TEMPO, dissolved in acetonitrile containing 0.1 mol/L of $NaClO_4$ as a background electrolyte. The flow rate was 3×10^{-8} m^3/s.

Instrumentation

Cyclic voltammetry and chronoamperometry were performed using a multichannel VMP potentiostat from Perkin Elmer Instruments. The software used to record the data was EClab V9.42.
Impedance spectroscopy analyses were supported by a PAR model 283 potentiostat coupled with a Solartron model 1260 frequency response analyser.

3.2. ELECTRODE SURFACE MODIFICATION

3.2.1. Electropolymerisation with TEMPO Entrapping

The electropolymerisations and characterisations were performed in a one-compartment cell using a gold bare electrode (Ø=1.6 mm) as the working electrode, a platinum flag as the counter electrode and a platinum wire as pseudo reference.

The ProDOT (Aldrich) polymerisations were performed in acetonitrile solution containing $LiClO_4$ (Aldrich) (0.1 mol/L), TEMPO (1 mmol/L), and the monomer (0.01 mol/L). 20 cycles were run between -1 V and 1.3 V at 50 mV/s, leading to the formation of a black electroactive film at the surface of the working electrode.

Pyrrole (Aldrich) polymerisations were performed in acetonitrile solution containing $NaClO_4$ (0.1 mol/L), TEMPO (1 mmol/L) and the monomer (0.1 mol/L). 10 cycles were run between -0.2 V and 0.8 V at 50 mV/s, leading to the formation of a black electroactive film at the surface of the working electrode.

The films were characterised by CV analyses, conducted in acetonitrile solutions containing 0.1 mol/L of $NaClO_4$.

3.2.2. Amino-TEMPO Modification at GC Electrode

The glassy carbon (GC) electrode surface was modified with Poly Acrylic Acid (PAA, Wako) and then treated with 1-ethyl-3-(3dimethylamino-propyl)-carbodiimide hydrochloride (WSC) and 4-amino-TEMPO (Aldrich), following the protocol described by Kishioka et al[45]. 4 µl of a 6.25×10^{-6} % aqueous PAA solution was cast-coated on the GC surface by using a micropipette. The surface was dried for 4 hours in a desiccator. 2 µl of 4-amino-TEMPO (3.47 mmol/L, i.e.20 times equivalents with respect to the amount of carboxyl groups in the PAA film) dissolved in water containing 3.47 mmol/L WSC, was cast on the electrode surface. The electrode was then left in a desiccator overnight.

Electrochemical characterisation of the polymer was performed in a one-compartment cell using the modified GC electrode as a working electrode, a platinum flag as the counter electrode and a platinum wire as pseudo reference. CVs were conducted in acetonitrile solutions with 0.1 mol/L of $NaClO_4$.

3.2.3. Self-Assembled Monolayer

In this project the electrode surfaces were modified with a monolayer of dodecanethiol, glutathione, cysteine and DNA.

Dodecanethiol self-assembled monolayer preparation

The gold electrodes to be modified were firstly cleaned by cyclic voltammetry in 1 mol/L sulphuric acid, rinsed with ethanol and dried with nitrogen, after which they were placed directly in a solution of 1 mmol/L dodecanethiol (Aldrich) in ethanol. The self-assembled monolayer was formed by maintaining the electrodes immersed in the solution for 24 hours, at room temperature and in an air tight container to prevent any solvent evaporation. The surfaces of the electrodes were then rinsed in solvent and water to remove unattached thiol residue.

Electrochemical characterisation of the SAM was performed in a one-compartment cell using the modified gold electrode as a working electrode, a platinum flag as a counter electrode and a platinum wire as pseudo reference. CVs and impedance were conducted on 1 mmol/L $K_3[Fe(CN)_6]$ (Aldrich), dissolved in deionised water containing 0.1 mol/L of KNO_3.

GSH and cysteine self-assembled monolayer preparation

The gold electrodes to be modified were firstly cleaned by cyclic voltammetry in 1 mol/L sulphuric acid, rinsed with ethanol and dried with nitrogen, after which they were placed directly in a solution of 1 mmol/L GSH (Aldrich) or cysteine (Aldrich) in deonised water. The self-assembled monolayer was formed by maintaining the electrodes immersed in the solution between 10 minutes and 16 hours for the GSH and between 15 minutes and 48 hours for the cysteine, at room temperature and in an air tight container to prevent any water evaporation. The surfaces of the electrodes were then rinsed in water to remove any unattached thiol residue.

Electrochemical characterisation of the SAM was performed in a one-compartment cell using the modified gold electrode as a working electrode, a platinum flag as the counter electrode and a Ag/AgCl reference electrode. CVs and impedance were conducted on 1 mmol/L $K_3[Fe(CN)_6]$ (Aldrich) in phosphate buffered solution (PBS, potassium phosphate monobasic and potassium phosphate dibasic from Aldrich in deionised water) containing 0.04 mol/L of proline (Adrich).

DNA self-assembled monolayer preparation

The gold electrodes to be modified were firstly cleaned by cyclic voltammetry in 1 mol/L sulphuric acid, rinsed with distilled water and dried with nitrogen, after what they were placed directly in a solution of 40 µmol/L oligonucleotide (Aldrich) in 20 µmol/L PBS solution (pH=7.4) containing 0.2 mol/L of NaCl (Aldrich). The self-assembled monolayer was formed by maintaining the electrodes immersed in the solution for 48 hours at room temperature and in an air tight container to prevent any water evaporation. The surfaces of the electrodes were then rinsed in water to remove any unattached DNA residue.

Electrochemical characterisation of the SAM was performed in a one-compartment cell using the modified gold electrode as a working electrode, a platinum flag as a counter electrode and a Ag/AgCl reference electrode. CVs and impedance were conducted in 20 µmol/L PBS solution (pH=7.4) containing 0.2 mol/L of NaCl (Aldrich) and 1 mmol/L of $K_3[Fe(CN)_6]$ (Aldrich) or methylene blue (Aldrich).

4. PE Electro-oxidation Results and Discussion

In this chapter, cyclic voltammetry is used to show how the (-)-sparteine affected the enantioselectivity of the PE oxidation. It starts with an electroanalysis of the two catalysts involved in the reaction, TEMPO and (-)-sparteine, in order to compare their individual behaviour on gold, platinum and glassy carbon electrodes. The enantioselectivity of the PE oxidation in the presence of (-)-sparteine is then discussed from CV analysis performed at various scan rates on platinum and gold bare electrodes and on a gold microelectrode array. An attempt to improve the selectivity by immobilising the TEMPO radical at the surface of the electrode is also presented in the last part of this chapter. To do so, proDOT and pyrrole were electropolymerised on metal electrodes and polyacrylic acid was polymerised and functionalised at the surface of a glassy carbon electrode.

4.1. INTRODUCTION

The selective electro-oxidation of (1)-phenylethanol (PE) in the presence of TEMPO and (-)-sparteine in bulk solution was investigated in this chapter. The purpose was to characterise the efficiency of enantioselectivity when the nitroxyl radical and the chiral base are in bulk solution, as opposed to using a chirally modified nitroxyl radical immobilised at the electrode surface[63,70]. This study was of interest to simplify the electroanalytical process. It involved no nitroxyl radical immobilisation at the surface of the electrode and all the reactants were commercially available. The literature presents similar set ups for chiral sensing with variable results. This research intended to establish the reliability of the enantioselective oxidation induced by (-)-sparteine and to extend it to different electrode materials. The ultimate objective was to use a microelectrode array (MEA) as a chiral sensor.

The selectivity of the reaction was quantified by the differences of oxidation current and potential between the enantiomers, which were extracted from CV analysis. The disc working macroelectrodes considered were glassy carbon (Ø = 3 mm), platinum (Ø = 2 mm) and gold (Ø = 1.6 mm). These were compared in order to identify possible adsorption of the catalyst at the surface of carbon or metal electrode. Furthermore, the comparison determined the choice of the most appropriated metal for the microdevice.

The CV analyses of the PE oxidation were performed in acetonitrile and the electrolyte was $NaClO_4$. The potential window defined by this background solution is shown in the following graph:

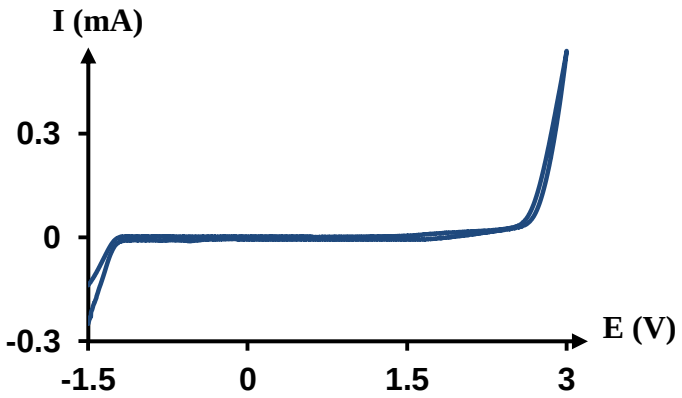

CV of $NaClO_4$.in acetonitrile (1 mol/L) using Pt working electrodes and Pt pseudo reference. Scan rate 100 mV/s.

All potentials reported in this chapter were measured versus the Pt wire pseudo reference (the ferrocene had a potential of 0.6 V relative to Pt).

4.2. TEMPO CHARACTERISATION

In this study, it was essential to perform preliminary experiments on the individual components in order to characterise them and their behaviour at the different electrode surfaces. The radical catalyst was TEMPO and the first experiments consisted of identifying its response and comparing it with literature. These analyses were also used to prove non adsorption of the catalyst at the surface of the electrode.

Fig. 44 shows the TEMPO radical and its cationic form after oxidation. Fig. 45 shows the CV voltammogram of TEMPO supported by Au, Pt and GC macroelectrodes.

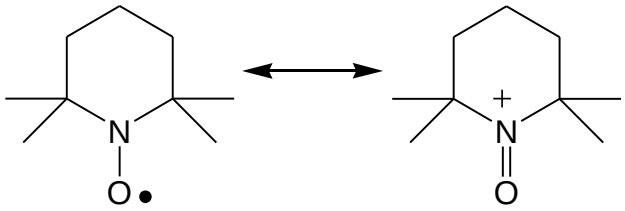

Fig. 44. TEMPO oxidation structures.

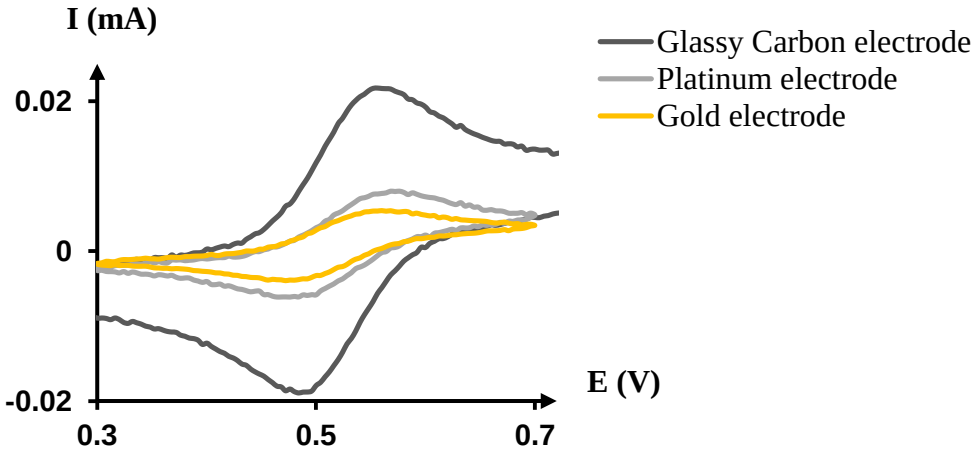

Fig. 45. CV of TEMPO (0.5 mmol/L) in acetonitrile (electrolyte $NaClO_4$, 0.1 mol/L) for GC, Pt and Au working electrodes. Scan rate 100 mV/s.

The same platinum pseudo reference was used in the three measurements. For all materials tested, the voltammogram exhibited a well-defined reversible wave at 0.52 V corresponding to the characteristic one-electron electrochemically reversible oxidation and then reduction of the TEMPO radical. The difference of amplitude between the three voltammograms was due to the difference of surface area between the gold, GC and platinum electrodes. The anodic peak intensities were 22 µA for the GC electrode, 8 µA for the platinum electrode and 5 µA for the gold electrode.

Those values followed the Randles-Sevcik equation (Eq. 5) where $I_{pa} = 2.69 \times 10^5 z^{3/2} CAD^{1/2} \nu^{1/2}$, with the electrode surface areas being 7×10^{-4} dm^2 for GC, 3×10^{-4} dm^2 for platinum and 2×10^{-4} dm^2 for gold. The diffusion coefficient value of TEMPO in acetonitrile[118] was 2.15×10^{-7} dm^2/s. The difference between the anodic and cathodic peak potential was 64 mV for the GC electrode, 90 mV for the platinum electrode and 68 mV for the gold electrode. Those values were slightly higher than the standard difference for a one-electron transfer reaction, which is 59 mV. These variations were attributed to the uncompensated ohmic drop iR and kinetics variations.

TEMPO is the redox active species in the PE oxidation process. It needs to be oxidised to be active and therefore it is often adsorbed or covalently attached directly to the electrode surface. In this study the activity of the TEMPO catalyst in solution was investigated. Running CVs at different scan rates gave information about transfer kinetics between the redox species and the surface of the electrode. When the analyte is in solution and not adsorbed at the metal substrate, the anodic and cathodic peak increase proportionally to $\sqrt{\nu}$ as expressed in the Randles-Sevcik equation (Eq. 5), where $I_{pa} = 2.69 \times 10^5 z^{3/2} CAD^{1/2} \nu^{1/2}$. In the case of adsorption of the analyte at the surface of the electrode the peak intensities are directly proportional to the scan rate. In addition, immobilisation on the electrode is also translated in the CV by a change of potential difference between the two peaks due to the modification of the diffusion layer. For fully absorbed redox species the peak potential difference is lower than the standard 59 mV value typically observed for a reversible redox process in solution.

Fig. 46 shows the CV of TEMPO in background solution for a scan rate varying between 10 and 300 mV/s.

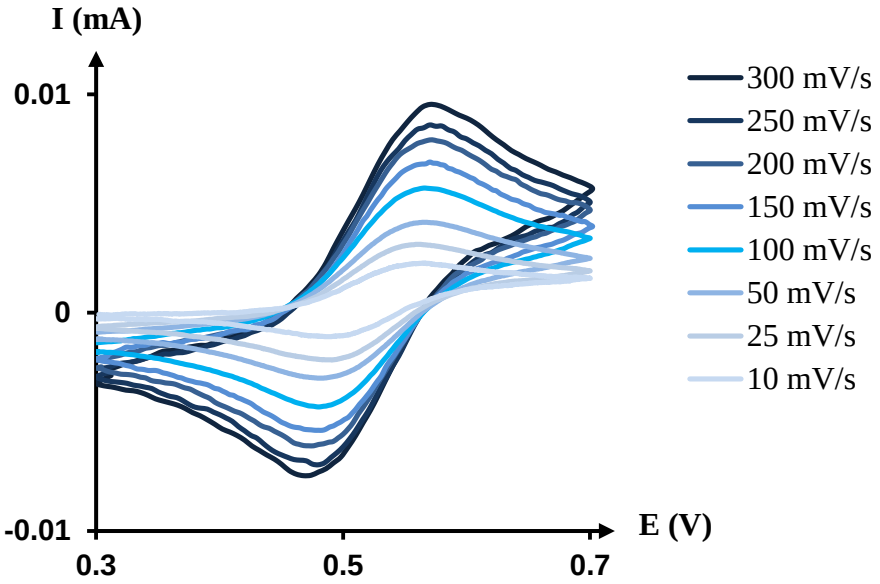

Fig. 46. CV of TEMPO (0.5 mmol/L) in acetonitrile (electrolyte $NaClO_4$, 0.1 mol/L) at different scan rates with a Pt working electrode.

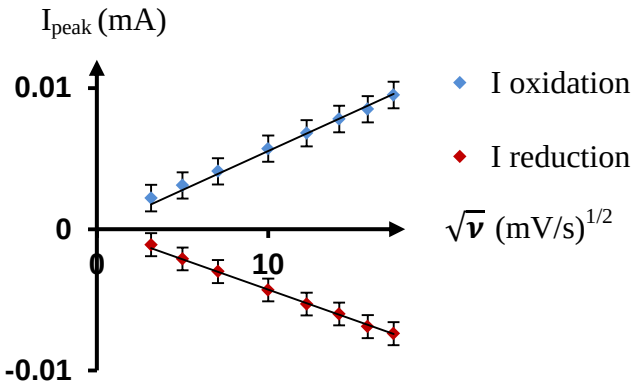

Fig. 47. Relation between $\sqrt{\nu}$ and I_{peak} for CV of TEMPO (0.5 mmol/L) in acetonitrile (electrolyte $NaClO_4$, 0.1 mol/L), on Pt working electrode.

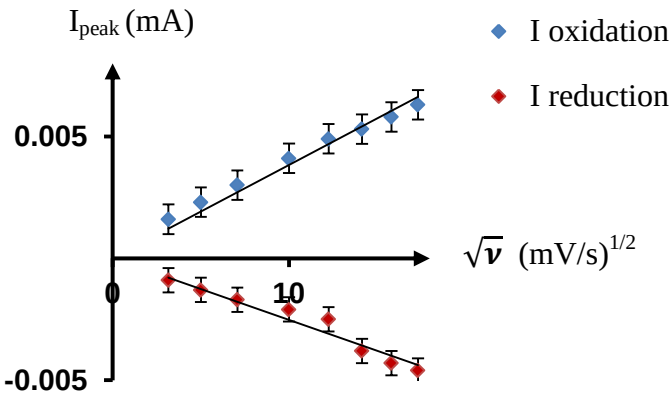

Fig. 48. Relation between $\sqrt{\nu}$ and I_{peak} for CV of TEMPO (0.5 mmol/L) in Acetonitrile (electrolyte $NaClO_4$, 0.1 mol/L), on Au working electrode.

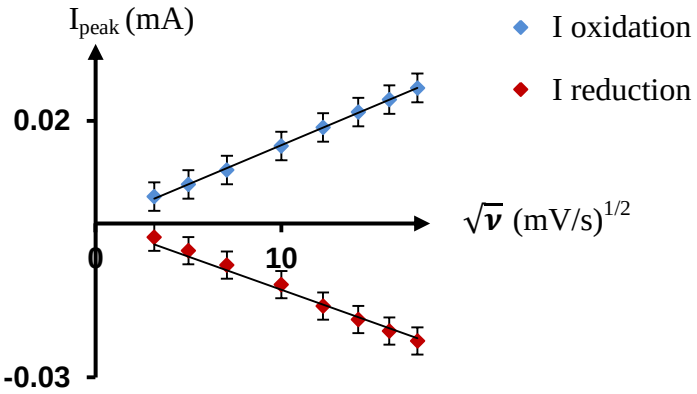

Fig. 49. Relation between $\sqrt{\nu}$ and I_{peak} for CV of TEMPO (0.5 mmol/L) in Acetonitrile (electrolyte $NaClO_4$, 0.1 mol/L), on GC working electrode.

Fig. 47, Fig. 48 and Fig. 49 verified the linear relation between the intensity of the peaks and $\sqrt{\nu}$ for platinum, gold and GC electrodes. This relation plus the invariable standard 59 mV difference between the peaks potential confirmed that there was no perceptible adsorption of TEMPO at the electrode and that the process was diffusion controlled.

4.3. (-)-SPARTEINE CHARACTERISATION

In the same manner, prior to being used in the PE oxidation, the (-)-sparteine catalyst was characterised and analysed via CV, in background solution, for each electrode material. Fig. 50 shows the cyclic voltammogram of (-)-sparteine for GC, Au and Pt electrodes.

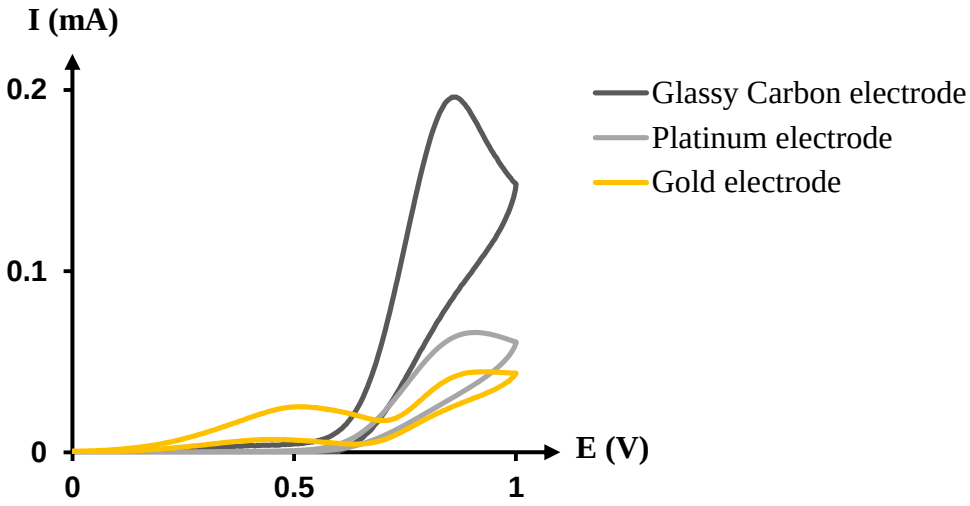

Fig. 50. CV of (-)-Sparteine (0.01 mol/L) in Acetonitrile (electrolyte $NaClO_4$, 0.1 mol/L) for GC, Pt and Au working electrode. Scan rate 100 mV/s.

For Pt and GC electrode, the voltammogram exhibited a well-defined irreversible peak at 0.85 V due to the oxide formation promoted by perchlorates (weak oxidant) in the presence of a proton abstracting base. The difference between the peaks' amplitude was again due to the difference of surface area between the working electrodes.

Fig. 50 illustrated that for the gold electrode an extra peak appeared at 0.5 V in addition to the peak at 0.85 V, indicating a spare irreversible electron loss. This additional oxidation happened in the same potential range as the TEMPO. If both sparteine and TEMPO were used in PE oxidation, the oxide formation happening at 0.5 V could not be avoided and the nitroxyl catalyst activity would be compromised. To remove this superfluous activity, a change of electrolyte was considered. Initially the analyses were conducted for 0.01 mol/L of (-)-sparteine in acetonitrile containing 0.1 mol/L of $NaClO_4$ electrolyte. This occurrence of an extra electron transfer in the presence of gold could be

suppressed by replacing the $NaClO_4$ electrolyte by $NaPF_6$ which had comparable potential windows (Fig. 51).

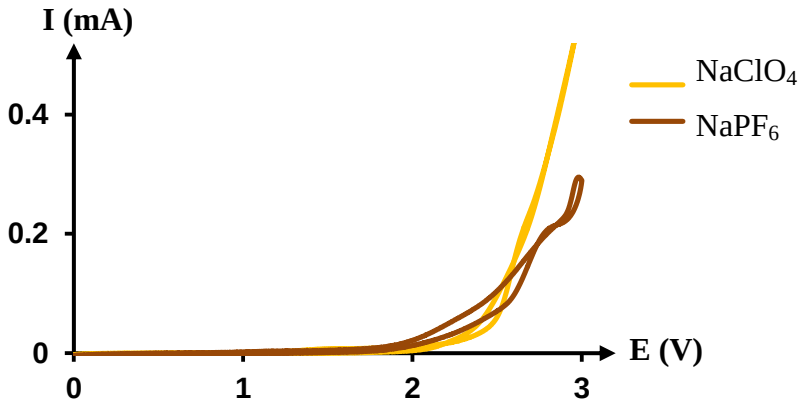

Fig. 51. CV of backgrounds for $NaClO_4$ and $NaPF_6$ electrolytes (0.1 mol/L), with a Au working electrode and a scan rate of 100 mV/s.

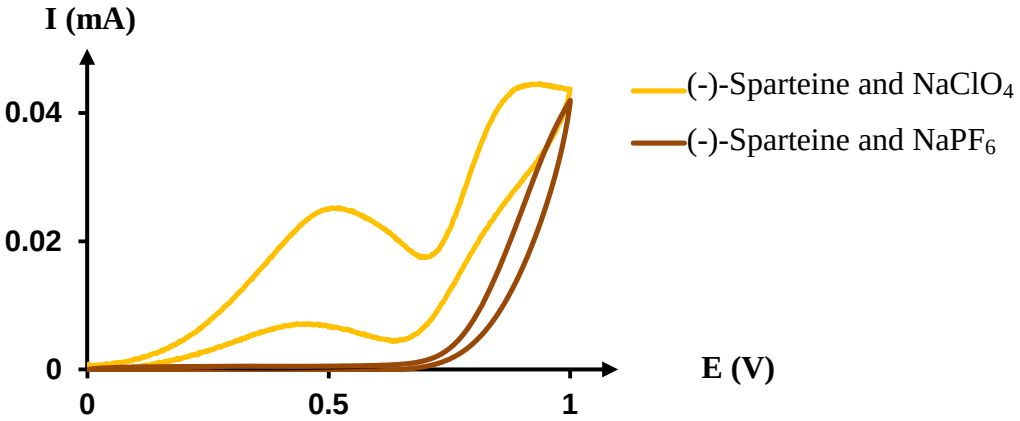

Fig. 52. CV of (-)-Sparteine (0.01 mol/L) in Acetonitrile for $NaClO_4$ and $NaPF_6$ electrolytes (0.1 mol/L) with a Au working electrode and a scan rate of 100 mV/s.

Fig. 52 shows that replacing $NaClO_4$ by $NaPF_6$ did make a difference and helped prevent the oxide formation at 0.5 V.

4.4. PE ENANTIOSELECTIVE OXIDATION

The reaction considered was the electro-oxidation of PE catalysed by the TEMPO nitroxyl radical in the presence of the chiral base (-)-sparteine. The reaction mechanism[44-49] is showed in Fig. 53.

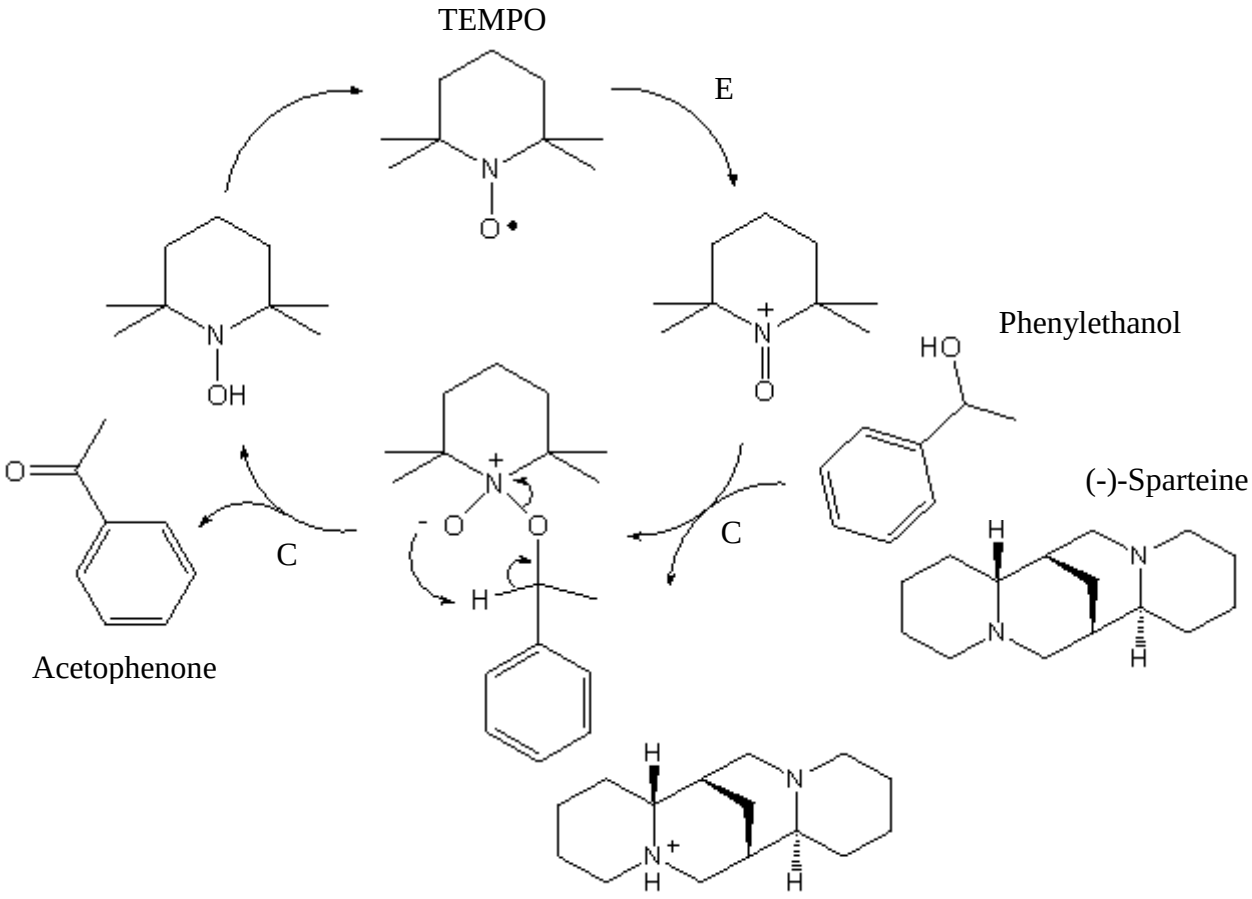

Fig. 53. Mechanism of the PE electro-oxidation reaction.

The reaction can be described as an *ECC* process where the reaction is initiated by an electrochemical (*E*) oxidation and followed by two chemical reactions (*CC*). The molar ratio between the PE analyte and the base is 1:1. There is no exact number in the literature for the optimum molar ratio between the analyte and the nitroxyl catalyst, with values between 20 to 40 mole of analyte for one mole of nitroxyl being quoted.

The relevance of considering the base to be the chiral catalyst instead a chiral modified nitroxyl radical was to determine if selectivity could be driven by the interaction with the base instead of interaction with the nitroxyl. The chiral (-)-sparteine base was expected to enantioselectively accept the proton of one PE enantiomer rather than the other one.

The first PE electro-oxidation was performed in standard conditions, using the non-chiral base lutidine, in the presence of TEMPO. Fig. 54 shows the voltammogram obtained for the electro-oxidation of (-) and (+)-PE in the presence of TEMPO and lutidine in acetonitrile containing $NaClO_4$ electrolyte. The two voltammograms were very similar and no difference in peak intensity was noticed other than normal experimental variation.

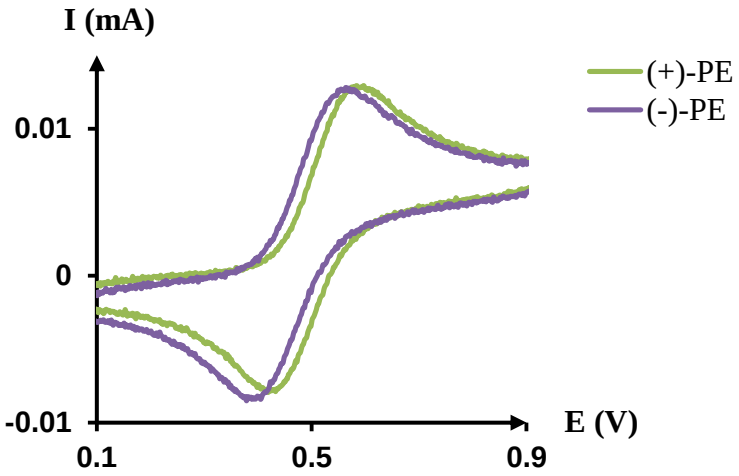

Fig. 54. CV of (-)-PE and (+)-PE in the presence of TEMPO, lutidine and $NaClO_4$ in acetonitrile at a Pt working electrode.

The (-) and (+)-PE were then oxidised in the presence of TEMPO and (-)-sparteine in acetonitrile containing the $NaPF_6$ electrolyte and supported by platinum and gold working electrodes. The CV analyses were conducted for different scan rates. Fig. 55 and Fig. 57 show the CV responses of (-) and (+)-PE at a scan rate of 100 mV/s at, respectively, gold and platinum electrodes. Fig. 56 and Fig. 58 show the responses for scan rates varying between 20 and 150 mV/s.

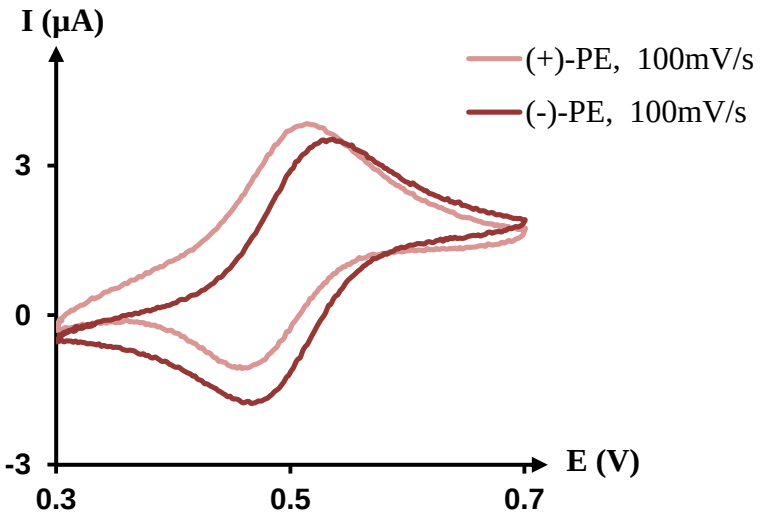

Fig. 55. CV of (-)-PE and (+)-PE in the presence of TEMPO, (-)-sparteine and $NaPF_6$ in acetonitrile at a Au working electrode.

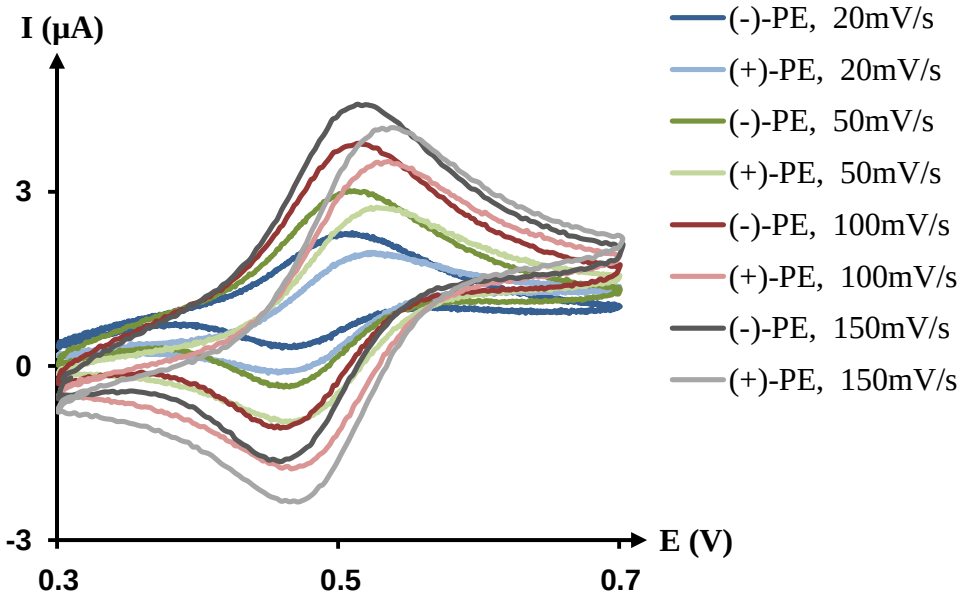

Fig. 56. CV of (-)-PE and (+)-PE in the presence of TEMPO, (-)-sparteine and $NaPF_6$ in acetonitrile for various scan rates at a Au working electrode.

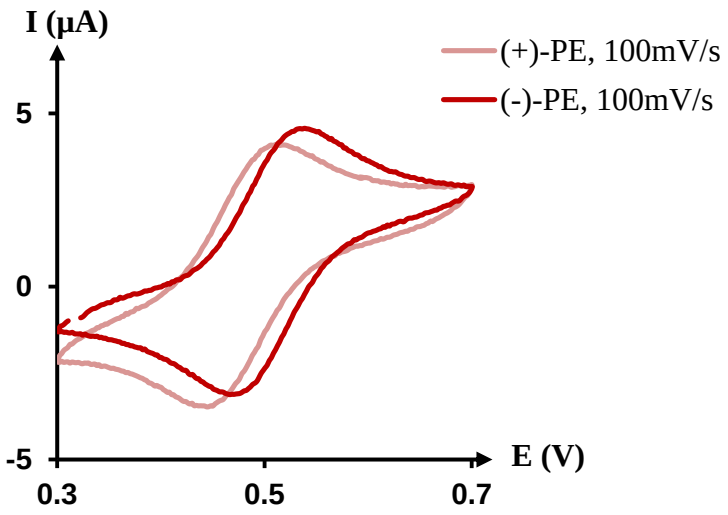

Fig. 57. CV of (-)-PE and (+)-PE in the presence of TEMPO, (-)-sparteine and $NaPF_6$ in acetonitrile at a Pt working electrode.

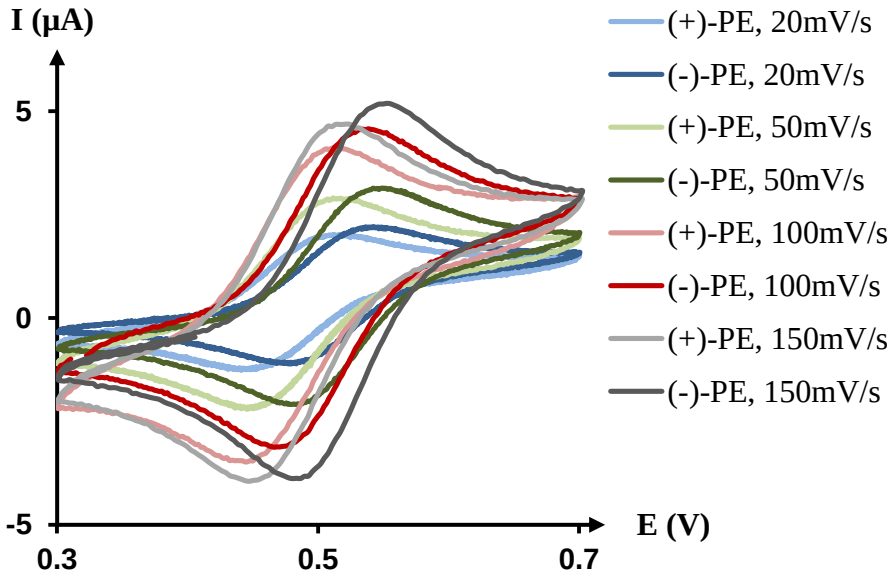

Fig. 58. CV of (-)-PE and (+)-PE in the presence of TEMPO, (-)-sparteine and $NaPF_6$ in acetonitrile for various scan rates at a Pt working electrode.

The chiral discrimination of the reaction was characterised by the differences between the anodic peak values, $I_{Peak\ Anodic}$, and the difference between the peak potentials, E_p, of the (-) and (+)-PE voltammograms (Fig. 59).

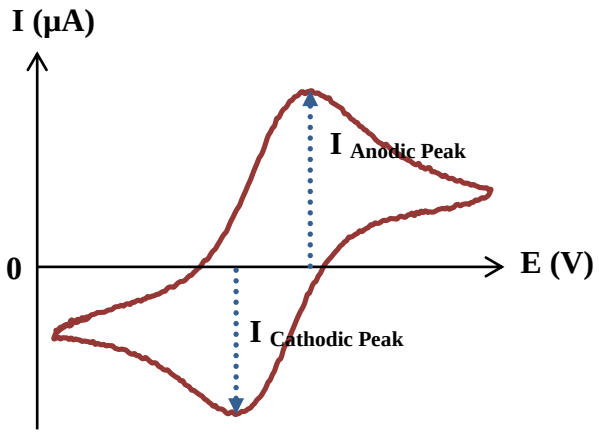

Fig. 59. Peak current measurements.

4.4.1. Enantioselectivity based on Peak Current Difference

The difference between the peak intensity of the enantiomers' responses was quantified by the ratio between the anodic peak difference ($\Delta I_{peak(-)(+)} = I_{peak(-)} - I_{peak(+)}$) and the anodic peak current of the (+)-PE, $I_{peak(+)}$ [55]. Fig. 60 and Fig. 61 present those ratios as a function of the scan rate.

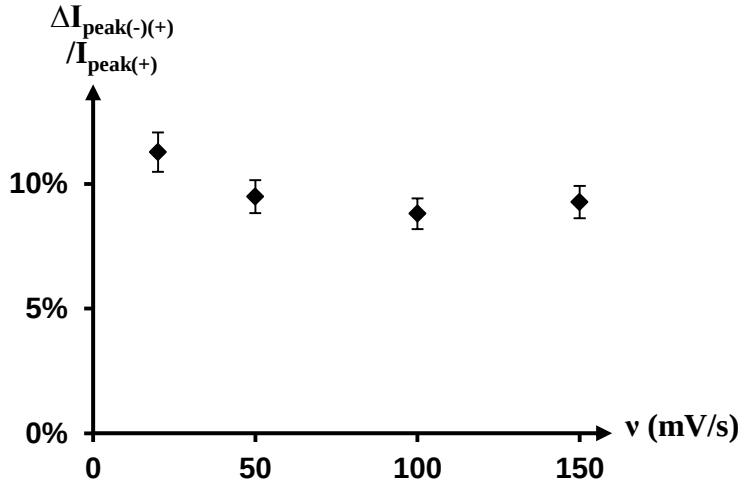

Fig. 60. Peak current intensity difference between (-) and (+)-PE for the gold electrode.

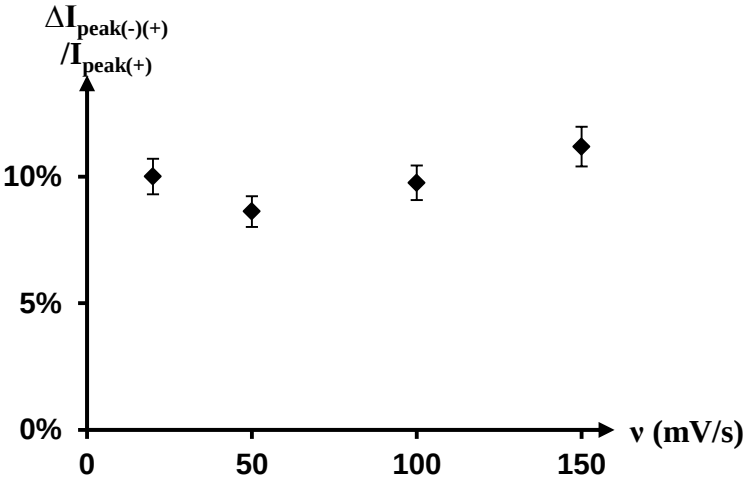

Fig. 61. Peak current intensity difference between (-) and (+)-PE
for the platinum electrode.

Results showed selectivity, up to 10%; limited but yet reproducible and noticeable in comparison with the PE oxidation in the presence of lutidine. The (-)-sparteine interacted preferentially with the (-)-PE. No difference of selectivity was noticed between platinum and gold electrodes. The graphs also illustrated that the selectivity remained constant between low and high scan rates. This profile demonstrated that the kinetic of the reaction was fast, and the use of high scan rate did not prevent the selective interactions between (-)-PE and (-)-sparteine.

4.4.2. Enantioselectivity Based on Peak Potential Difference

The progress of an electrochemical reaction can be followed by the transition state theory[1]. Underlying this concept is the fact that reactions proceed through a well defined transition state reached, where the reaction rate *k* and the standard free energy of activation $\Delta G^{\#}$ are defined as shown in Eq. 29. By replacing $\Delta G^{\#}$ with its electrochemical expression, the reaction rate can be expressed as a function of the potential (Eq. 30).

Eq. 29 $$k = A' e^{-\Delta G^{\#}/RT}$$

where *k* is the rate constant (s^{-1}), *A'* is the frequency factor (s^{-1}), $\Delta G^{\#}$ is the standard free energy of activation ($J.mol^{-1}$), *R* is the gas constant ($J.mol^{-1}.K^{-1}$) and *T* is the temperature (K).

Eq. 30 $$k = A' e^{-nFE^{\#}/RT}$$

where $E^{\#}$ is the transition state potential (V), *n* the number of electron involved in the process and *F* the faraday constant ($C.mol^{-1}$).

The calculation of the rate transfer of the PE oxidation is complex as implied by the reaction mechanism. However, Eq. 30 shows that differences in potential indicate differences in reaction rates, and consequently differences in activation energy.

CV analyses of the PE oxidation (Fig. 55 and Fig. 57) showed that the transition state of the enantiomers was reached at different potentials. The peak potential of the (-)-PE was higher than the (+)-PE one. Those differences were calculated following Eq. 31 and were plotted versus the scan rates, for Pt and Au electrodes (Fig. 62).

Eq. 31 $$\Delta E_{(-)/(+)} = E_{pa(-)\text{-}PE} - E_{pa(+)\text{-}PE}$$

where $E_{pa(-)\text{-}PE}$ is the anodic potential peak of the (-)-PE and $E_{pa(+)\text{-}PE}$ is the anodic potential peak of the (+)-PE.

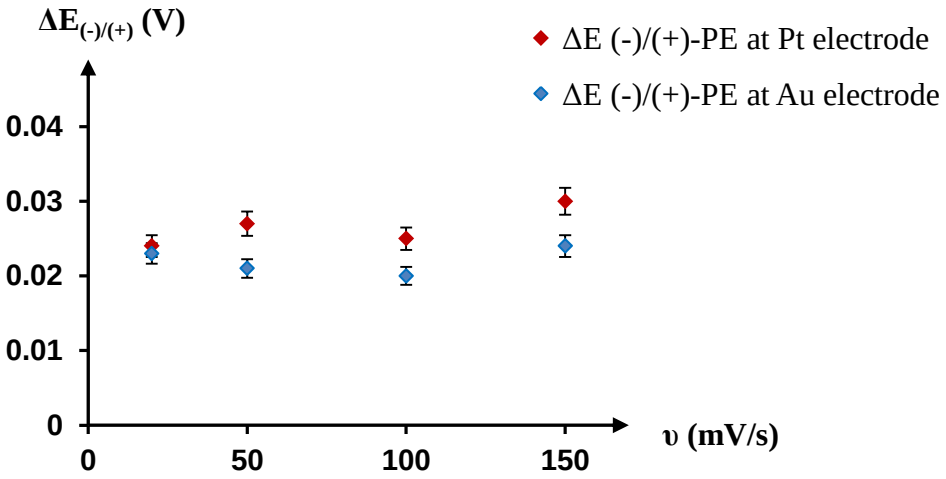

Fig. 62. Differences between the anodic peak potential of (-)-PE and (+)-PE at Au and Pt electrode.

$\Delta E_{(-)/(+)}$ was constant for varying scan rates and the average difference was 25 mV at Pt electrode and 21 mV at Au electrode. This difference of potentials showed that, in the presence of TEMPO and sparteine catalysts, the oxidation of (+)-PE required less activation energy than the (-)-PE oxidation (Fig. 63). The differences in reaction rates and activation energy were accessible in CV analyses and could be used for chiral separation and recognition.

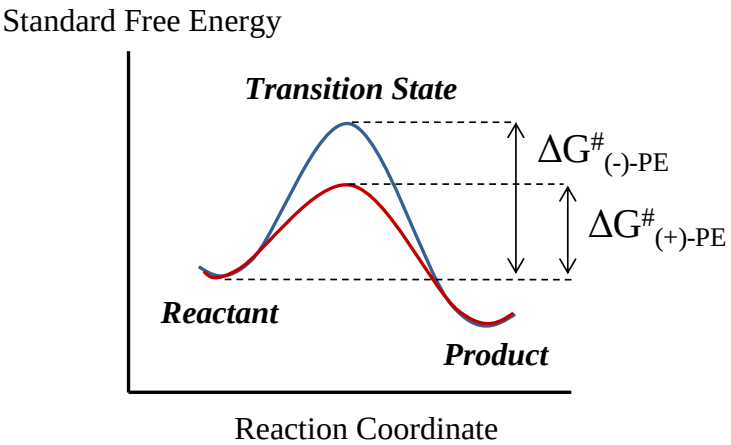

Fig. 63. Free energy changes during a reaction.

4.4.3. Enantioselectivity at MEA

The ultimate objective of the chiral sensing was to have it performed by a microarray. Reducing the scale of the electrode from macro to micro allows an increase in the analysis sensitivity and the minimisation of chemical waste. The current measured through a microelectrode array is translated into a sygmoidal shaped voltammogram, where the steady state $I_{ss} = n4zFDCae^{(-0.96L/a)}$ (Eq. 11).

A gold microelectrode array (MEA) made of 306 microdisc (Ø = 45 µm), was fabricated in collaboration with the School of Engineering and Computing Sciences for this purpose. Its fabrication, optimisation and characterisation are discussed in chapter 5.

Fig. 64 shows the response of the microelectrode array for the electro-oxidation of (-) and (+)-PE in the presence of (-)-sparteine and TEMPO in acetonitrile containing $NaPF_6$.

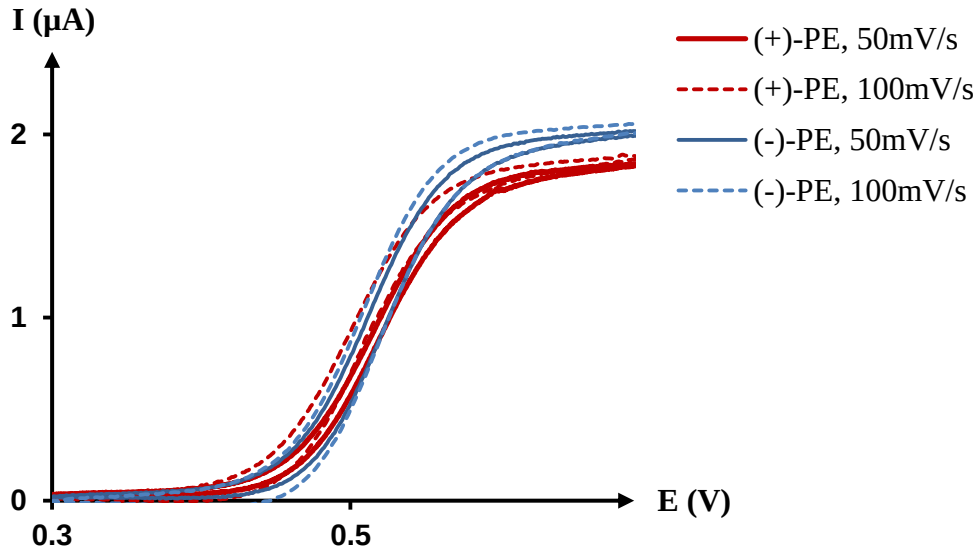

Fig. 64. CV of (-)-PE and (+)-PE in the presence of TEMPO, (-)-sparteine and $NaPF_6$ in acetonitrile for various scan rates using MEA working electrode.

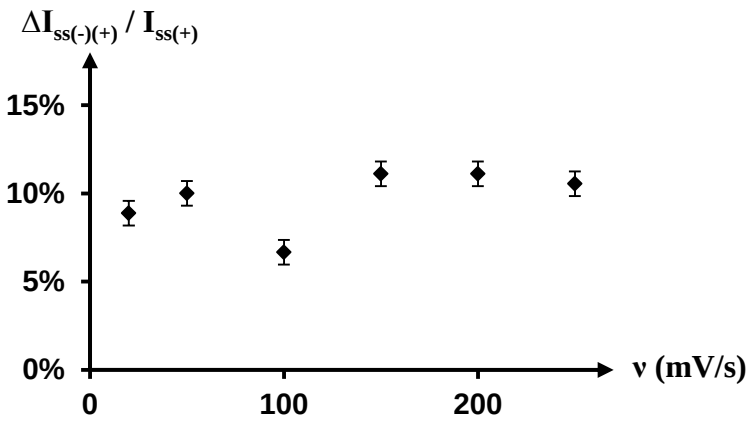

Fig. 65. Peak intensity difference between (-) and (+)-PE for the MEA.

As expected, the steady state current of the CV response remained constant with scan rate variations, which illustrated the good behaviour of the microelectrode array.

The selectivity obtained with the microelectrode (Fig. 65) was comparable with the one obtained with the macroelectrodes (Fig. 60 and Fig. 61). The current response of the (-)-PE enantiomer was in average 10% higher than the current response of (+)-PE with percentage values comprised between 7 and 11%, for scan rates ranging between 20 and 250 mV/s. This difference represented a 30 % increase of the diffusion coefficient of the (-)-PE in comparison with the (+)-PE. The low percentage obtained for the 100 mV/s scan rate was not representative of any peculiar behaviour other than experimental anomaly. Likewise the results obtained at macroelectrodes, no noticeable variation of selectivity was noticed when increasing the scan rate.

These results illustrated that the enantioselectivity of the PE electrooxidation resulting from preferential interaction between (-)-sparteine and (-)-PE could be detected at MEA. The dimensions of the electrodes could be reduced to have a minimum chemical waste, while maintaining the sensing efficiency.

The use of microelectrodes proved to be well adapted to this application and the absence of peaks made it easy to compare the different current responses.

At this end of this part, the factors retaining the selectivity could be the two following:

- The limited interaction between the chiral base, (-)-sparteine, and the PE.
- The fact that the nitroxyl radical was in solution and not directly adsorbed at the surface of the electrode.

4.5. SURFACE MODIFICATION

For most electrocatalytic processes, the stability and action of the catalyst can be enhanced by immobilising the electroactive species at the surface of the electrode. The immobilisation of the nitroxyl catalyst at the surface of the electrode was investigated in an attempt to improve its stability and, overall, the selectivity of the PE oxidation. The procedures for surface modification were chosen based on the equipment accessibility and the robustness and straightforward behaviour of the process. Surface modifications involving heavy organic chemistry or requiring multiple surface treatments were not adapted to our purpose. The metal electrode surfaces were modified by electropolymerisation. The chemical polymerisation of polyacrylic acid substituted with TEMPO derivative was used to modify the glassy carbon electrode.

4.5.1. TEMPO Entrapping during Electropolymerisation

The first tests were performed on a gold macroelectrode. Electropolymerisation is a very common way to modify the electrode surface with a very robust film[119] that is removable by soft polishing. It takes place in the presence of electrolytes, where anions are trapped in the resulting polymer[120]. This entrapping step is of interest for surface modification as the catalyst might occupy those free cavities and be entrapped itself.

Difficulty concerning this attempt was due to the positive charge of the TEMPO molecule (Fig. 44). Whereas the spontaneous trapping of anions happens during the polymerisation, entrapping of cations would not be directly expected. Even so, this process remained of interest as only a small quantity of nitroxyl would be necessary to assure the catalytic effect during the PE oxidation (less than 0.025 molar eq.). Thus, even partial entrapping could ensure proper activity of TEMPO.

No formal protocol was found for this particular purpose. The monomer chosen to be supporting TEMPO was propylenedioxythiophene (proDOT), the electropolymerisation of which is described in the literature[121,122] (Fig. 66).

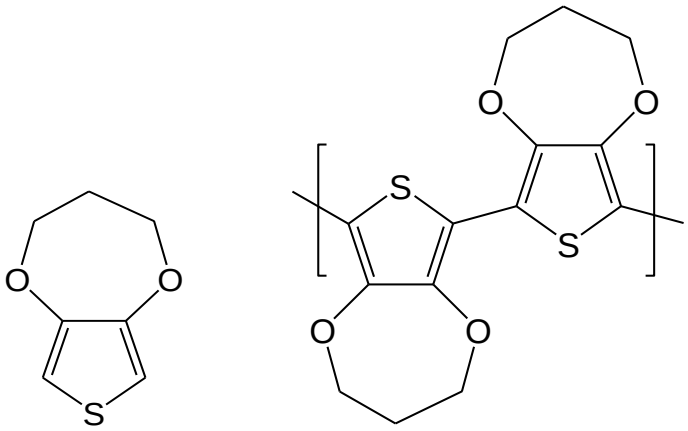

Fig. 66. Poly Propylenedioxythiophene.

The proDOT electropolymerisation was performed in the presence of TEMPO. Fig. 67 shows the current answer of the ProDOT monomer and TEMPO while the conductive polymer was growing at the surface of the electrode. As expected, the current increased with the potentiodynamic growth of ProDOT film. The TEMPO oxidation and reduction also appeared on the voltammogramm as shown in the enlargement of Fig. 67.

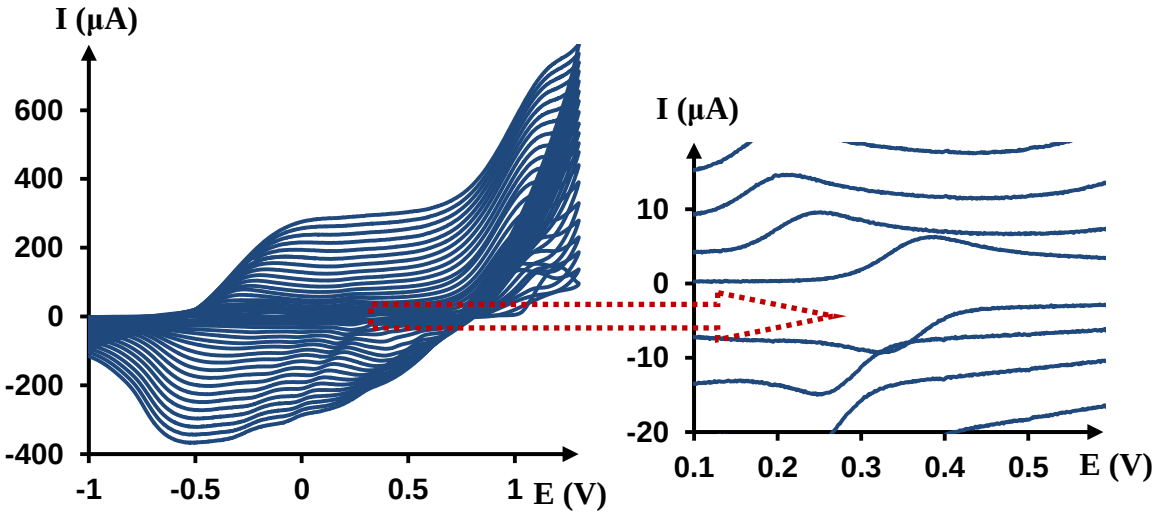

Fig. 67. CV voltammogram for electropolymerisation of ProDOT (0.01 mol/L), in the presence of TEMPO, $LiClO_4$ in acetonitrile.
Au bare electrode vs Pt pseudo ref, 50 mV/s, 20 cycles.

The modified electrode was rinsed in acetonitrile before further analysis to remove any loose catalyst molecule. The presence of any remaining TEMPO in the polymer was verified by running CV in background solution containing $NaClO_4$ salts only (Fig. 68). The absence of peaks around 0.52 V demonstrated the absence of TEMPO in the ProDOT film.

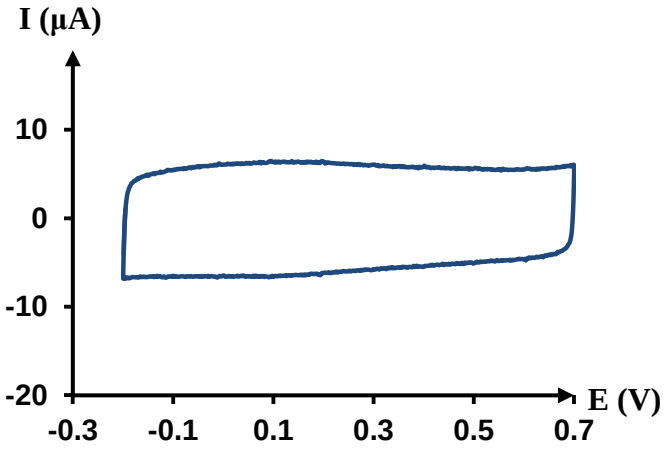

Fig. 68 CV voltammogram of modified Au bare electrode in $NaClO_4$ (0.1 mol/L) in CH_3CN, vs Pt pseudo ref, 50 mV/s.

The film thickness was reduced to ensure that no redox peak of small intensity was present. This confirmed the absence of a peak. More experiments were performed using different molar equivalents between salt, monomer and TEMPO. Any influence of those variations on the TEMPO entrapping would indicate a possible competition between the ions to access the polymer cavities. The concentration of the $LiClO_4$ salt was decreased, while the amount of TEMPO was increased.

ProDOT	**$LiClO_4$**	**TEMPO**
1	10	0.1
1	5	1
1	2	10

Table 1. Molar equivalents between the chemicals during ProDOT electropolymerisation.

The fact that no improvement was noticed over those ratio changes indicated that the lack of affinity between ProDOT and TEMPO prevented the ion entrapment.

The pyrrole monomer was also tested in order to polymerise a film (Fig. 69) having different possible interactions with the TEMPO ions. Used in the same conditions, it showed no better results and no catalyst was detected by CV after the polymerisation and the rinsing steps.

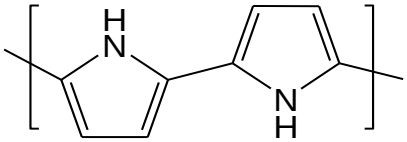

Fig. 69. Polypyrrole.

No strong interactions or bond creation could immobilise the pure TEMPO molecule or entrap it in the polymer.

4.5.2. TEMPO Derivative Bounded to Polyacrylic Acid

The modification of glassy carbon or graphite felt electrode using polyacrilic acid (PAA) is also very common[45]. The PAA polymer is stable and robust. It attaches itself covalently to the electrode surface during the polymerisation and is afterwards functionalised with the desired chemical to give it more properties.

A derivative of TEMPO, the 4-aminoTEMPO was used to functionalise the PAA, using the amide linkage 1-ethyl-3-(3dimethylamino-propyl)-carbodiimide hydrochloride (EDC or WSC). The EDC is a zero-length crosslinking agent used to form amides from carboxyl groups and primary amines. The mechanism of the reaction is showed in Fig. 70. The reaction between the PAA and the WSC is rapid and results in the formation of an O-acylisourea intermediate. The O-acylisourea reacts with the 4-aminoTEMPO to form an amide bridge and immobilise the nitroxyl catalyst at the carbon surface.

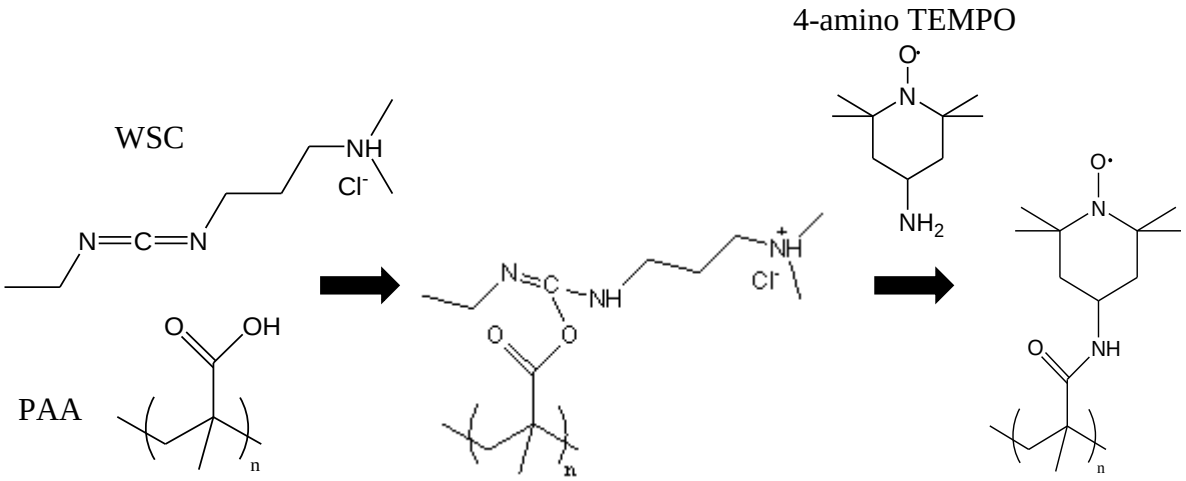

Fig. 70. GC surface modification with PAA and 4-aminoTEMPO.

The immobilisation of 4-amino TEMPO at the surface of the electrode was established by CV analysis in background solution containing $NaClO_4$ electrolyte only. Fig. 71 shows the voltammogram with the characteristic reversible peak of TEMPO, proving the presence of the radical at the surface of the electrode.

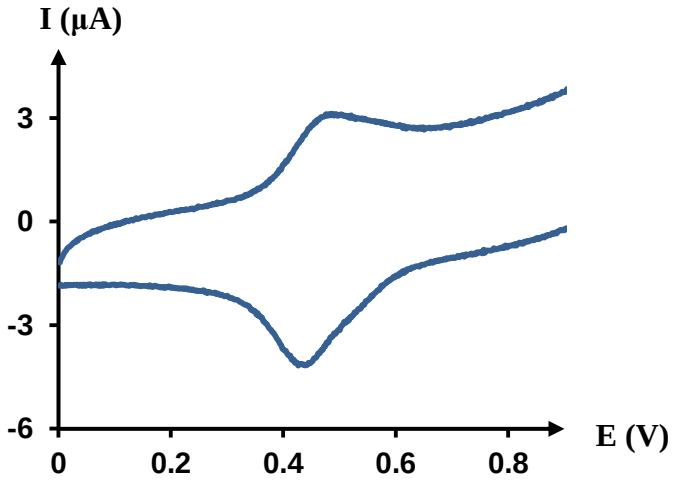

Fig. 71. CV voltammogram of modified GC bare electrode in $NaClO_4$ (0.1 mol/L) in CH_3CN, 100 mV/s.

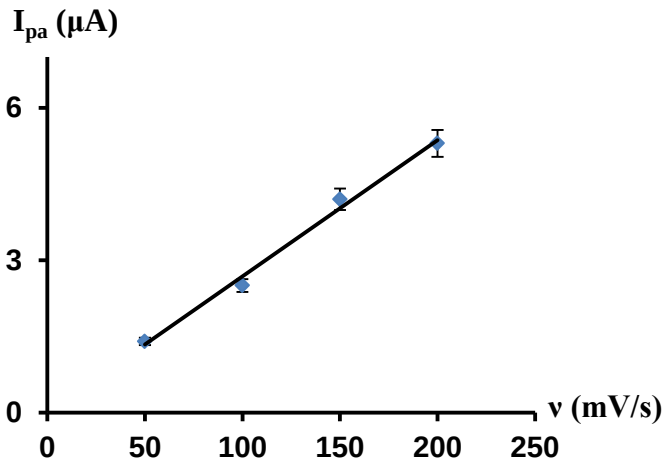

Fig. 72. Relation between the scan rate and I_{peak} for CV of modified GC electrode in acetonitrile (electrolyte $NaClO_4$, 0.1 mol/L).

The CV analysis was performed for different scan rates. As mentioned earlier, in the case of adsorbed species the peak intensity should be directly proportional to the scan rate. Fig. 72 shows that the GC electrode was properly modified and the TEMPO derivative properly adsorbed at its surface.

The robustness of the layer was tested by immersing the modified electrode in solvent for different times and performing CV analyses to control the changes. After 3 hours in solvent, the anodic peak intensity was three times less than the initial value, which proved that the system was stable. The first signs of instability of the layer appeared for applied potentials $\geq$ 1.2 V.

Fig. 73 shows the CV analysis of the electro-oxidation of (-)- and (+)-PE in the presence of (-)-sparteine in acetonitrile containing $NaClO_4$ and using the modified electrode.

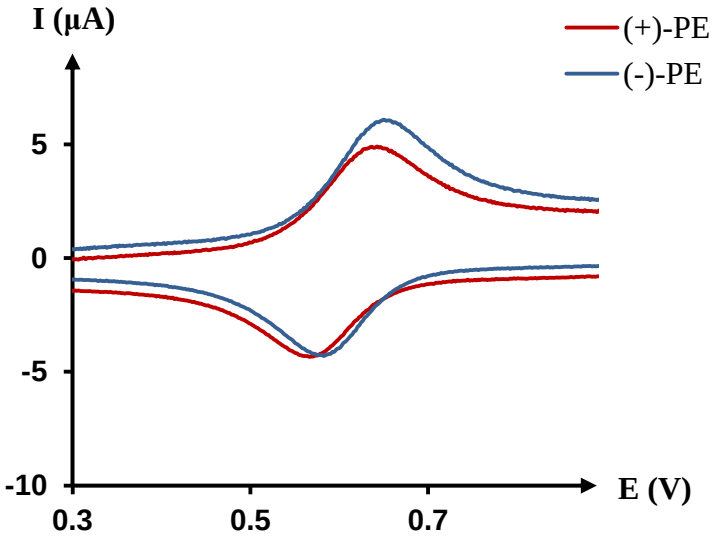

Fig. 73. CV of (-)-PE and (+)-PE in the presence of (-)-sparteine and $NaPF_6$ in acetonitrile for various scan rates with a TEMPO modified working electrode.

Results showed that the selectivity between the two enantiomers was not improved when the TEMPO was immobilised at the surface of the electrode. It could be concluded that using the TEMPO catalyst in solution rather than adsorbed at the electrode was not the reason for the limited enantioselectivity of the reaction.

4.6. CONCLUSION

The activity of the (-)-sparteine as a chiral agent appeared to be limited whether the TEMPO was in bulk solution or immobilised at the surface of the electrode.
The (-)-sparteine interacted preferentially with (-)-PE. The highest current selectivity at a macroelectrode was about 10% and was obtained for a scan rate of 20 mV/s. This percentage didn't decrease for higher scan rates, showing that the kinetics of the reaction was fast. All scan rates permitted the selective interactions between the chiral base and the (-)-PE to take place. The selectivity percentages and behaviour were similar for both platinum and gold bare electrodes.
CV analyses of the PE oxidation showed that the transition state of the enantiomers was reached at different potentials. This difference of potentials showed that, in the presence of TEMPO and sparteine catalysts, the oxidation of (+)-PE required less activation energy than the (-)-PE oxidation.

The current enantioselectivity was detected using the MEA. The percentage values were comprised between 7 and 11% on average.

The fact that for both bulk and immobilised TEMPO the (-)-sparteine did not evidently affect the orientation of the PE oxidation indicated that the low selectivity was due to the lack of selective interactions between the chiral base and the (-)-PE. It could be concluded that the (-)-sparteine was not active enough as a chiral agent to allow a precise chiral detection of PE via CV analysis.
Furthermore, this outcome could be extended from (-)-sparteine to a chiral base in general used as a chiral catalyst, and the possibility was not excluded that the reaction could only be efficiently orientated when the chiral agent was the nitroxyl catalyst.

The critical points of this study were (i) the use of (-)-sparteine which appeared to be both unstable and reactive in the presence of gold and $NaClO_4$, and (ii) the modification of the metal surface with a nitroxyl derivative. The latter could not be managed as it required complex organic chemistry to synthesis a monomer functionalised with a TEMPO derivative.
The undesired oxide formation happening at the surface of gold electrode in the presence of (-)-sparteine and $NaClO_4$ could be corrected by changing the electrolyte to $NaBF_6$.

Finally, this study illustrated the ability of the microdevice, which was designed and fabricated specifically for this purpose, to perform stable analyses and to detect low concentration variations very accurately.

5. MICRODEVICE FABRICATION AND CHARACTERISATION

For the purposes of both improving the electroanalytical detection and making a more efficient use of chemicals, the scale of the electrochemical cell was reduced from macro to micro dimensions. This chapter describes the fabrication and the characterisation of a microdevice, which consists of an array of 306 microelectrodes, each with a diameter of 45 µm supported by a polydimethylsiloxane (PDMS) slab engraved with microfluidic channels. The fabrication technique used was photolithography. The details of this are described in this chapter in the literature review. The protocol followed for the fabrication is explained and discussed afterwards in the experimental part. The electroanalytical performance of the microdevice was characterised using cyclic voltammetry. The active surface area was determined and it was established that the surface roughness of the electrode had an influence on the final result from the array. Finally, the microdevice was used for flow injection analyses using chronoamperometry and provided the capability to detect small changes of analyte concentration.

5.1. INTRODUCTION

Microelectrode Arrays (MEAs) consist of interconnected electrodes belonging to the same metal layer, where at least one of the surface dimensions of an individual electrode is in the range of 0.1 to 50 μm[10]. Microelectrodes are more sensitive than macroelectrodes, as the signal-to-noise ratio is much higher. Many studies described the correlation between the current and the diffusion layer geometry and thickness at microelectrode array surfaces of various shapes, the most common of these being the microband and the microdisc arrays[9,17,18,21,22,24-26].

In cyclic voltammetry analysis, the current response at microdisc electrodes array is a steady state current, I_{ss}, whose amplitude is $I_{ss} = n4zFDCa$ (Eq. 10). For shallow recessed microdisc electrodes (L/a <1), this equation can be improved further[16] where $I_{lim} = I_{ss}e^{(-0.96L/a)}$ (Eq. 11). To preserve their individual properties, the microelectrodes should be separated enough so that their diffusion layers do not overlap, but are yet close enough to have no surface area waste[15,28,29].

For the purpose of reducing the scale of the electroanalysis a microdevice was fabricated in the School of Engineering, which consisted of a microelectrode array supported by microfluidic channels. The most common technique used in the manufacturing of microelectronic and microfluidic devices is photolithography. This procedure consists of processing photoresist material to transfer the desired electrode pattern from a mask to the surface of a substrate[123-128]. When the surface for patterning is a metal layer, the fabrication involves metallisation. The two metallisation techniques considered were electron-beam (e-beam) evaporation and electroplating.

Coupling microelectrode arrays with microfluidic channels allows for the performance of flow injection analyses (FIA) as well as monitoring the analyte in real time, contrary to sampling analyses. Furthermore, the small overall size of the device requires a minimum amount of analyte to be tested. Simulated and experimental FIA supported by microelectrode arrays have been considered and showed great capability of the systems for diverse electronalytical purposes, and more specifically for chronoamperometric measurements[129,130].

5.2. TECHNICAL BACKGROUND

Microtechnology[126], which is also known as MicroElectroMechanical Systems (MEMS), can be defined as a technique involving dimensions comprised between the micron and the millimetre scale.

The most common technique to process thin layers and manufacture microelectronic and microfluidic devices is photolithography[10,131,132]. Photolithography consists of processing photoresist material to transfer a pattern from a mask to the surface of a substrate. The process involves substrate cleaning, surface insulation, photoresist application, soft baking, mask alignment, UV-light exposure, photoresist development and hard-baking. It requires the fabrication to take place in a cleanroom with filters to remove ultraviolet light. Details of the fabrication and material properties can be found in many sources[123-125,127,133].

The fabrication of a three dimensional microstructure consists of numerous different stages. These can be broadly summarised as:

- Substrate preparation: cleaning and metallisation
- Photolithography
- Bonding

5.2.1. The Cleanroom

A cleanroom is a special environment required for the fabrication of microscale devices where particle count, temperature, humidity, vibrations and lighting are all controlled. As the scale of a device is reduced to the micron level, every trace of dust or contamination during the microfabrication can cause irreversible damage to the device.

The cleanroom class is defined as the maximum number of particles of 0.5 μm or larger per cubic foot of air. The Durham MEMS cleanroom is class 1000, except for the photolithography area which is class 100.

The human body represents a significant source of contamination. Cleanroom clothing (Fig. 74) is worn to protect the devices from textile and body dust. In higher class cleanrooms, the use of a mask and glasses can also be required.

Fig. 74. Protective clothing in the cleanroom.

5.2.2. Substrate Preparation

The device features are microscale, and therefore it is of great importance to work on a clean substrate, i.e. one that is contamination and dust free. The substrates considered in this project are silicon and glass wafers. Various cleaning methods exist for microfabrication. Mechanical cleaning such as ultrasonic agitation, manual polishing and supercritical cleaning are efficient ways to remove particles but they are less effective at

removing surface residue. Other treatments such as vapour cleaning, thermal treatments and plasma etching are also commonly used. Chemical cleaning can be used to remove organic contaminants or metal ions. Common methods use mixtures of hydrogen peroxide and various acids or bases in which the substrates are immersed.

5.2.3. Metallisation

When the process involves patterning metal, the fabrication starts with the metallisation of the substrate. The deposition process influences the film microstructure, and therefore its properties (e.g. surface roughness, coating density). For the study of electrical phenomena at the surface of the electrode those parameters must be well defined and the material structure homogeneous. The three most common techniques used to cover a substrate with a thin metallic film are evaporation, sputtering and electroplating.

Evaporation

- Filament Evaporation

Filament evaporation, also known as resistive evaporation, is the simplest method. This process is usually carried out in a vacuum bell jar, in which a current is used to heat a filament. As the temperature rises, the metal to be deposited is melted and wets the filament. The current through the filament is increased until the metal vaporises. The metal vapour condenses on the cooler surface of the substrate to form the desired metal layer. The deposition rate depends on the metal density and the amount of current passing through the filament. This technique is not applicable to metals that form eutectic mixtures with the tungsten (e.g. nickel).

- Electron-Beam Evaporation

Frequently called "e-beam", the electron-beam metallisation uses a focused beam of electrons, in a high vacuum chamber, to heat the metal for deposition. The metal source is kept in a water-cooled crucible and exposed to a beam of high energy electrons. As these come to rest in the metal, the heat released warms up the metal to create first a liquid and then a vapour. At this latter point the metal can evaporate and condense on the substrate. Deposition uniformity is governed by a cosine distribution law; however, in our case the

distance between source and substrate is large enough to make this angular variation insignificant and to consider the deposition non-conformal. For a given vacuum chamber, the deposition rate is determined by the thermal conductivity, specific heat capacity and melting point of the metal, and the current density of the electron beam[134].

Sputtering

To perform sputtering, ions of an inert carrier gas (such as argon) are introduced into a low-pressure or partial-vacuum atmosphere. An electric field is used to ionise the atoms and attract them to one place in the chamber known as the target. The target is the metal used for deposition. When the ions strike the target, they dislodge, or sputter, these metal atoms. The dislodged atoms are then deposited in a thin film on the substrate which faces the target. Sputtering can be achieved by using both direct current and radio frequency electrical supplies and can be used to deposit almost any material.

Electroplating

Electrochemical deposition is used for metals such as copper, gold and nickel. The deposition is achieved by applying an external electric potential between the wafer and a counter electrode while they are immersed in an electrolyte solution. For the deposition to happen, the substrate must already be covered by an electrically conducting layer (typically by evaporation or sputtering). When the electrical potential is applied between the conducting area of the substrate and the counter electrode a chemical redox reaction takes place in the electrolyte solution. Metal ions are reduced to their solid state at the surface of the wafer to form a layer of material. The deposition is isotropic and the rate is determined by the metal concentration in solution and the current density applied to the electrodes[135]. Film thicknesses obtained with this method vary from sub-micron to hundreds of microns.

5.2.4. Photolithography

Photolithography is the process of patterning a radiation-sensitive polymer (photoresist)[127]. The photoresist is commonly applied on the substrate by spin coating and its wet thickness depends on its viscosity and the speed and time of the spin. The polymer is then prebaked to drive off the excess solvent. It is exposed to UV-light through the mask designed with the desired pattern. This exposure changes the photoresist's chemical resistance to the developer solution. Finally the photoresist is developed in wet chemicals in order to remove the soluble parts and form the desired pattern. Once the photoresist processing is finished, its pattern can be transferred into underlying layers using etching techniques.

The photoresist can have either a positive or negative polarity. For positive resists, the resist is exposed with UV light wherever the material is to be removed. The final pattern of the photoresist is the same as the one of the mask. The UV light changes the chemical structure of the resist so that the exposed parts become soluble in the developer. The exposed resist is then washed away by the developer solution.
Negative resists behave in the opposite manner. After prebaking, the UV exposure activates the polymerisation initiator. The polymerisation settles during postbaking and makes the exposed photoresist not soluble in developer. Therefore, the polymerised photoresist remains on the surface whereas the unexposed areas are removed in the developer solution. When using a negative photoresist, the final pattern of the material is the inverse of the mask's pattern.

The different steps of the process are schematically represented in Fig. 75.

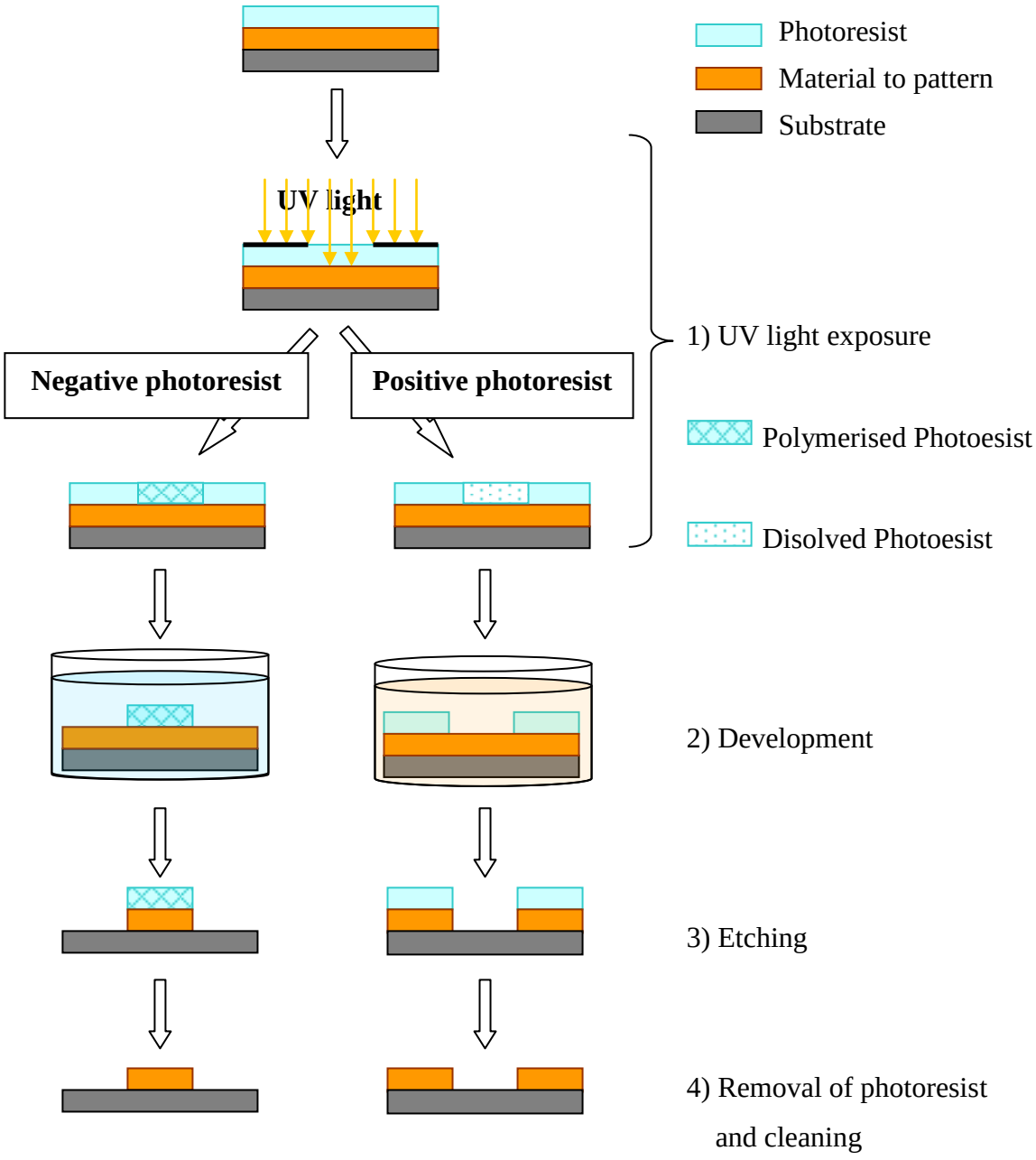

Fig. 75. The photolithography process.

A good quality pattern requires careful control of the UV exposure and development conditions. If there is insufficient light energy reaching the photoresist, the chemical reaction is incomplete, and the photoresist is not completely soluble or fully polymerised. In this case, called underexposure, the pattern is only partially developed and the corners and edges, which receive slightly less light than the centre of the pattern, are poorly defined at the end of the process.
On the opposite, there is overexposure when too much light energy reaches the photoresist and the chemical reaction spreads outside of the bounds of the exposed area. This is partially due to chemical transport within the photoresist, but is mostly caused by stray light reaching the masked areas. Again, this effect brings poor definition of the pattern formed in subsequent processing.
The effects of the developing solution are comparable to the exposure. Underdeveloping can lead to residual photoresist in an exposed area, either in the corners or throughout the exposed area.

To have a well defined pattern and an accurate thickness, the parameters such as the baking time or the intensity and length of UV exposure, must be coherent with the thickness of the wet photoresist which is processed. Optimum parameters are determined empirically or using guidance provided with the photoresist[128,136].

5.2.5. Materials

When compared to silicon and glass, polymers can be cheap and relatively easy to process for micromachining. They are easily deposited on substrates by spin coating with thicknesses varying from millimetres to micrometres. The microfluidic channels were embedded in PDMS and the electrodes were shaped in SU8.

PolyDiMethylSiloxane (PDMS)

PDMS is an organosilicon polymer with a $SiO(Me)_2$ repeat unit as shown in the Fig. 76.

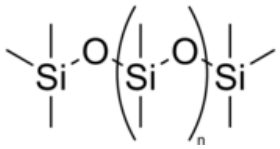

Fig. 76. PDMS structure, where n is the number of monomer of the polymer

The PDMS is manufactured in a range of viscosities, from a thin pourable liquid (when *n* is very low) to a thick, rubbery, semi-solid (when *n* is very high). This can be controlled by adding a silane (SiH_4) precursor during the polymerisation. A Si substituted precursor limits branching and cross-linking whereas using a non-substituted Si precursor increase the possibility of branching on the silicon. After polymerisation and cross-linking, solid PDMS is hydrophobic. Its surface is barely wet by polar solvents but can possibly adsorb hydrophobic contaminants. As aqueous solvents do not penetrate or swell solid PDMS, this material can be used with water and alcohol solvents without material deformation. However some organic solvents such as chloroform, ether, and THF diffuse into the material and cause it to swell.

Plasma oxidation can be used to alter the PDMS chemistry and form silanol (SiOH) at its surface. This treatment makes the PDMS surface temporarily hydrophilic, allowing the surface to be wetted and functionalised.

PDMS is optically clear, flexible and resistant. It is considered to be inert, non-toxic and non-flammable. Its good mechanical properties combine with ease of manufacture to make it suitable for a very wide range of applications and it is very commonly used in microfluidic systems [137-139].

SU8 [123-125,133]

SU8 photoresist was first developed in 1989 by IBM to fabricate printed circuit boards and for packaging. It was adapted in 1996 for microsystem fabrication and is now used for a variety of micromachining based applications.

SU8 material consists of an epoxy resin (EPON®) dissolved in an organic solvent, along with an onium salt which acts as a photoacid generator. Its molecular structure is presented in Fig. 77.

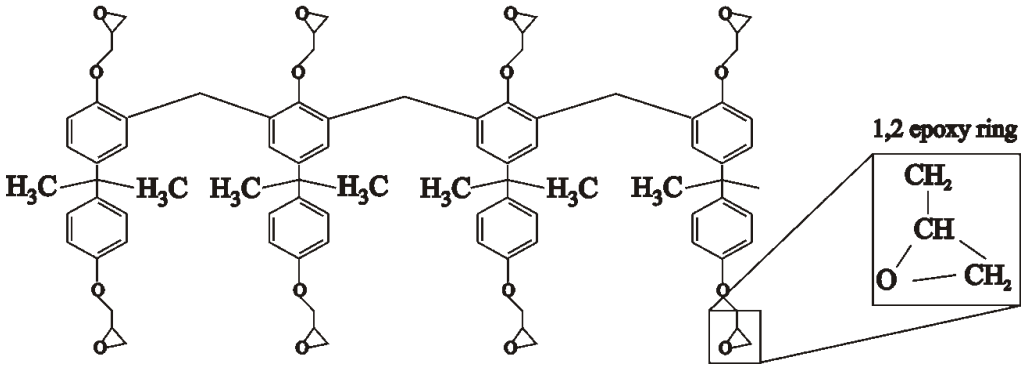

Fig. 77. The molecular structure of SU-8 epoxy (glycidyl-ether-bisphenol-A novolac).

Each molecule is composed of 4 glycidyl-ether-bisphenol groups, and therefore 8 epoxy reactive groups (hence the "8" in SU8) which provide a very dense three dimensional crosslinked network when the resin is cured. This arrangement makes the SU8 polymer very robust and resistant to temperature variation. On the other hand, since the polymer has a low molecular weight (~7000), when uncrosslinked, it can be easily dissolved by a number of solvents (e.g. propylene-glycol-methyl ether (PGME), gamma-butyrol-acetone (GBL), and methyl iso-butyl ketone).

The SU8 is commonly used in photolithography as a negative photoresist to process and pattern thin layers. When exposed to the UV light, the onium salt is converted into an acid. During the postbake, the acid molecules initiate the polymerisation by reacting with the epoxy groups and producing radicals which attach to the backbone of SU8 molecule. When the cross-linking happens between two such radicals, the acid molecule regenerates and can induce further polymerisation. The postbaking step is necessary since the glass temperature of the uncured SU8 is 50 ºC and therefore at room temperature the reaction would barely take place.

SU8 has good physical and chemical properties which make it robust, stable and very resistant to most organic solvents and acids. It is compatible with the standard silicon processing and with most of the chemicals used in analytical applications. It also has very good optical properties with a transparency of greater than 98% from 500 to 850 nm. The main disadvantages are its adhesion, selective removal, mechanical stress and a large thermal coefficient of expansion. For these reasons, although SU8 is mainly used as a photoresist to make a mould, it can also be used as a structural material.

In this project, the SU8 is used as a mould for the microchannel fabrication, and as an electrical insulator to shape the microelectrode. The formulation used was based on GBL as the solvent, whereas newer versions of SU8 use cyclopentanone.

5.2.6. Etching

Etching consists of removing material away from the defined patterns. Etching techniques can be separated in two groups, i.e. wet or dry techniques. Wet techniques require immersion of the substrate in a solution containing chemicals which react with the material where it's not protected. Dry techniques usually consist of plasma processes where the material is bombarded with reactive ions etching the surface. The main advantages of the wet techniques are the low cost and high etching rate, although using liquid chemicals might be a source of contamination and handling hazards. Dry etching techniques can produce a very directional etch and therefore allow extremely small feature sizes (< 100 nm) to be defined.

5.2.7. Plasma Surface Treatment

Surface treatment commonly refers to: surface cleaning, surface crosslinking, surface functionalisation, surface etching and coating deposition. Plasma surface treatment[140] offers the flexibility to choose either highly anisotropic or isotropic process, enabling a very clean and accurate treatment of the layers.

A plasma is a partially ionised gas mixture consisting of ions, free radicals, neutral by-products, and photons. During the process, gases flow through the chamber, with the flow rate controlled by mass flow controllers (MFCs) and chamber pressure is maintained by an automatic throttle valve connected to a vacuum pump.

Two mainstream technologies are available: Reactive Ion Etching (RIE), and Plasma Etching (PE). In RIE mode, power is applied to the lower electrode to strike and maintain the plasma and to provide ion bombardment of the wafer through the generation of a DC bias. The whole chamber provides the ground electrode. In this process the size difference between the electrodes leads to a net electric field. When using PE mode, the power is supplied to the upper electrode while the lower is grounded. The equally sized electrodes lead to no net effect. Further, the use of a much lower chamber pressure (1-10 mT in RIE, 50-1000 mT in PE) gives directionality to the etching ions in RIE. The orientated ion bombardment in RIE permits to avoid undercutting and the PE mode produces a smoother and more uniform finish.
Fig. 78 shows the differences between the chambers for RIE and PE process and the resulting etching.

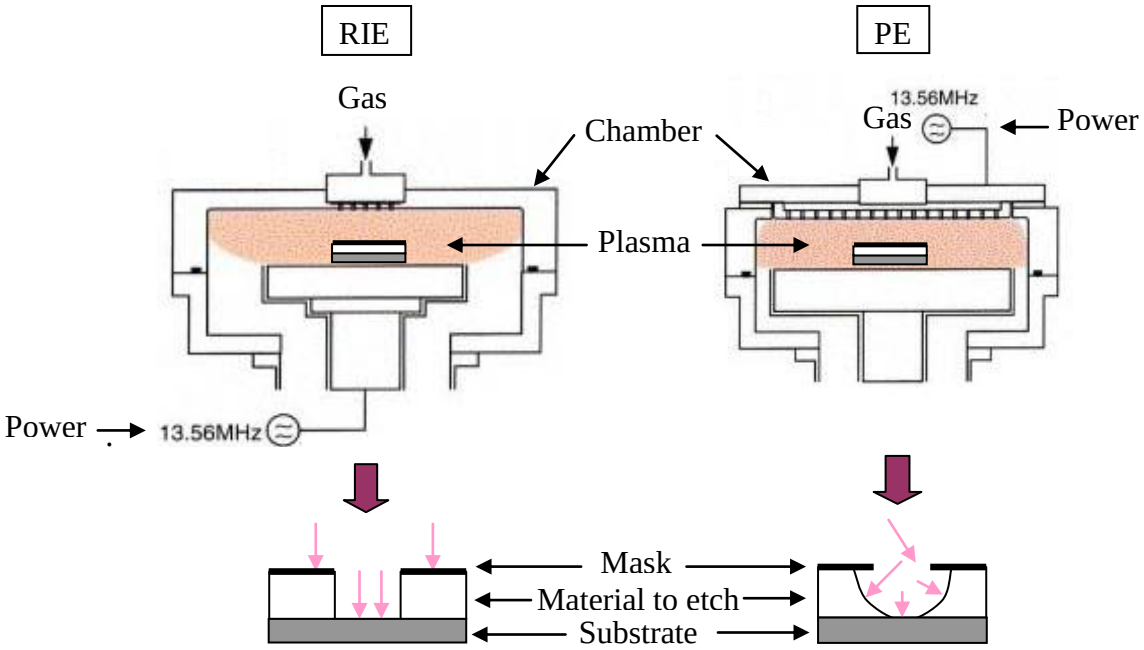

Fig. 78. RIE compare to PE.

5.3. MICRODEVICE FABRICATION

Both the microfluidic channel pad and the electronic circuit were fabricated using photolithography. The devices were fabricated in a cleanroom under yellow light. The microfluidic channels were made of PolyDiMethylSiloxane (PDMS). The electronic circuit supporting the electrode array and the pads consisted of gold on top of a chromium layer necessary for adhesion between the substrate (glass or silicon) and the gold. The photoresist SU8 was used as an insulator to shape the microdisc electrodes. Finally, the two pieces were bonded together using oxygen plasma activation of their surfaces.

5.3.1. Substrate Preparation

The substrates were glass slides (PGO Optics) and silicon wafers, 2 in. diameter, (100) orientation, 275 +/- 25 µm thick, n-phosphorus doped, 10-30 Ωcm, single sided polished from Siltronix. Both substrates were cleaned by immersion in an acidic solution made from sulphuric acid (Fisher) and hydrogen peroxide (Fisher), 3:2 H_2SO_4:H_2O_2 v/v, for 20 minutes. When the substrate was a semiconducting silicon wafer, an additional step was necessary to insulate the surface. The wafer surface was etched in a 10% HF solution, to remove any native oxide, and then rinsed in DI water and dried with nitrogen. The substrate was then placed in a high temperature furnace, with an oxygen atmosphere, for 1.5 hours, which was sufficient to grow an insulating oxide layer of 200 nm thickness.

5.3.2. Electrode Fabrication

The gold layer consisted of 3 sets of electrodes and pads: the pseudo reference electrode, the counter electrode and the working electrode (MEA). The fabrication and shaping of the electrodes started with the metallisation of the substrate, followed by photolithography and etching of the undesired metal.

Metallisation

The two metallisation processes compared in this project were e-beam evaporation and electroplating.

For e-beam metallisation, the clean insulated substrate was coated with chromium (10 nm), and then gold (200 nm), using an e-beam evaporator (Lesker six source). Patterning was achieved by selective etching using a photoresist mask. The positive photoresist S1813 (Rohm and Haas) was applied on the wafer by spin coating (Laurell Technologies, 1st step: 10 s, Acc.: 500 rpm^{-2}, Initial speed: 0 rpm, Final speed: 700 rpm; 2nd step: 30 s, Acc.: 3000 rpm^{-2}, Initial speed: 700 rpm, Final speed: 3700 rpm). It was prebaked at 95 °C for 8 min before being exposed to UV light (EVG620 double sided mask aligner) through the mask shaping the gold layer (Fig. 79). The exposed photoresist was removed in a mixture of Microdeposit 351 developer (Rohm and Haas) and water (1:2 351:H_2O). The bare gold and chromium were removed by immersion in gold etching solution (3:1:6 KI:I_2:H_2O w/w) and chromium etching solution (10:1:49 $(NH_4)_2Ce(NO_3)_6$:NO_3:H_2O w/w). The residual photoresist was removed using the microposit remover 1112A from Rohm and Haas.

For electroplating metallisation, the clean substrate was coated with chromium (10 nm), and then gold (50 nm), using the same e-beam evaporator. Positive S1813 photoresist was spin coated on the substrate. It was prebaked at 95 °C for 8 min before being exposed to the UV light through the mask shaping the *inverse* of the electronic circuit. The exposed photoresist was removed by immersion in a mixture of microdeposit 351 developer and water (1:2 351:H_2O). The gold electroplating solution (Neutronex 309) was stirred and maintained at 40 ºC, and a 0.8 mA current was applied to the circuit for 1 hour. After deposition the photoresist was removed using the Microposit remover 1112A from Rohm

and Haas, and the surface was gently etched to remove the gold and chromium seed layers. Fig. 80 is a schematic picture of the cross section of the substrate after metallisation.

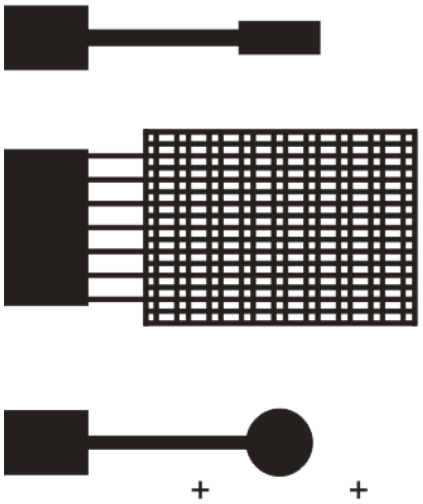

Fig. 79. Gold electrodes and pads mask.

Fig. 80. Cross section diagram of the substrate covered with Cr and Au.

SEM analysis showed that the thickness of the electroplated gold layer varied between 1 and 3 µm. This variation was no source of problem for the electrode characterisation as the roughness of the gold, measured by AFM, showed good consistency.

Electrodes Shaping

The microdisc electrodes were shaped by a 2 µm thick layer of SU8-2 photoresist[128] (Chestech), employed as an insulator. The negative photoresist was spin coated on top of the electronic circuit (1^{st} step: 5 s, Acc.: 100 rpm^{-2}, Initial speed: 0 rpm, Final speed: 500 rpm; 2^{nd} step: 30 s, Acc.: 300 rpm^{-2}, Initial speed: 500 rpm, Final speed: 2000 rpm). It was prebaked for 3 min at 65 °C and 1 min at 95 °C, exposed to the UV light through the mask (Fig. 81) and postbaked for 1 min at 65 °C and 1 min at 95 °C. The uncured photoresist was removed by immersion in EC solvent (Rohm and Haas). The insulating layer was then baked a final time at 120 °C for 10 min to stabilise.

The surface of the electronic device was cleaned from residual material by oxygen plasma etching (Oxford Plasma Technology RIE80, exposed to 50% of O_2 for 2 min at a forward power of 80 W, a pressure of 100 mTorr and a temperature of 20 ºC).

Fig. 82 is a schematic picture of the cross section of the substrate after metallisation and electrode shaping.

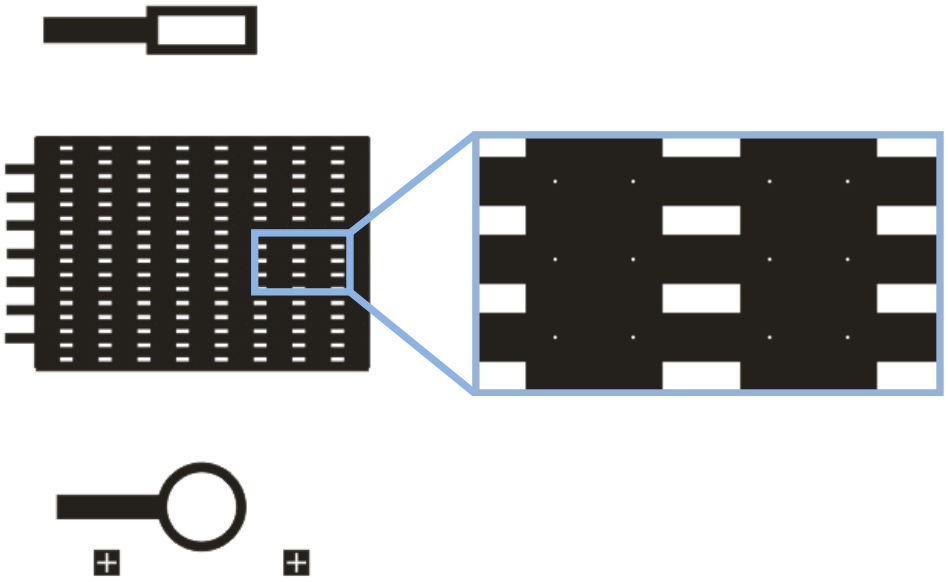

Fig. 81. SU8-2 insulator mask.

Fig. 82. Cross section diagram of the substrate covered with Cr and Au.

Microfluidic Channels Fabrication

The microfluidic channels were built in PDMS. A SU8-50 photoresist[136] (Chestech) mould was prepared on a silicon substrate. The SU8-50 photoresist was spin coated on a silicon wafer (1^{st} step: 5 s, Acc.: 100 rpm^{-2}, Initial speed: 0 rpm, Final speed: 500 rpm; 2^{nd} step: 30 s, Acc.: 300 rpm^{-2}, Initial speed: 500 rpm, Final speed: 1000 rpm), prebaked for 10 min at 65 °C and 30 min at 95 °C, exposed to the UV light through the mask (Fig. 83), and postbaked for 10 min at 65 °C and 3 min at 95 °C. The uncured photoresist was removed by immersion in EC solvent. Pieces of tubing were glued at the surface of the mould to structure the entrance and exit ports of the channels. The mould was sputter coated (Agar SEM coater) with a thin layer of gold to prevent adhesion with the PDMS.

The liquid PDMS was poured onto the substrate, placed under vacuum to remove the bubbles, and cured for 20 min at 120 ºC. Once cured and cooled down, the PDMS was carefully peeled away from the substrate. Fig. 84 to Fig. 86 are schematic pictures of the cross section of the PDMS mould and PDMS slab once peeled away.

Fig. 83. SU8-50 microfluidic channels mask.

Fig. 84. Cross section diagram of the SU8 mould.

Fig. 85. Cross section diagram of the SU8 mould covered with liquid PDMS.

Fig. 86. Cross section diagram of the PDMS slab once cured.

Substrate and Microchannels Bonding

Adhesion between the channels and the microelectrode support was promoted using plasma surface activation[140] (Oxford Plasma Technology RIE80). The two surfaces to activate were exposed to 60% of O_2 for 40 s at a forward power of 125 W, a pressure of 300 mTorr and a temperature of 20 ºC. After exposure the two pieces were mechanically clamped for two days to ensure good adhesion.

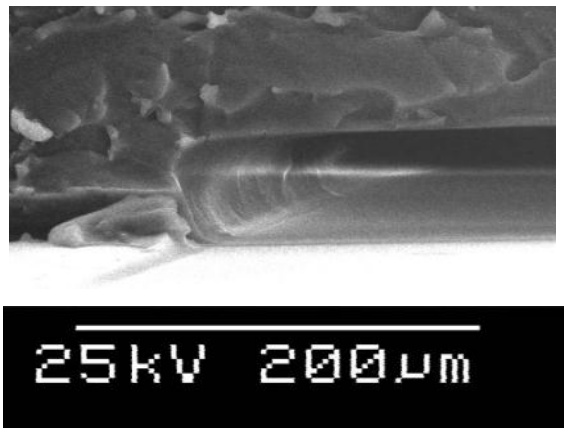

Fig. 87. SEM picture of the cross section of the PDMS channel bonded with glass.

Mask Fabrication

The patterns were drawn using CorelDRAW 11 and printed on to a transparent film. The design was transferred onto an emulsion plate by photoreduction (Sinar plate camera). As the contrast on the emulsion masks was not high enough to reproduce very fine features (few µm), the pattern was transferred again to a chromium mask. The mask was patterned using the S1813 based photolithographic process described earlier for the electronic circuit fabrication.

5.3.3. Microelectrode Characterisation by CV

CVs measurements were carried out using a multichannel potentiostat from Perkin Elmer Instruments. The software used to record the data was EClab V9.42. The analytes probed for the microelectrodes' characterisation were 1 mmol/L $Ru(NH_3)_6Cl_3$ (Aldrich, D= $7.1x10^{-6}$ $cm^2.s^{-1}$) dissolved in deionised water containing 0.1 mol/L KNO_3 (Lancaster) as background electrolyte; and 3 mmol/L 2,2,6,6-Tetramethylpiperidine-1-oxyl **(**TEMPO, Aldrich), dissolved in acetonitrile (HPLC gradient grade) containing 0.1 mol/L $NaClO_4$ (Aldrich) as background electrolyte.

5.3.4. Flow Injection Analyses by Chronoamperometry

In the case of FIA measurements, the analyte was injected into the microfluidic channel using a syringe micro pump. To create a gradient of concentration, a closed reservoir containing solvent and background electrolyte was inserted between the syringe and the device via tubing. As the analyte was pumped in the circuit, its concentration in the reservoir increased, until reaching its source value, when the reservoir content has been fully replaced with the syringe solution. The analyte probed was 2,2,6,6-Tetramethylpiperidine-1-oxyl **(**TEMPO, Aldrich), dissolved in acetonitrile (HPLC gradient grade) containing 0.1 mol/L $NaClO_4$ (Aldrich) as background electrolyte. Chronoamperometric measurements were carried out using a multichannel potentiostat from Perkin Elmer Instruments. The software used to record the data was again EClab V9.42.

5.3.5. Surface Analysis

The physical appearance of the electrodes was confirmed using a Scanning Electron Microscope (SEM) (Hitachi, S-2400), and surface roughness analyses were completed using an Atomic Force Microscope (AFM) (Veeco Digital Instruments, Dimension 3100).

5.4. FABRICATION DISCUSSION

The first microelectrode array fabricated is shown in Fig. 88 where, from left to right are the counter, the MEA and the reference electrode. The array was made of 5 microelectrodes with a diameter of 100 μm. The SU8 insulator being transparent, the position of the microelectrodes is indicated by the black dashed circles. This system was improved by reducing the diameter of the microelectrodes and increasing their number.

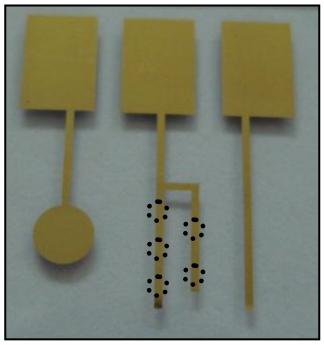

Fig. 88. First microelectrode array.

The final array consisted of 306 gold microelectrodes, each with a diameter of 45 μm. The MEA, the counter and the pseudo reference electrodes were built in the same gold circuit. Fig. 89 shows the whole device, composed of the electronic circuit on glass surmounted with the PDMS microchannels. The electronic circuit consists of 3 sets of electrodes; on the left of Fig. 89 is the counter electrode, in the centre is the microelectrode array and at the right is the pseudo-reference electrode. SEM images were taken to validate the electrode dimensions. Fig. 90 is an SEM picture showing part of the MEA, where the white dots are the exposed electrodes and the light grey is the gold circuit covered with the SU8 insulator. The SEM picture of a single electrode confirmed that the microdiscs had a diameter of 45 μm.

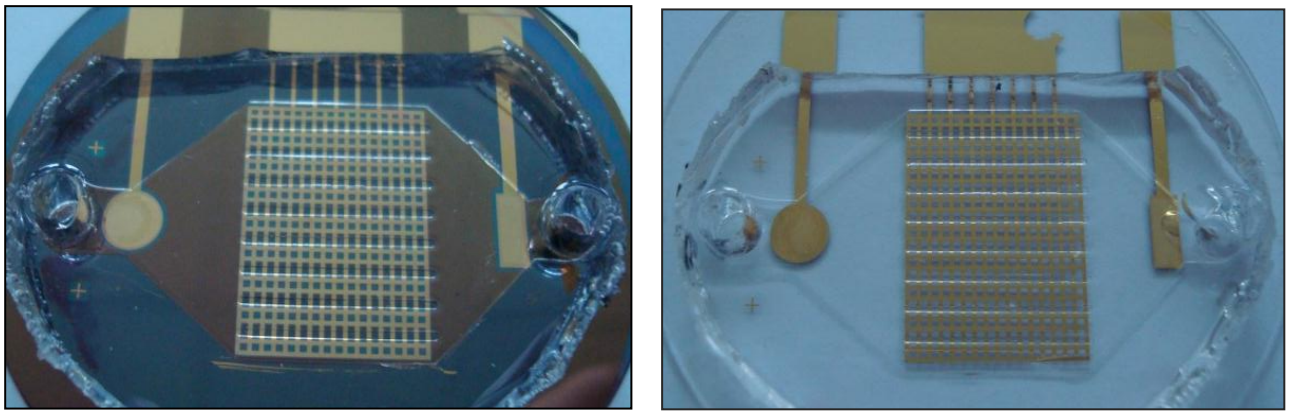

Fig. 89. Complete microfluidic device. Left: silicon substrate; right: glass substrate.

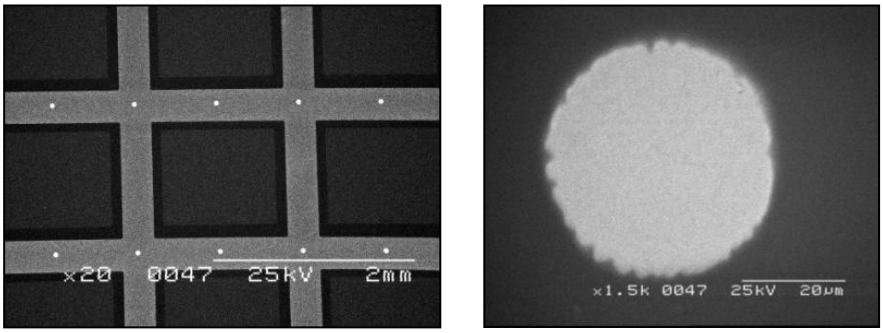

Fig. 90. (left). Microelectrode array. (right). Individual microelectrode.

5.4.1. Substrate

Although silicon wafers are the most extensively used substrate in the fabrication of thin film devices, glass is more robust, cheaper and easier to process. Glass transparency also allows a visual check of the chromium layer stability against chemical attack at any time. The surface roughness and the resistivity of glass and silicon substrates were compared to verify that any could be used without consequences on the performances of the electronic circuit.

The AFM measurements showed that the glass surface roughness was comparable with that of silicon (roughness average Ra = 0.178 nm and 0.107 nm for glass and silicon respectively). Furthermore, in contrast to silicon, glass is not a conductive material and so there is no need for an additional step to insulate the surface. AFM pictures showed no differences between metal layers when evaporated at the surface of silicon or at the

surface of glass: average roughness values were Ra = 0.844 nm for silicon (Fig. 91) and = 0.868 nm for glass (Fig. 92). The gold surface area measured for a nominal 5 µm square was 25.1 μm^2 for both glass and silicon. Those results confirmed that in these conditions the crystallinity of the substrate had no influence on the way the metal organised itself at the surface of the wafer during the e-beam deposition.

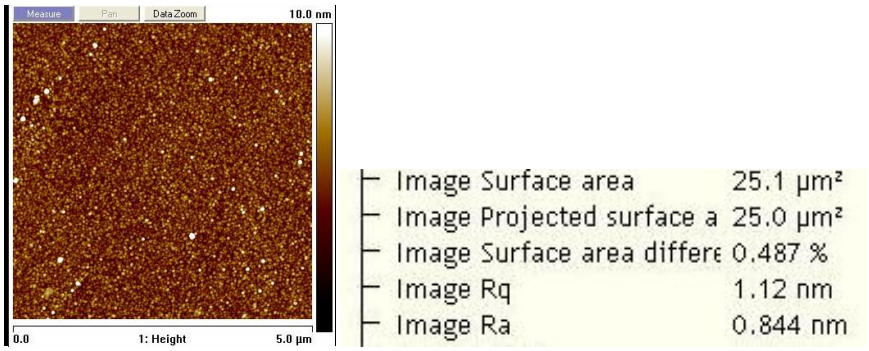

Fig. 91. AFM. Cr and Au on silicon.

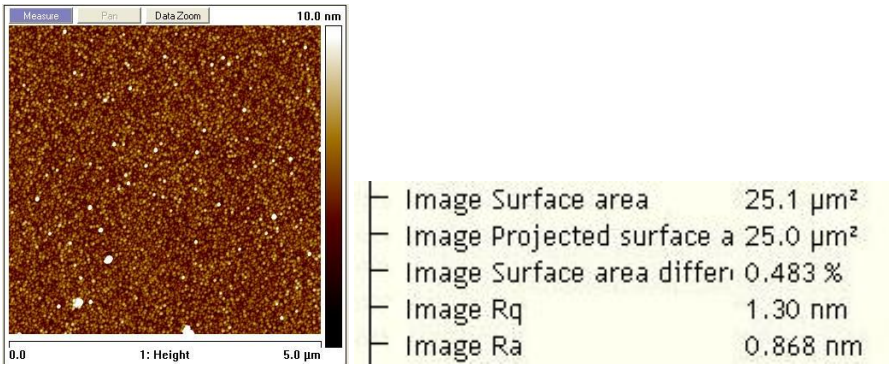

Fig. 92. AFM. Cr and Au on glass.

The three electrodes (working, counter and pseudo-reference) were built on the same substrate, and therefore the efficiency of the MEA also depended on the resistivity of the support. The current leakage was measured between the electrodes for the silicon wafer and for the glass substrate to ensure that no difference of resistance would influence the final device response during electroanalysis. The leakage between the electrodes was similar for the silicon wafer and for the glass substrate, in the range of 10 pA, which could be neglected in comparison with the microamps range expected to be measured by the device.

Glass substrates were preferred to silicon wafers as they could be used more easily, they were more robust and they had a similarly low value of surface roughness.

5.4.2. Design

The electrodes were designed in order to retain a distance between the electrodes large enough to avoid any overlapping of diffusion layers. The electrode radius was 22.5 µm and the centre-to-centre distance between them was 800 µm, for a D/r = 35.
The microfluidic channels consisted of 9 microfluidic channels in parallel. The depth of the channels was 200 µm, as measured from the SEM picture of the SU8 mould (Fig. 93). It was chosen to be big enough so the diffusion layer of the microelectrodes, which grew during electroanalytical measurements, wasn't obstructed by the PDMS walls. To ensure the microfluidic channels were not interfering with the measurements, the CV analysis of the array directly immersed in the analyte solution and supported by the microchannels were compared. The responses were the same whether or not the circuit was embedded in the PDMS slab, proving that the 200 µm distance between the electrodes and the channel wall was enough to maintain their good behaviour.

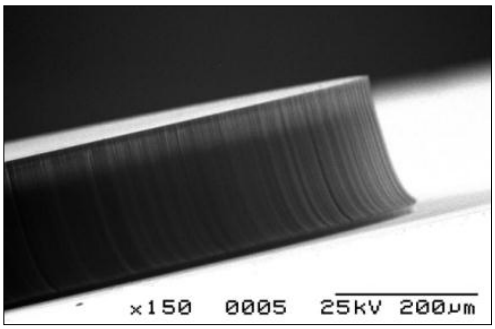

Fig. 93. SEM picture SU8 mould.

The microfluidic slab consisted of 9 channels in parallel (Fig. 83) in order to maintain the uniformity of the depth (200 µm) between the wall and the centre of the channel. Due to the shrinkage of the PDMS substrate during baking, the microchannel features were corrected and designed 10% bigger to get a size compatible with the electronic circuit.

Gold Stability

The microelectrodes were characterised using CV analysis. Although the microelectrode response was stable for low potential and current, the metal dissolved instantaneously when higher currents (up to 0.1 mA) were measured, and a higher potential (up to 2.5 V) was applied. The deterioration of the underneath chromium layer could be observed through the glass substrate (Fig. 94).

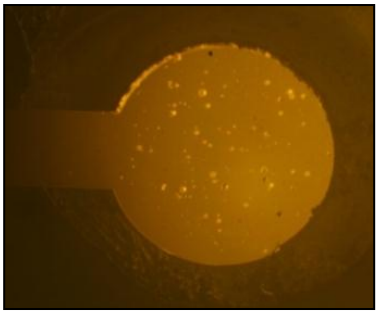

Fig. 94. Underneath view of the electrode deterioration.

The lack of chromium lead to the entire deterioration of the electrode, as gold had no adhesion with glass. The spherical shape of the damaged areas and the uniformity of their distribution in the chromium layer corroborate the presence of pinholes in the gold layer, allowing undesirable contact between the chemicals in solution and the chromium and dissolution of the metal. In comparison with those results, the electronic circuit fabricated by electroplating barely deteriorated after continual use. This was due to the manner the gold was deposited at the electrode surface. The processes of e-beam and electroplating deposition are schemed in Fig. 95. In electroplating metallisation, the deposition was isotropic and the layer obtained was thicker which prevented pinhole formation. On the contrary, the e-beam evaporation resulted in thin gold layer, more exposed to pinhole formation.

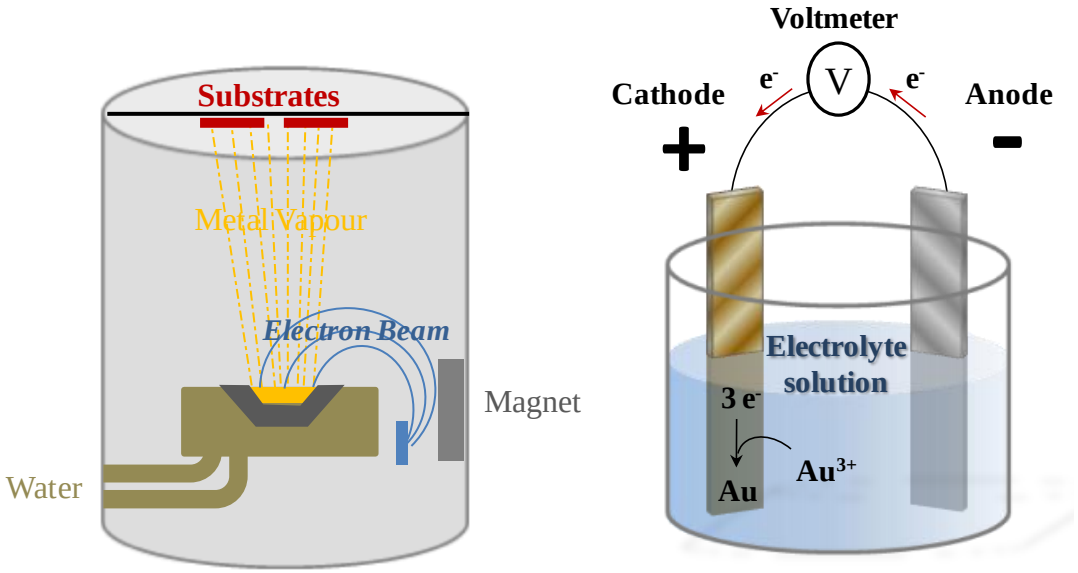

E-beam deposition Electroplating deposition

Fig. 95. E-beam vs electroplating metallisation.

No improvement was achieved by changing the circuit composition. The same degradation happened when the adhesion layer was titanium rather than chromium and the pinholes were still present when platinum was used instead of gold. Increasing the thickness of the gold layer during e-beam evaporation (from 1000 Å to 2000 Å) helped improve its uniformity and limited the number of pinholes but this metallisation technique had to be used for low current detection exclusively. Subsequent experiments were run using a restricted potential window between -0.4 V and 1 V to ensure the stability of the electrode.

5.5. MICROELECTRODE ARRAY PERFORMANCE

5.5.1. Electrode Stability

The electrochemical cell for cyclic voltammetry and chronoamperometry is composed of 3 electrodes; the working electrode, the counter electrode and the reference or pseudo reference electrode.

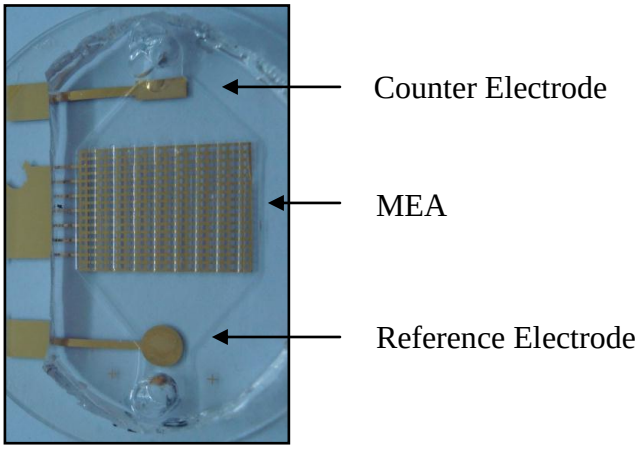

Fig. 96. Microdevice.

To simplify the fabrication of the microdevice, the three electrodes were built in the same gold material (Fig. 96). Platinum is usually more commonly chosen for reference and counter electrodes because of its great chemical stability and robustness.

The stability of the gold system was validated by CV analyses comparing the response of the microelectrode array when using gold pseudo reference electrode and gold counter electrode and when using platinum pseudo reference electrode and platinum counter electrode (Fig. 97).

.

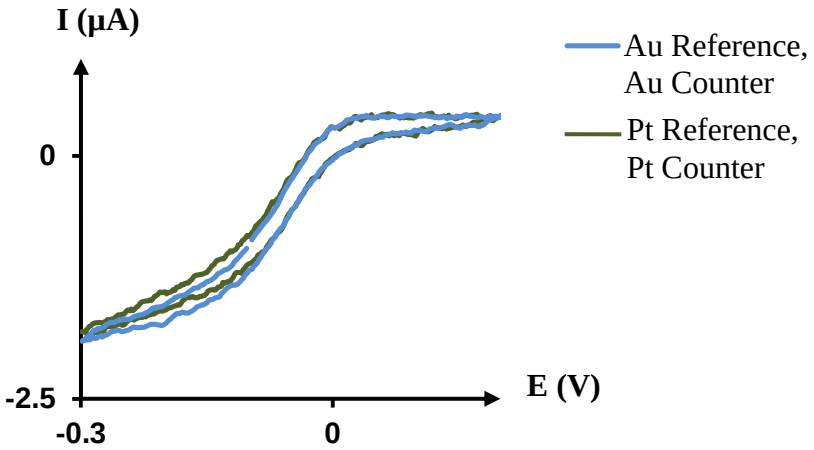

Fig. 97. MEA response in the presence of $K_3Fe(CN)_6$, against Au pseudo reference using a Au counter electrode and against Pt pseudo reference using a Pt counter electrode.

The voltammogram shows that the amplitude of the current obtained was the same whether gold or platinum was used. These results confirmed the reliability of using gold as both a pseudo reference and as a counter electrode.

5.5.2. Microelectrode Array Behaviour

In CV analyses, the well-known behaviour of the microelectrode array depends on the occurrence of an individual spherical diffusion layer at the surface of each electrode.
In the absence of overlapping between the electrodes' diffusion layers, the CV voltammogram consists of a steady state current shape where the amplitude does not depend on the scan rate. (Eq. 10) where I_{ss} = n4zFDCa).

The calculation of the minimum distance necessary between microdisc electrodes to avoid overlapping of their diffusion layers has evolved in the past few years to take into account not only the radius of the electrode but also parameters such as the scan rate, the recess depth or the analyte diffusion coefficient[15,28,29]. The MEAs were designed in order to have a centre-to-centre distance of d = 800 µm and an electrode radius of a = 22.5 µm. These parameters ensure the required criteria (Eq. 32 and Eq. 33) to preserve the independent diffusion layer at each electrode are met[28].

Eq. 32 $d > 20a$

Eq. 33 $d > 2[2D(\Delta E/\nu)]$

where D is the analyte's diffusion coefficient (cm^2/s), ΔE is the potential difference between the onset of electrolysis and a potential where the limiting current (or peak potential) is obtained (V), and υ is the scan rate (V/s).

Overlapping between the electrode's diffusion layers is visible in CV analyses as it results into a voltammogram having a Nernstian shape, comparable with the macroelectrode response. Fig. 98 shows the responses of the MEA in the presence of $Ru(NH_3)_6Cl_3$ for different scan rates.

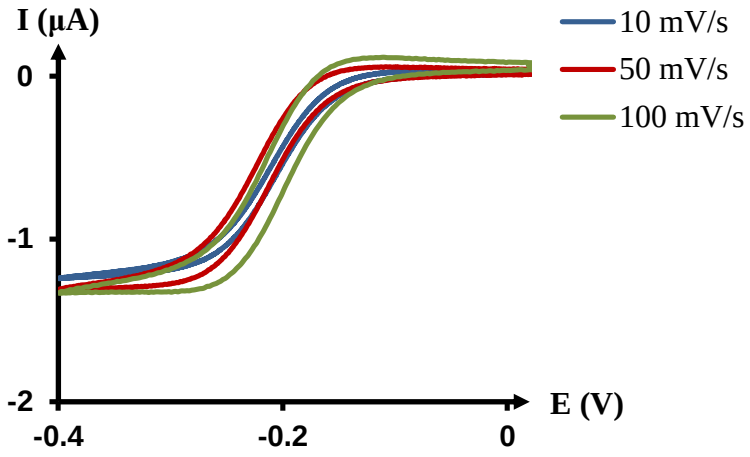

Fig. 98. CV of MEA in $Ru(NH_3)_6Cl_3$ (1 mmol/L) in KNO_3 (0.1 mol/L) for different scan rates.

CV analyses showed a constant steady state current independent of the scan rate, indicating the well behaved nature of the individual microelectrodes and also their collective behaviour.

The behaviour of the device was also tested on analytes in organic solution. The redox active species was the 2,2,6,6-Tetramethylpiperidine-1-oxyl (TEMPO) in acetonitrile containing $NaClO_4$. CV measurements for different scan rates showed constant steady state current, illustrating the efficiency of the device for solvents other than water.

5.6. ELECTRODE SURFACE CHARACTERISATION

The electrochemical performances of a microelectrode are directly related to its surface area. The active surface of the microelectrode array was characterised by AFM and CV analysis in 1 mol.L^{-1} sulphuric acid and 1 mmol.L^{-1} $Ru(NH_3)_6Cl_3$. The AFM pictures showed that electroplated and e-beam electrodes had different values of surface roughness. Both e-beam and electroplated electrodes were processed exactly the same way, attesting that the roughness variation resulted only from the use of different metallisation techniques. Fig. 99 presents the AFM picture and the roughness values of the electrode surface for gold deposited via e-beam evaporation (left) and deposited via electroplating (right).

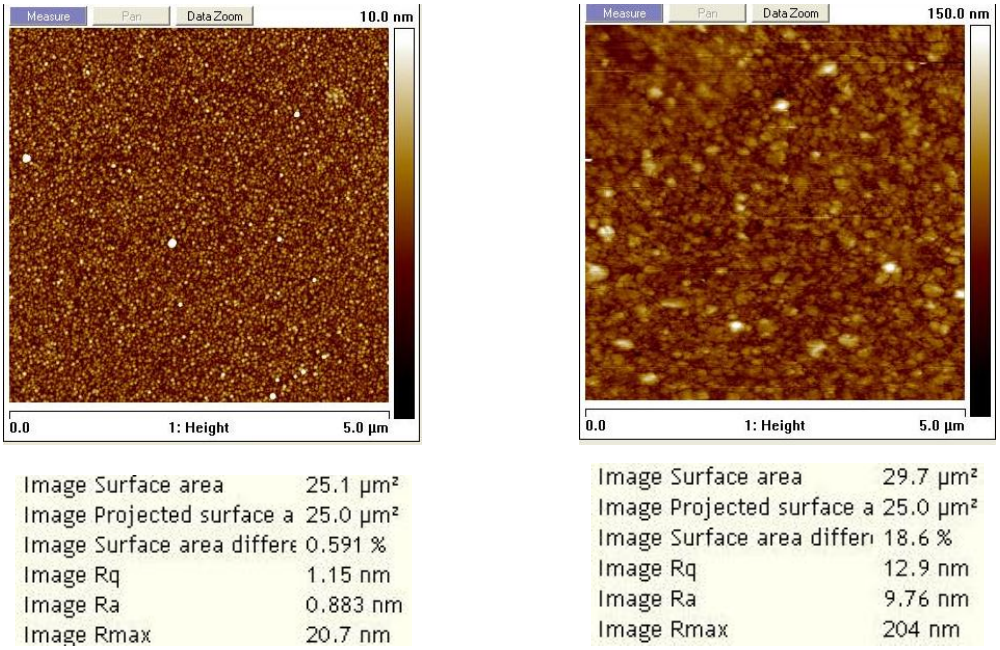

E-beam electrode **Electroplated electrode**

Fig. 99. AFM picture of gold surfaces metallised using e-beam and electroplating.

AFM images of the surfaces of the electrodes show that the average surface roughness Ra was 0.88 nm for the e-beam gold electrodes and increased more than ten-fold to 9.76 nm for the electroplated gold electrodes. This difference implied an increase of the effective surface area of 18.6 %. As the current response measured in CV analysis is proportional to the size of the electrode, the increase of the effective surface area was expected to increase the activity of the electrode.

CV analyses run in sulphuric acid confirmed the difference between the roughness factors of the e-beam and the electroplated electrode (Fig. 100). The roughness factor was calculated from the integration of the gold oxide reduction peak, using the Brummer and Makrides method[141]. It is assumed that the charge required for the reduction of the monolayer of chemisorbed oxygen on a polycrystalline gold electrode is 400 µC.cm^{-2}. The roughness factor was 480 µC.cm^{-2} for the e-beam electrodes, and 700 µC.cm^{-2} for the electroplated one.

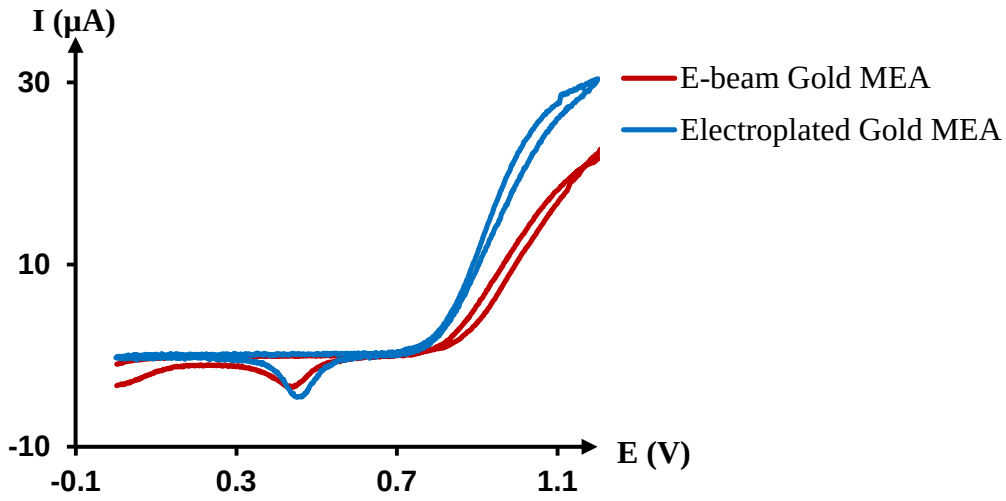

Fig. 100. CV of MEA in H_2SO_4 (1 mol.L^{-1}) comparing electroplated and e-beam gold array response vs gold pseudo reference electrode.

The electro-activity of the MEAs were compared using $Ru(NH_3)_6Cl_3$ analyte. Fig. 101 shows that the current measured with the e-beam gold electrodes was 1.2 µA, whereas it increased to 1.6 µA for the electroplated gold electrodes.

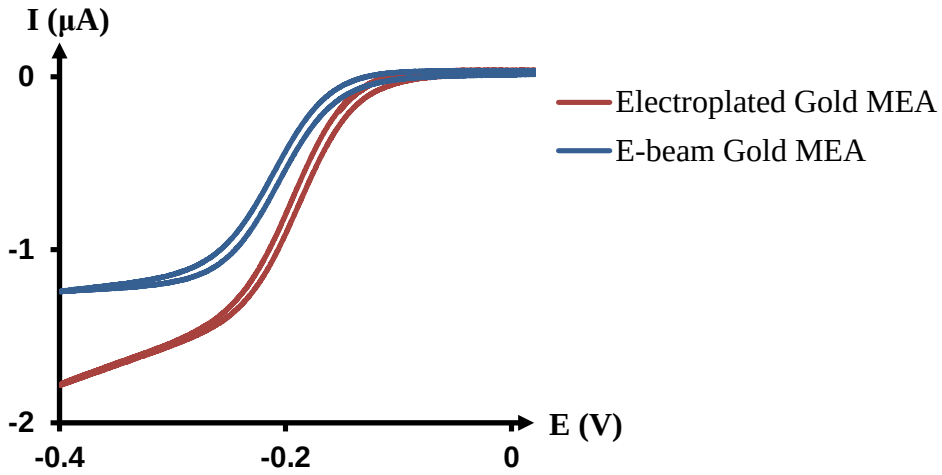

Fig. 101. CV for MEA in the presence of $Ru(NH_3)_6Cl_3$ (1 mmol/L) in KNO_3 (0.1 mol/L).

These responses were compared to the theoretical values describing the current at recessed microelectrodes, where $I_{ss} = n4zFDCae^{(-0.96L/a)}$ (Eq. 11) with an analyte diffusion coefficient of D= 7.1x10^{-6} cm^2.s^{-1}. For 306 electrodes, having a radius of 22.5 µm, with a recess depth L of 4 µm, the expected current was 1.54 µA. Compared to the experimental 1.2 µA measured, it is estimated that the e-beam MEAs were 78% active. The inactivity of certain electrodes could be attributed to any of several effects such as presence of air bubbles in the electrode depletion region, insulator remaining at the surface of the electrode or a discontinuity of the electronic circuit.

In the case of the electroplated electrodes, the 18.6% increase of the surface measured earlier was taken in account, and the radius was corrected with a factor of √1.186, bringing it to 24.5 µm. For 306 electrodes, having an effective radius of 24.5 µm, with a recess depth of 4 µm, the expecting current was 1.8 µA. Compared to the experimental 1.6 µA measured, it is estimated that the electroplated MEAs were 88% active.

Experimental results showed that increasing the surface roughness has a greater effectiveness than increasing the radius of the electrodes. The final activity of the electroplated MEA was higher even when the equivalent radius increase was taken in account. Nevertheless, the roughness increase had to be modest enough so as to not modify the radial shape of the diffusion layer, which is the characteristic of microelectrodes.

5.7. INFLOW ANALYSIS

After static fluid analysis, the application of the device was extended to flow injection analysis (FIA). FIA has a direct application for chemical synthesis, where the concentration of the analyte needs to be monitored in time. The measurements required the flow to be at a laminar regime.

The liquid velocity within the microdevice channels was simulated in order to:

- monitor the flow turbulence at the recessed electrodes
- correlate the analyte diffusion coefficient with the flow rate at the diffusion layer
- confirm that the diffusion layer did not interfere with the channels walls

The simulation was performed with the computer aid design COMSOL.

The electroanalytical technique used for experimental inflow measurements was the chronoamperometry, which background theory is described in Chapter 1.

5.7.1. Microchannels Flow Simulation: COMSOL

COMSOL is a finite element modelling package which allows simulation for processes involving multiphysics problems. Building a program in COMSOL consists on modelling the device, solving the simulation and extracting the desired data from it. The main steps of those can be described as follows:

- Selecting the application mode
- Defining the system parameters and variables
- Building the model
- Defining the simulation parameters
- Extracting the data

Application mode

This first step defines the main axes of the simulation, its dimension, its physics and its time dependence. For the modelling of the flow rate at the recessed electrode within the microchannels, the space dimension chosen was the 2D. The channel had a rectangular section and the electrode was situated in the middle of its length, as showed in Fig. 102. The symmetry of the system allowed simplifying the simulation from 3 to 2 dimensions while still allowing access to all the information about the flow kinetics at the electrode surface (Fig. 103). The physics chosen was fluid flow for a single phase flow in a laminar regime. In this case, the flow simulation involved kinetics and therefore was time dependent (as opposed to stationary).

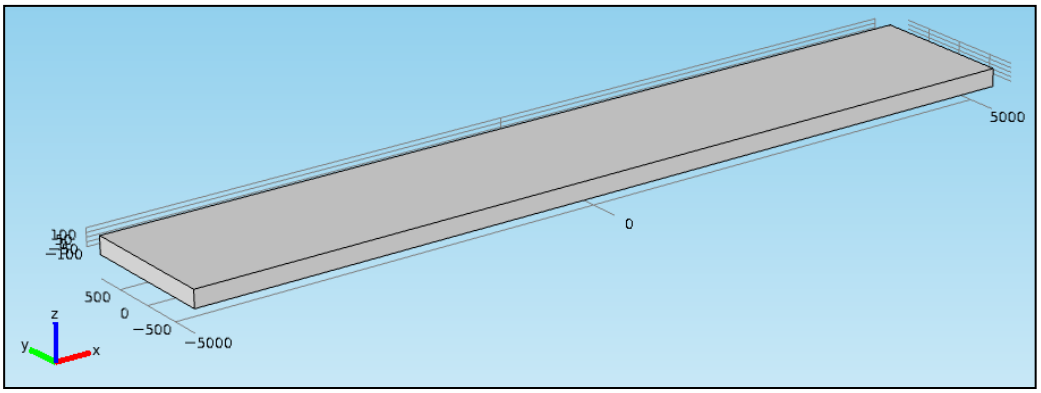

Fig. 102. 3D view of the channel where the dimensions are in µm.

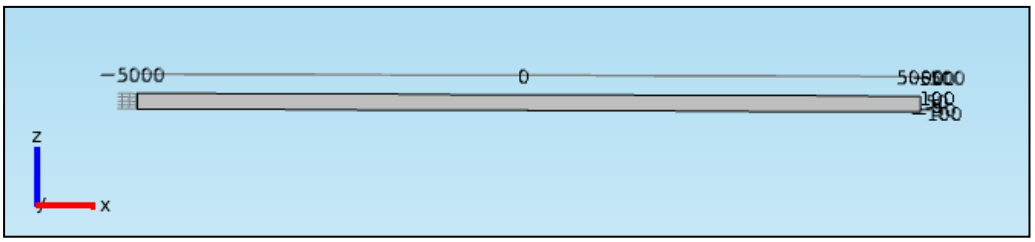

Fig. 103. 2D view of the channel where the dimensions are in µm.

System parameters and variables

The system parameter for this simulation was the flow velocity, U. It was chosen in order to have a Reynolds number less to 2000, which characterises laminar flow[142] (Eq. 34).

Eq. 34
$$Re = \rho u D_H / \mu$$
$$D_H = 4A/P$$

where ρ is the density of the fluid (kg/m^3), u is the flow velocity (m/s), D_H is the channel hydraulic diameter (m), μ is the dynamic viscosity of the fluid (kg/(m.s)), A is the cross sectional area of the channel (m^2) and P is the wetted perimeter of the channel (m).

The solvent in the channel was acetonitrile, with a density of 777 kg/m^3 and a viscosity of 3.4 $\times 10^{-4}$ kg/(m.s). The cross sectional area of the channel was 3.2 $\times 10^{-7}$ m^2 and the wetted perimeter was 3.6$\times 10^{-3}$ m. The channel hydraulic diameter was therefore 3.6 $\times 10^{-4}$ m. The flow velocity chosen was 1 $\times 10^{-4}$ m/s, for a Reynolds number equal to 0.08.

Building the model

Building the model consists of drawing its geometry, defining the materials and the equations involved.

- Channel geometry

As mentioned earlier, the channels were 200 μm high. The microelectrodes were 45 μm in diameter, 2 μm recessed and 800 μm separated from each other. Fig. 104 shows the domain of the simulation.

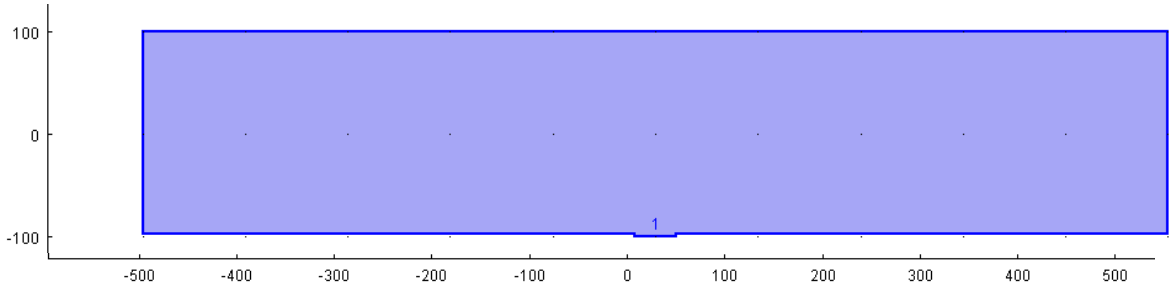

Fig. 104. Simulation domain where the dimensions are in μm.

- Material

Fig. 105 shows the boundaries of the domain. The acetonitrile flow inlet was at the boundary 1 and the outlet was at the boundary 8.

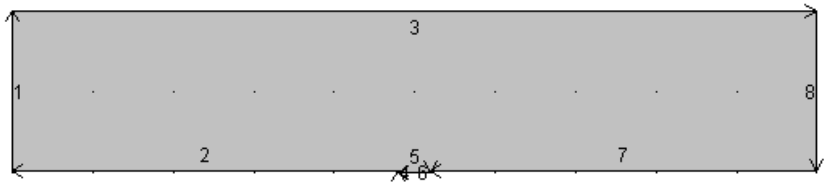

Fig. 105. Channel boundaries.

- Laminar flow equations

The model for the laminar flow of acetonitrile was built from the Navier-Stokes and Euler equations.

Navier-Stokes equation:

$$\rho\frac{\partial u}{\partial t}+\rho(u.\nabla)u=\nabla.\left[-\rho I+\mu\left(\nabla u+(\nabla u)^{T}\right)-\frac{2}{3}\mu(\nabla.u)I\right]+F$$

where u is the flow velocity (m.s^{-1}), ρ is the fluid density (kg.m^{-3}), p is the pressure (kg.m^{-1}.s^{-2}), I is the unity tensor and F is the body force term (kg.m.s^{-2}).

Euler incompressible flow equation:

$$\frac{\partial\rho}{\partial t}+\nabla.(\rho u)=0$$

Simulation parameters

The parameters related to the building of the simulation were the meshing and the time step used in creating a flow model.

- Meshing

The mesh determines the detail with which the simulation should be run. It is defined by its size, its shape and its position. The finer the meshing is, the more accurate the simulation is. For the flow simulation in the microchannels, the mesh chosen was fine and its direction was set to be defined automatically by the program in order to have finer definition around edges and geometrical variations.

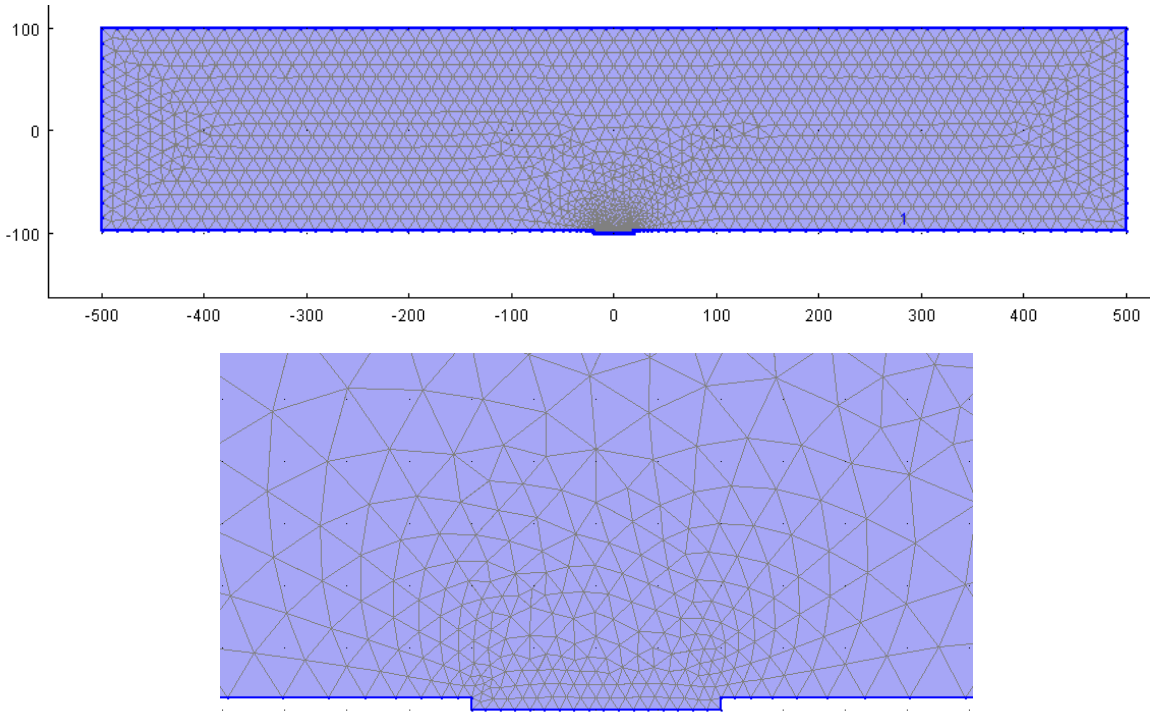

Fig. 106. Mesh where the dimensions are in μm.

- Solver configuration

The model was solved every 0.02 s, over the time interval 0 to 3 s.

Result extraction and discussion

Fig. 107 shows the flow kinetic simulation for an initial flow of 1.5 $\times 10^{-4}$ m.s^{-1}. The velocity reaches a maximum of 1.52 $\times 10^{-4}$ m.s^{-1} (in dark red) at the centre of the channel and a minimum of 0 m.s^{-1} (in dark blue) at the wall and electrode surface.

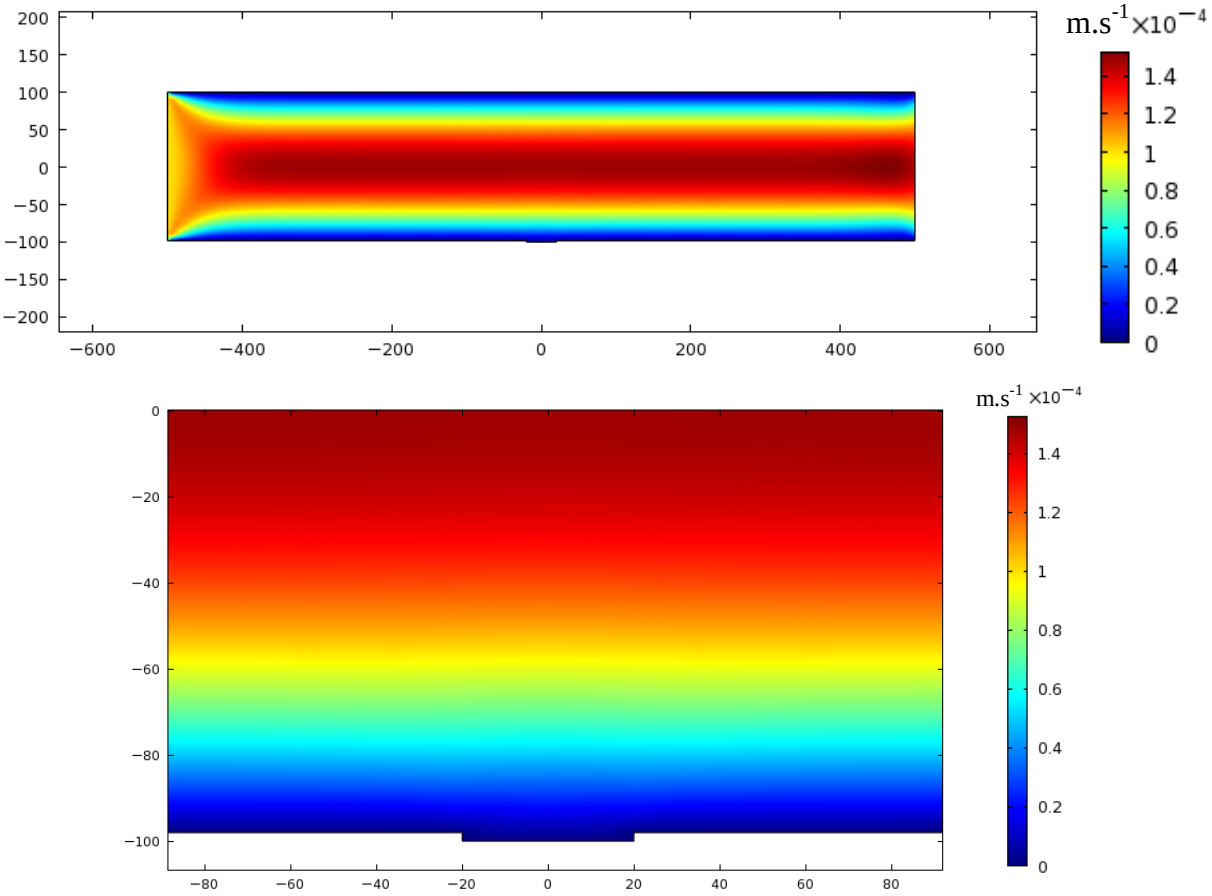

Fig. 107. Flow kinetic simulation where the dimensions are in µm.

The flow rate gradient affected the electroanalysis by renewing the chemical concentration within the diffusion layer. The scale of flow kinetic concerned in the diffusion layer could be estimated by calculating the diffusion layer thickness. The diffusion layer thickness at the microelectrode is defined as followed[9]:

Eq. 35 $$\delta = \sqrt{\pi D t}$$

where D is the diffusion coefficient of the electroactive probe (cm^2.s^{-1}) and t is the time necessary to reach the steady state (s).

The microdevice was tested in the presence of TEMPO and the resulting thickness of the diffusion layer was 58 µm.

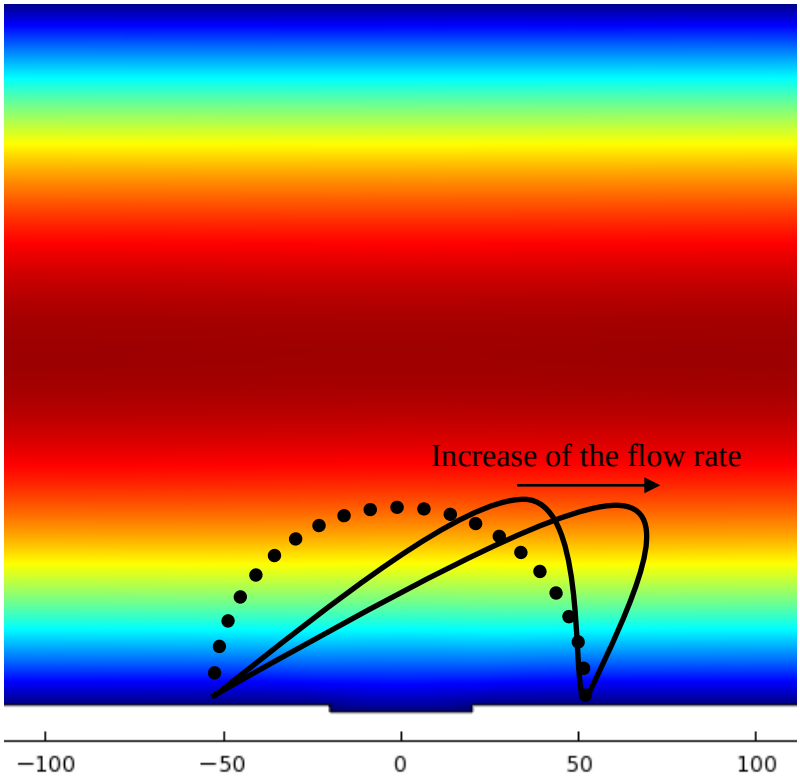

Fig. 108. Diffusion layer size within the channel where the dimensions are in µm.

The spherical diffusion layer at the microdisc is represented to scale by a dashed black line in Fig. 108. The typical diffusion layer deformations for inflow analysis are represented by the black lines on the same figure. The deformation depended on the flow rate; the faster the flow rate, the more deformed the initial shape became. Furthermore, the comparison between the diffusion coefficient of the analyte and the flow rate gave further information on the amplitude of the deformation. The diffusion coefficient of the TEMPO was 2.15 $\times 10^{-8}$ $m.s^{-1}$ and the flow rate in the diffusion layer was up to 5 $\times 10^{-5}$ $m.s^{-1}$, which indicated that in this study the inflow electroanalyses were very influenced by the flow rate.

5.7.2. CA Analysis Supported by the Microelectrode Array

Fig. 109 shows the chronoamperometry analyses supported by the microdevice performed on a flow of TEMPO solution with concentration varying between zero and 5 mmol.L^{-1}, at a flow rate of 1 ml/h. The potentials applied were 0.1 V, where the redox TEMPO was inactive, and 0.6 V, where the TEMPO was oxidised. The device showed a good capability to detect the change of concentration as the current response went from nothing to a stabilised current, when the concentration was constant (red voltammogram in Fig. 109).

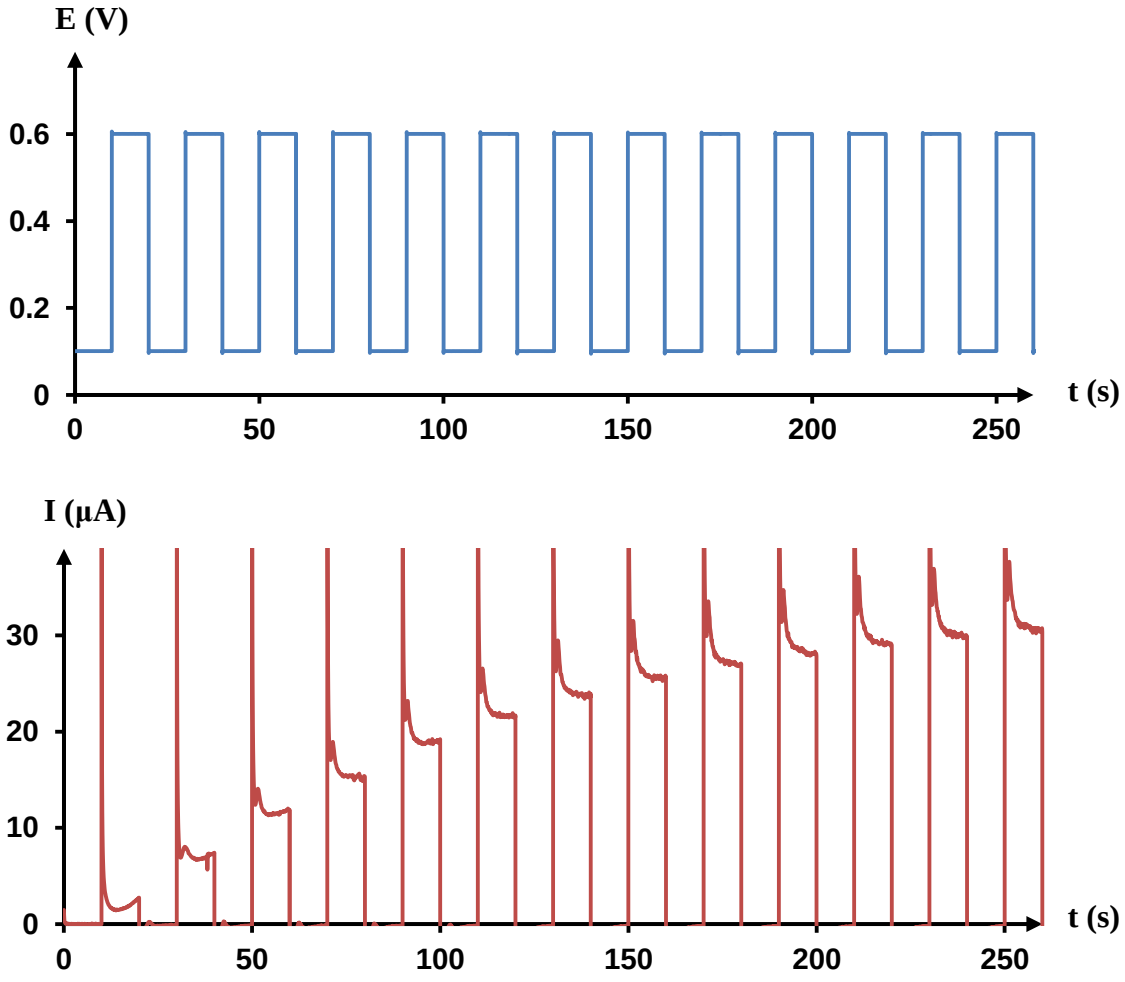

Fig. 109. CA of MEA, in the presence of TEMPO in NaClO4 (0.1mol/L) in acetonitrile.

5.8. CONCLUSION

An array of 306 gold recessed microelectrodes (45 µm diameter) was fabricated using photolithography, metallisation and oxygen plasma treatment processes. The fabrication of the microdevice described in this chapter proved to be robust and reproducible. Using gold for working, pseudo reference and counter electrodes permitted the simplification of the fabrication process. The stability of the system where all three electrodes were made of gold was established before further analyses. The CV responses of the MEAs were in accordance with the theory, with steady state current and no dependence to the scan rates.

The influence of the method of fabrication on the final response of the electrode was established and the electro-activity of the electrode could be enhanced, while maintaining the microelectrode properties, by increasing the surface roughness of the electrodes. The modification of roughness was achieved by choosing electroplating over e-beam metallisation during the fabrication process. Experimental results showed that increasing the surface roughness not only increased the current, but also had a greater effectiveness than increasing the radius of the electrodes. For an increase of the active surface of 18.6% the limited current measured was 33% higher. Nevertheless, the roughness increase had to be kept low in order to not alter the spherical shapes of the diffusion layers of the microelectrodes.

The microdevice also proved good capability to be used in flow injection analysis for chronoamperometry analysis. The kinetic of the flow within the microchannels could be modelled successfully using COMSOL multiphysics.

6. SELF-ASSEMBLED MONOLAYER

Self-assembled Monolayer's (SAM) are of interest as a way to functionalise the electrode surfaces and so give them specific properties and extend their field of application. This chapter presents the surface modification of the gold macro and MEA electrodes to make them capable of enantiomer recognition, and to extend their application to biosensors. The electrodes were modified with glutathione and cysteine chiral molecules to investigate their ability to recognise the proline enantiomers in Electrochemical Impedance Spectroscopy (EIS) analysis. The properties of the macro and micro array electrodes were extended to biological applications by modifying their surfaces with thiolated single stranded DNA. The monolayers were all studied using cyclic voltammetry and impedance spectroscopy analysis. The electron transfer resistance and impedance of each monolayer were accessed from the EIS analyses and used to calculate and compare their electron transfer rate.

6.1. INTRODUCTION

A self-assembled monolayer can be defined as a layer of molecules that spontaneously organise themselves side by side into a specific and reproducible arrangement at the interface between two phases. An interaction with a targeted molecule can be designed by choosing the appropriate head groups and monolayer organisation. In the context of using electroanalysis for chiral recognition, SAM modification can be used to promote the enantioselectivity of the electrode surface by introducing chiral interactions between the analyte and the molecule composing the monolayer. Burgi et al. worked on chiral differentiation at SAM surfaces[109,110] and developed Attenuated Total Reflection Infrared (ATR-IR) and Modulation Excitation Spectroscopy to show the ability of L-glutathione and cysteine (Fig. 110) modified electrodes to interact enantioselectively with (D)-proline enantiomer[111,112]. Electroanalysis such as CV and EIS techniques allow the study of kinetics parameters, surface coverage and structure of the SAM. One objective of this study was to find out if the glutathione and cysteine enantioselective interactions could be characterised using CV and EIS analytical techniques.

Furthermore, SAM modification could also be used to extend the range of application of the microelectrode array to bio-sensing by modifying the surface of the microdisc electrodes with thiolated DNA (Fig. 110).

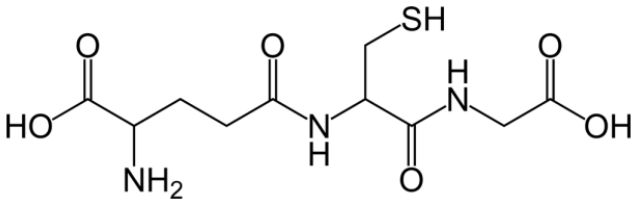

Glutathione

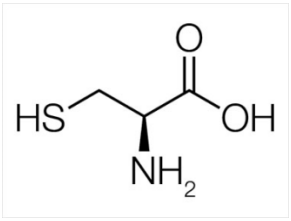

Cysteine

5’-GGGAGTCAAGAACGAA$(CH_2)_3$SH-3’

Thiolated Oligonucleotide

Fig. 110. Molecules tested for self-assembled monolayer modification on a gold electrode.

The analyses of the monolayers consisted of CV analysis, where the presence of pinholes was identified, and EIS to study the structure of the monolayer and the kinetics of the electron transfer. Relating experimental impedance data to physical values required the fitting of equivalent electronic circuits and the method is explained in the following section.

.

6.2. ELECTROCHEMICAL IMPEDANCE SPECTROSCOPY - EQUIVALENT CIRCUIT

This section expands on the impedance spectroscopy presentation of the first chapter, and details the experimental data analyses.

EIS helps in the understanding of the kinetics of the electrochemical process taking place at the electrode surface by measuring the total impedance of the system over a wide frequency range. The data collected are organised in Nyquist and Bode plots. In the first one, the real part of the impedance, Z', is plotted versus the imaginary part, Z''. The Bode plots present, versus the frequency, the total magnitude of the impedance, $|Z|$, and the phase angle between Z' and Z'', φ. Fig. 111, Fig. 112 and Fig. 113 show examples of Nyquist and Bode plots for frequencies going from 100 kHz to 0.1 Hz.

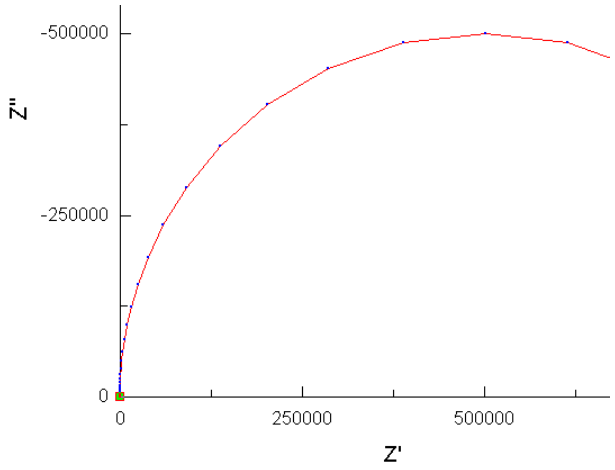

Fig. 111. Nyquist plot. Imaginary part of the impedance, Z'', versus its real part, Z'.

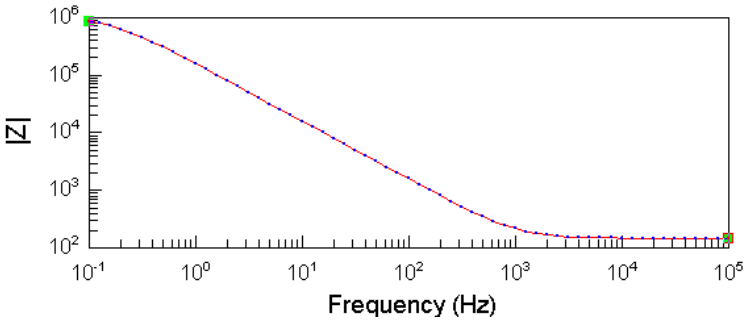

Fig. 112. Bode plot. Absolute value of the impedance, $|Z|$, versus the frequency.

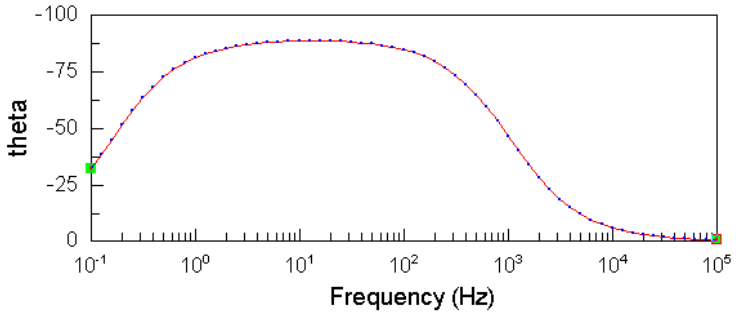

Fig. 113. Bode plot. Phase angle modulation, φ, versus the frequency.

To determine the capacitance and resistance values from experimental data, an equivalent electronic circuit is built and component values are chosen to fit Nyquist and Bode plots of EIS data.

The software used to model the equivalent circuits in this study was Zview. The typical electronic circuit equivalent to the electrode surface was composed of two resistors and a capacitor (more precisely a Constant Phase Element, CPE). Each element of the equivalent circuit can relate to a physical phenomena taking place at the surface of the electrode in the presence of redox active species.

- The resistance R1 represented the resistance of the solution.
- The resistance R2 represented the charge transfer resistance.
- The capacitor represented the capacitance of the double layer.

The equivalent electronic circuit is showed in Fig. 114.

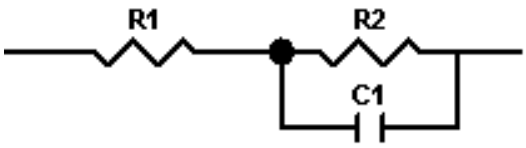

Fig. 114. Equivalent electronic circuit of the electrode in solution.

As described in the literature review, the impedance resulting from combining resistors with capacitors is an imaginary number, where the absolute value and phase angle are given by:

$$Z = \sqrt{Z'^2 + Z''^2}$$

$$\varphi = \tan^{-1}\frac{Z''}{Z'}$$

The total impedance of the circuit presented in Fig. 114 is the sum of the impedance of the resistor, Z_{R1}, and the impedance of the combined resistor-capacitor, Z_{R2C}.

Eq. 36 $$Z = Z_{R1} + Z_{R2C}$$

As R_2 and C_1 are connected in parallel the resulting impedance Z_{R2C} can be expressed as a complex number shown in Eq. 37.

Eq. 37 $$\frac{1}{Z_{R2C}} = \frac{1}{R_2} + \frac{1}{1/i\omega C_1}$$

$$Z_{R2C} = \frac{\frac{R_2}{i\omega C_1}}{R_2 + \frac{1}{i\omega C_1}} = \frac{R_2}{1 + i\omega C_1 R_2}$$

By multiplying the top and bottom of the ratio by the complex conjugate $1\text{-}i\omega C_1R_2$ the real and imaginary part could be dissociated.

Eq. 38 $$Z_{R2C} = \frac{R_2}{1+(\omega C_1 R_2)^2} - i\frac{\omega C_1 R_2^2}{1+(\omega C_1 R_2)^2}$$

where the first term of the equation is the real part and the second one the imaginary part.

Combining Eq. 36 and Eq. 38, the total impedance of the circuit, Z, was expressed as follows:

Eq. 39 $$Z = R_1 + \frac{R_2}{1+(\omega C_1 R_2)^2} - i\frac{\omega C_1 R_2^2}{1+(\omega C_1 R_2)^2}$$

Real part: $$Z' = R_1 + \frac{R_2}{1+(\omega C_1 R_2)^2}$$

Imaginary part: $$Z'' = -\frac{\omega C_1 R_2^2}{1+(\omega C_1 R_2)^2}$$

Fig. 116 and Fig. 117 show 4 examples of Bode and Nyquist plots to illustrate Eq. 39 and understand the influence of the parameters R_1, R_2 and C_1 on Z', Z'' and $|Z|$ (Fig. 115).

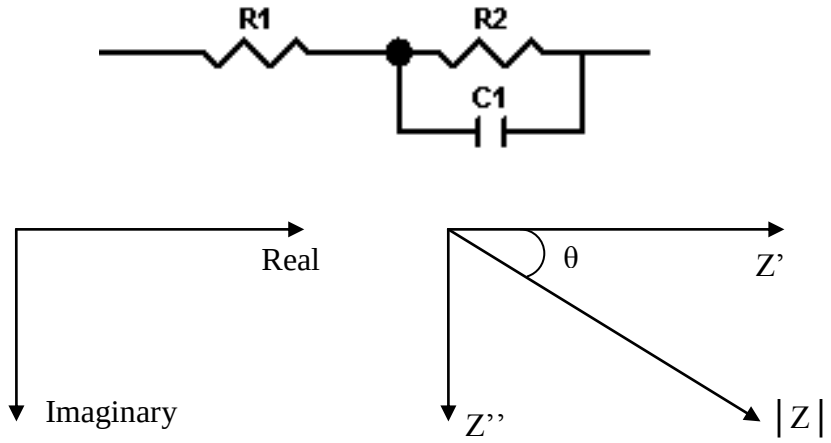

Fig. 115. Equivalent circuit and relation between Z', Z'', $|Z|$ and θ.

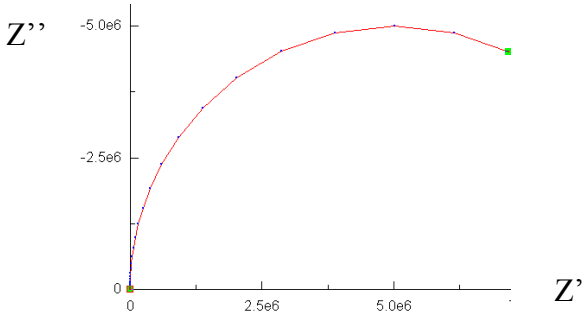

R_1	500 Ω
R_2	10 MΩ
C_1	0.1 µF

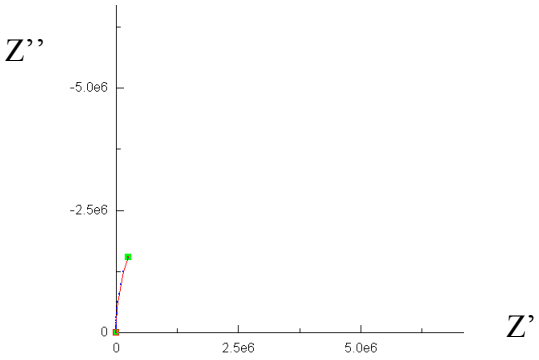

R_1	500 Ω
R_2	10 MΩ
C_1	1 µF

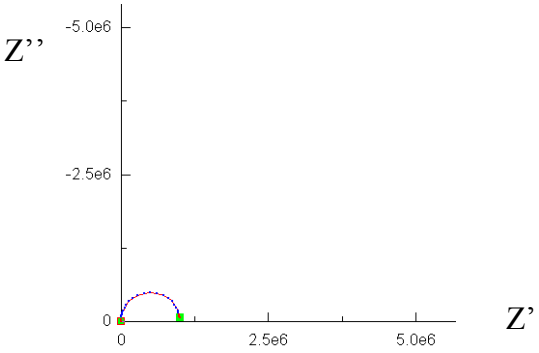

R_1	500 Ω
R_2	1 MΩ
C_1	0.1 µF

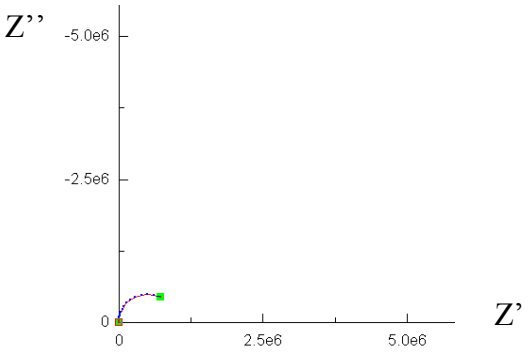

R_1	500 Ω
R_2	1 MΩ
C_1	1 µF

Fig. 116. Nyquist plots for different R_1, R_2 and C_1.

R_1	500 Ω
R_2	10 MΩ
C_1	0.1 µF

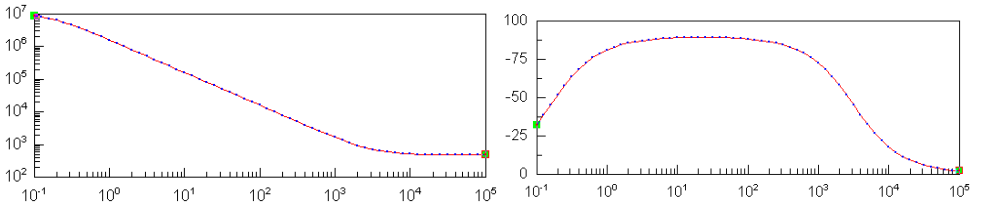

R_1	500 Ω
R_2	10 MΩ
C_1	1 µF

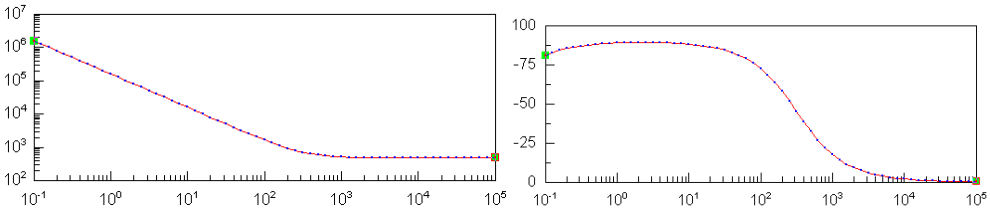

R_1	500 Ω
R_2	1 MΩ
C_1	0.1 µF

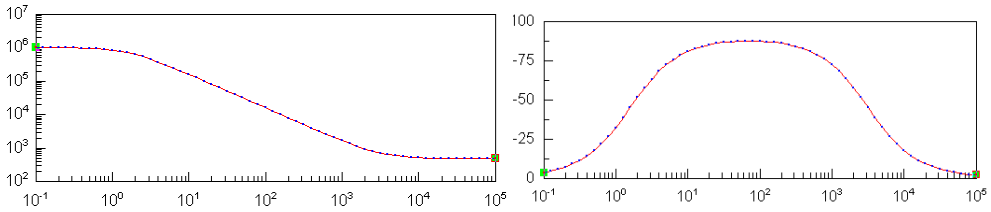

R_1	500 Ω
R_2	1 MΩ
C_1	1 µF

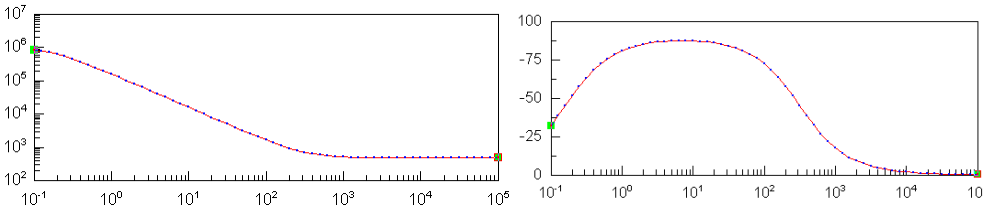

Fig. 117. Bode plots for different R_1, R_2 and C_1.

In practice, a Constant Phase Element (CPE) was used instead of a capacitor to represent the double layer capacitance. The relation between CPE and a capacitor is that a capacitor is a CPE with a constant phase angle of 90 degrees. The CPE compensates for non-homogeneity in the system caused by a rough or porous surface, and has a phase angle of $(90\times n)^{o}$, with n comprised between 0 and 1. The impedance resulting from the same equivalent circuit described earlier but with a CPE instead of a capacitor is described as follows:

Eq. 40 $$Z = R_1 + \frac{R_2}{1+(\omega^n C_1 R_2)^2} - i\frac{\omega^n C_1 R_2^2}{1+(\omega^n C_1 R_2)^2}$$

In the case of a modified electrode, the circuit was corrected to fit the experimental circuit by adding a Warburg element, W_S, as showed in Fig. 118.

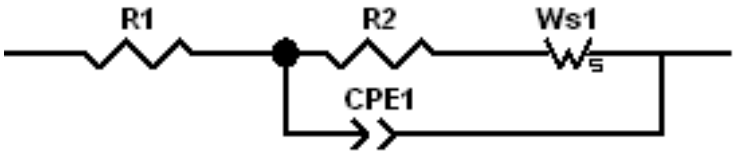

Fig. 118. Equivalent electronic circuit of modified gold.

The Warburg element characterised the charge diffusion through the monolayer. Lower frequencies correspond to deeper diffusion into the material. W_S and R_2 together represented the faradic impedance.

6.3. BARE GOLD ELECTRODE CHARACTERISATION

Cyclic voltammetry and impedance spectroscopy analysis were first performed on the unmodified gold macro and micro array electrodes in order to characterise their cleanliness and compare their impedance. The optimum cleanliness of the surfaces before surface modification was a major requirement as any contamination or dirt could generate defects during the monolayer formation.

6.3.1. Cleanliness Characterisation

The cleanliness of the electrode was characterised by CV analysis in a 1 mol/L sulphuric acid solution between 0 and 1.5 V (vs Ag/AgCl/KCl 3.5 mol/L reference electrode). As the applied potential successively increased and decreased, the outer layer of gold was oxidised and reduced. The electrode was considered clean for a stripping charge higher than 1.4 µC.cm^{-2} [143]. Fig. 119 and Fig. 120 show respectively the CV responses for the macroelectrode and the MEA used in this study.

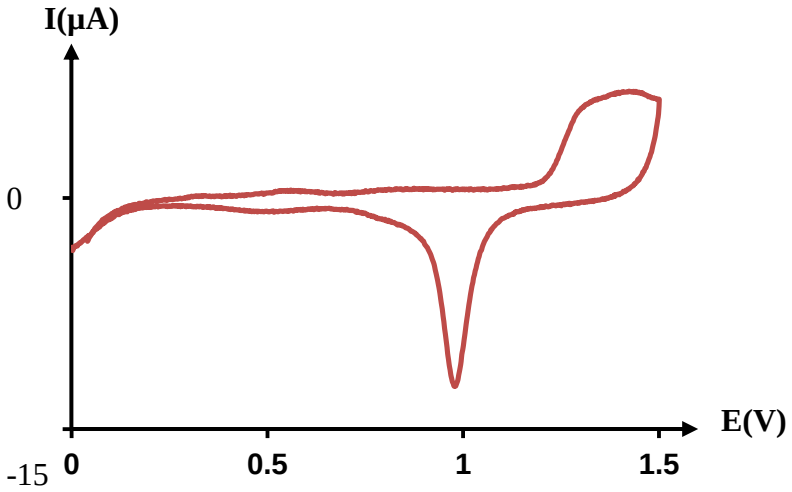

Fig. 119. Au bare macroelectrode in H_2SO_4 using a scan rate of 100 mV/s.

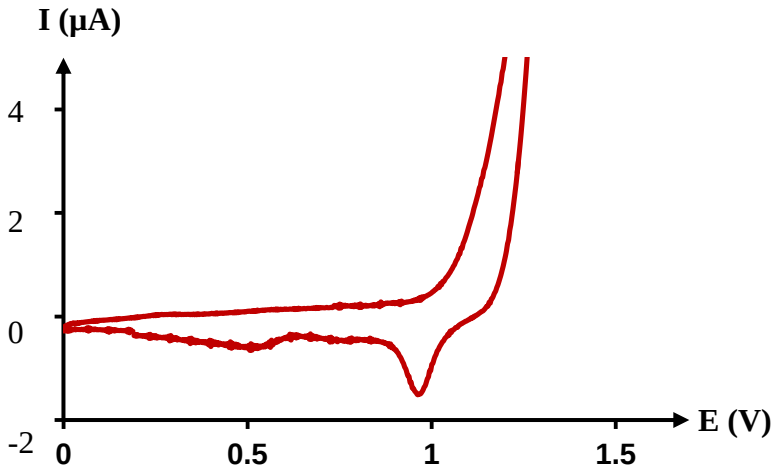

Fig. 120. Au bare microelectrode array in H_2SO_4 using a scan rate of 100 mV/s.

The stripping charge was quantified from the cathode peak at 0.95 V versus Ag/AgCl reference. This peak amplitude was 12 µA for the macroelectrode and 1.5 µA for the microelectrode array corresponding to a stripping charge higher than 1.4 $\mu C.cm^{-2}$ in both cases, which confirmed the cleanliness of the electrode surfaces.

6.3.2. Cyclic Voltammetry Analysis of the Bare Gold

In this chapter, CV analyses were used to detect the presence of pinholes in the monolayer formed at the surface of the electrodes. Preliminary analyses consisted of characterising the unmodified gold electrode. The clean electrodes were tested in $K_3Fe(CN)_6$ (1 mmol/L) solution. Fig. 121 and Fig. 123 show the CV results obtained from an unmodified macroelectrode and MEA, respectively. The reversible reduction of ferricyanide occurred at 0.25 V against a Ag/AgCl reference electrode.

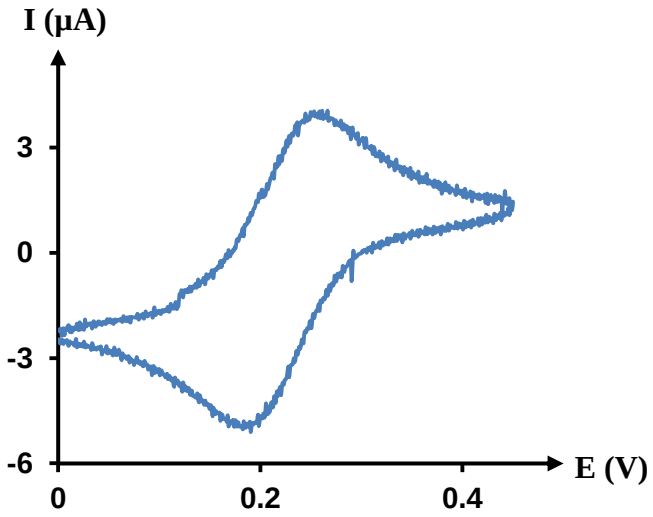

Fig. 121. CV for Au macroelectrode in $K_3Fe(CN)_6$ in water containing KNO_3 electrolyte, using a scan rate of 100 mV/s.

Fig. 121 shows a voltammogram with the typical Nernstian shape characteristic of a macroelectrode. I_{pa}= 4.8 µA and followed the Randles-Sevcik equation (Eq. 5) where $I_{pa}=2.69\times10^5 z^{3/2} C A D^{1/2} \upsilon^{1/2}$, using D= 7×10^{-6} cm^2/s for the ferricyanide diffusion coefficient. The same experiments were performed at different scan rates to establish the proportional relation between the peak current and $\sqrt{\nu}$ (Fig. 122).

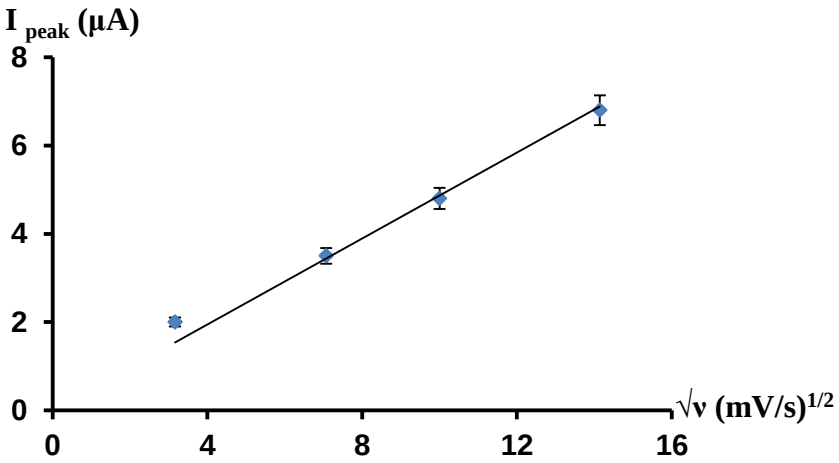

Fig. 122. Relation between $\sqrt{\nu}$ and I_{peak} at a DNA modified electrode, in the presence of ferricyanide.

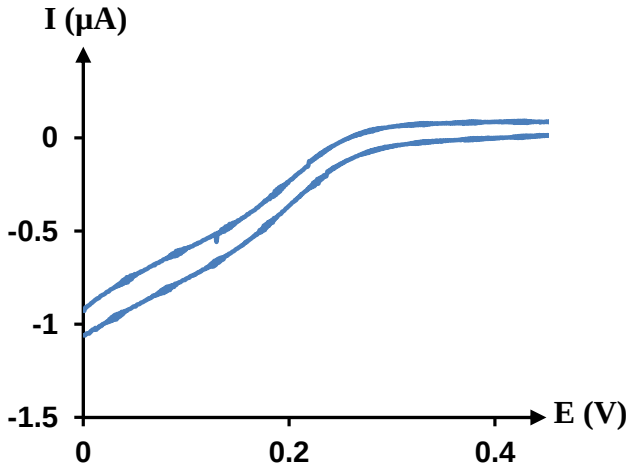

Fig. 123. CV for Au MEA in $K_3Fe(CN)_6$ in water containing KNO_3 electrolyte, using a scan rate of 100 mV/s.

Fig. 123 shows a voltammogram with the typical sygmoidal shape characteristic of a microelectrode. I_{ss}= 1 µA and followed the equation (Eq. 11) where $I_{ss} = n4zFDCae^{(-0.96L/a)}$, using D= 7×10^{-6} cm^2/s for the ferricyanide diffusion coefficient. The current measured was constant for CV analyses run at different scan rates.

Both the responses of the macroelectrode and of the MEA fitted the theory and described the standard behaviour of $K_3Fe(CN)_6$ at a bare gold surface.

6.3.3. Electrochemical Impedance Spectroscopy on Bare Gold

The first EIS analyses were performed using an unmodified gold electrode to compare the responses of macro and microarray electrodes. The measurements were made on $K_3Fe(CN)_6$ (1 mmol/L) solution for frequencies going from 100 kHz to 0.1 Hz. Fig. 124 shows the Nyquist plot of the macroelectrode response at the analyte redox potential. On the left is the whole plot and on the right is a zoom of the low values of Z' and Z''.

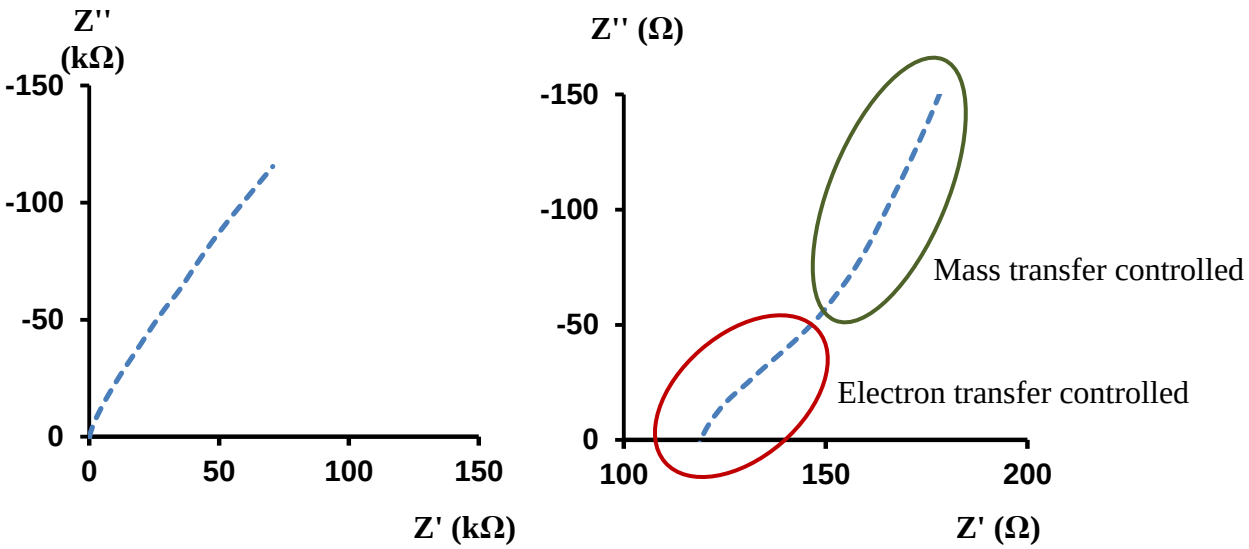

Fig. 124. Nyquist plot for unmodified gold macroelectrode in $K_3Fe(CN)_6$.

The kinetic of the system is dictated by the slowest process between mass transfer and charge control. The EIS response of the bare electrode was composed of a straight line for the major part of the frequencies spectrum indicating that the process was controlled by mass transfer and that the redox reaction and charge transfer were taking place without obstruction. The zoom of the plot on its low values showed that part of the response also had a curved shape part characteristic of the electron transfer control. The small curved portion where the electron transfer was limited corresponded to the kinetics of the diffusion layer. The fitting of the data with the equivalent circuit allowed the determination of values for the charge transfer resistance and capacitance of the diffusion layer (Fig. 125). The charge transfer resistance was 150 Ω and the capacitance was 0.2 μF.

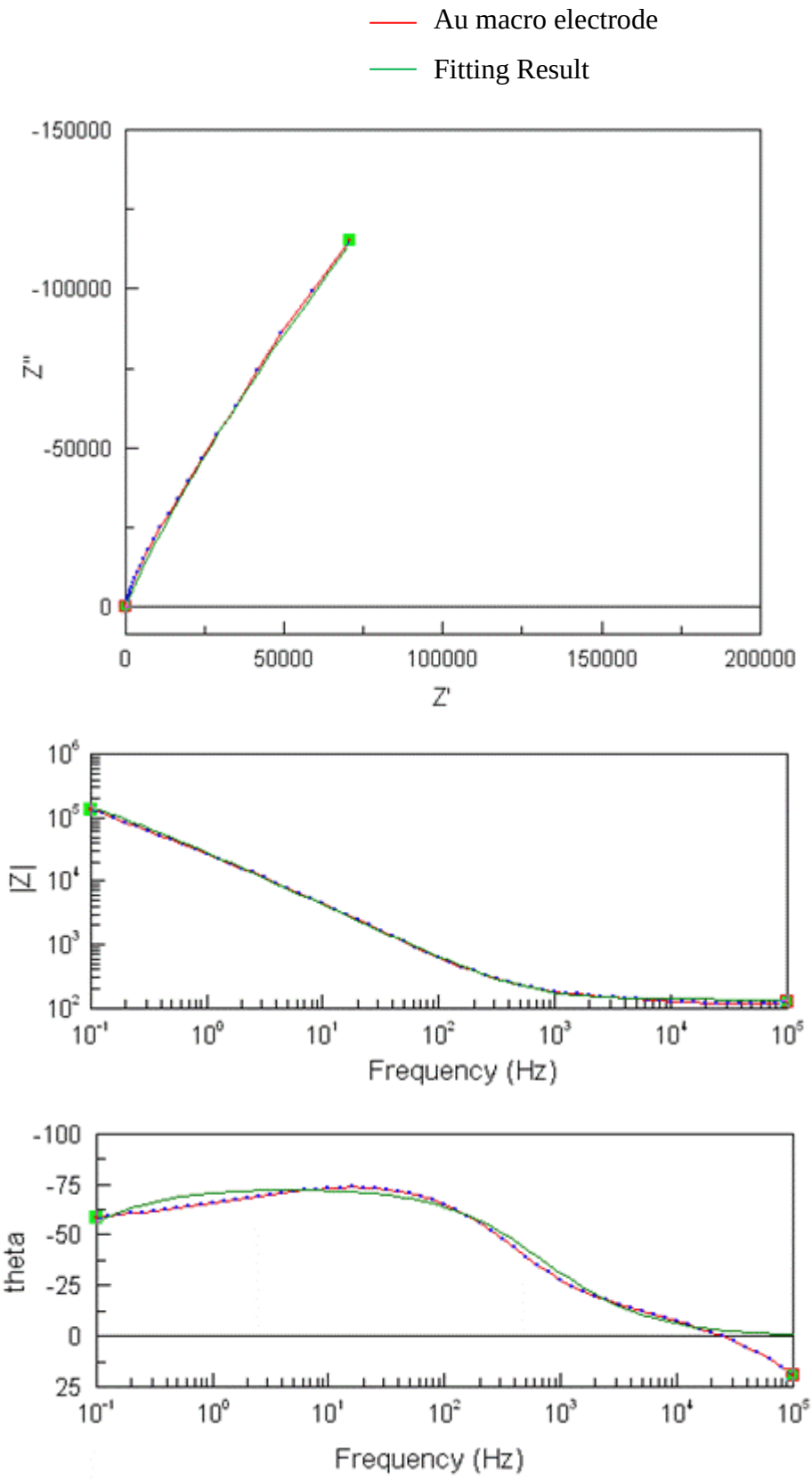

Fig. 125. Example of fitting curve for equivalent circuit.

The same analyses were performed using the microelectrode array. The Nyquist plot for the microelectrode array at the analyte redox potential is showed in Fig. 126.

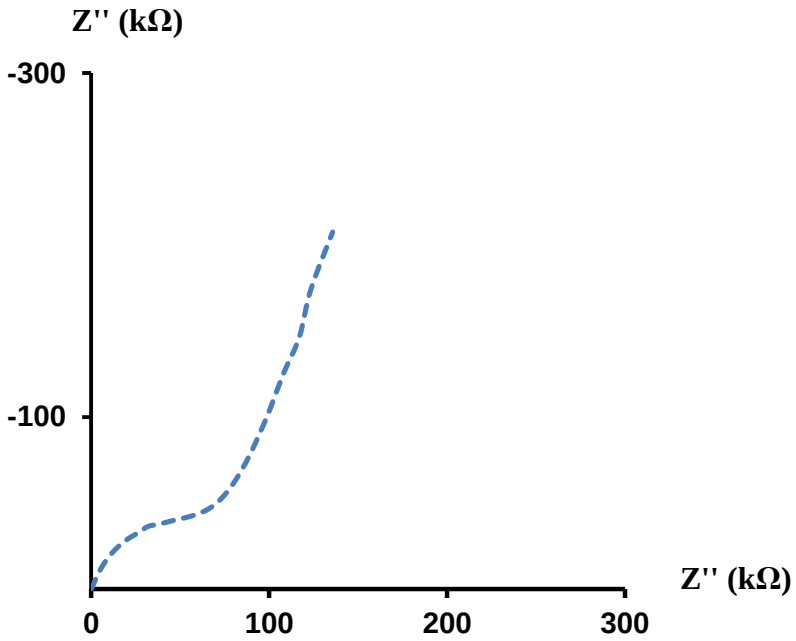

Fig. 126. Nyquist plot for bare MEA in $K_3Fe(CN)_6$.

Like the response for the macroelectrode, the MEA analyses showed predominance of mass transfer control as expected for a bare electrode. The appearance of "semi circle" shapes characteristic for charge transfer control was also clear for higher frequencies, which characterised the kinetic at the diffusion layer. The fitting of the data with the equivalent circuit gave a value for the charge transfer resistance of 73 kΩ and a capacitance of 0.12 μF.

The differences of values and shapes between bare macro and bare micro array electrode were due to the sizing down of the electrode surface area. The charge transfer resistance and the capacitance are directly related to the electrode interface area[1]. The reduction of the electrode size generates an increase of the resistance and a reduction of the capacitance. When using an array of microdiscs instead of one single electrode, the variations were not directly proportional to the surface area as not only the diffusion layer shape changed, but also the proportion of edge effects increased significantly. The impedance measurements showed the increase of the charge transfer resistance expected due to the reduction of the electrode. The charge transfer resistance was 150 Ω for the macroelectrode and 73 kΩ for the microelectrode array. The capacitance also followed the theory and decreased, from 0.2 µF for the macroelectrode, to 0.12 µF for the microelectrode array. Scaling down the electrode from macro to micro implied both direct reduction of the capacitance and increase of the fringing field at the edge of the microdiscs. The fringing effect results from the electric field bowing out at the edges of the electrode. The smaller the electrode surface is, the more important the fringing effect is relative to the total electric field. This effect is illustrated in (Fig. 127).

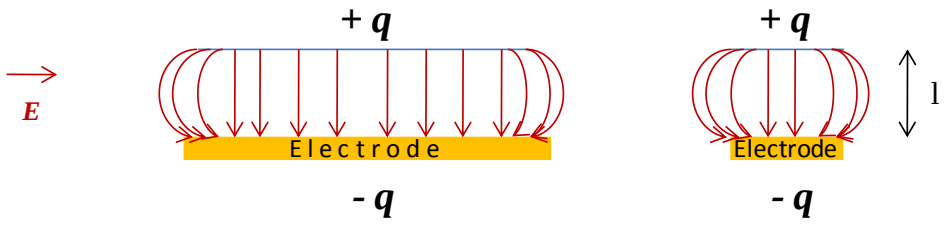

Fig. 127. Fringing field effect.

6.4. DODECANETHIOL SAM

The first molecule chosen to modify the macro and micro electrodes was dodecanethiol (Fig. 128). This molecule has been widely studied and its conditions of optimal use to get a fully covering self-assembled monolayer have been well described in the literature[79,144,145]. It was relevant to use a well-known and robust thiol to achieve the first modification of the microelectrode array.

Fig. 128. Dodecanethiol molecule.

6.4.1. DDT SAM

The modified electrodes were tested in a $K_3Fe(CN)_6$ (1 mmol/L) solution versus Ag/AgCl reference. Since the molecule wasn't conductive, the complete coverage of the electrode surface was expected to prevent electron transfer. The cyclic voltammetry analyses were used to confirm the absence of a redox reaction at the surfaces of the macro and micro electrode. Fig. 129 and Fig. 130 show the CV responses of, respectively, the modified macroelectrode and the modified MEA. Both electrodes were modified in the exact same conditions. For comparison, the response of the unmodified macroelectrode and MEA is shown in black in each case.

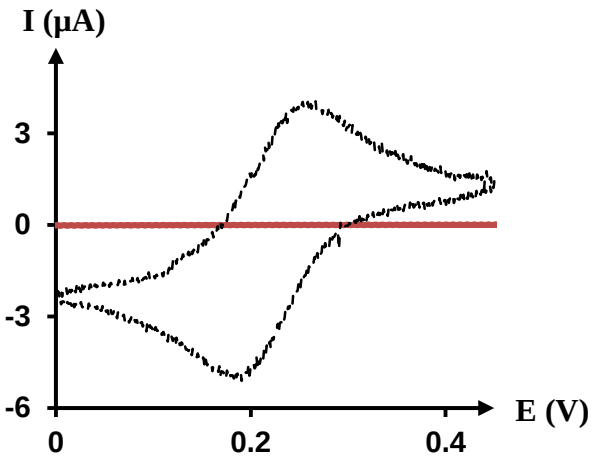

Fig. 129. In red: CV of DDT modified macroelectrode on $K_3Fe(CN)_6$ in water containing KNO_3.

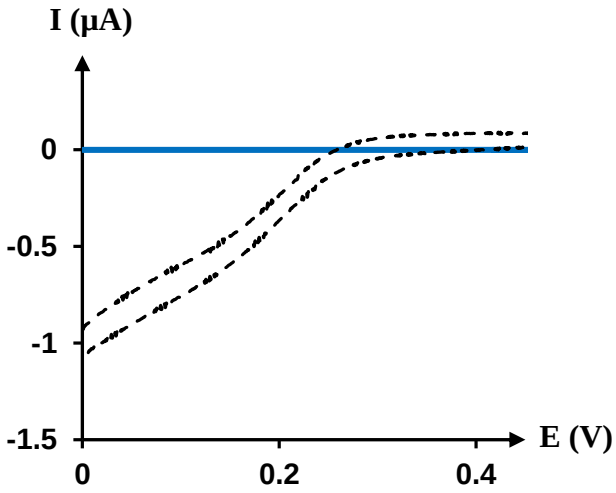

Fig. 130. In blue: CV of DDT modified microelectrode on $K_3Fe(CN)_6$ in water containing KNO_3.

The absence of peaks in the voltammogram of macro and microelectrodes confirmed the complete covering of the surface and the insulating properties of the SAM. The structure of the SAM was studied further using impedance spectroscopy. The measurements were made on $K_3Fe(CN)_6$ (1 mmol/L) solution for frequencies going from 100 kHz to 0.1 Hz. Fig. 131 shows the Nyquist plot of the macroelectrode at the analyte redox potential. Fig. 132 shows its responses for potential going from 0 to 0.7 V.

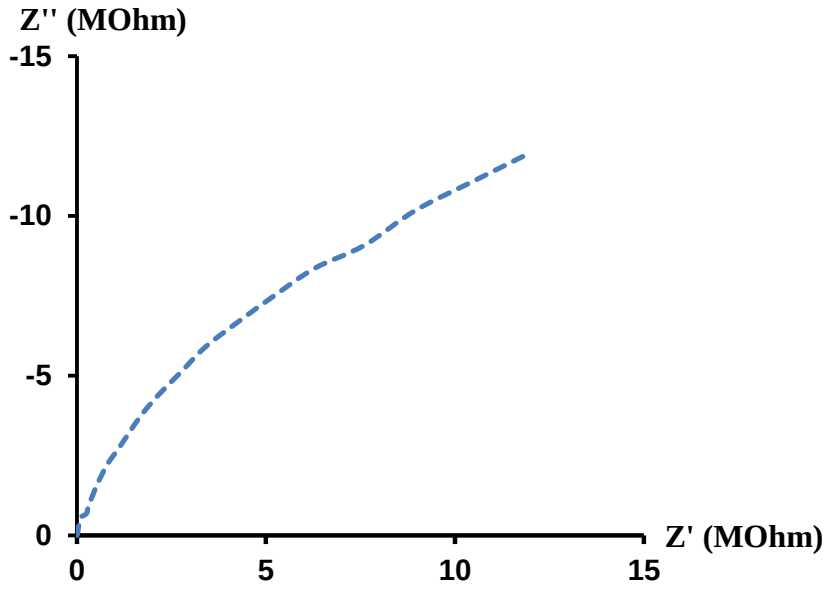

Fig. 131. Nyquist plot for gold macroelectrode modified with DDT in $K_3Fe(CN)_6$ solution.

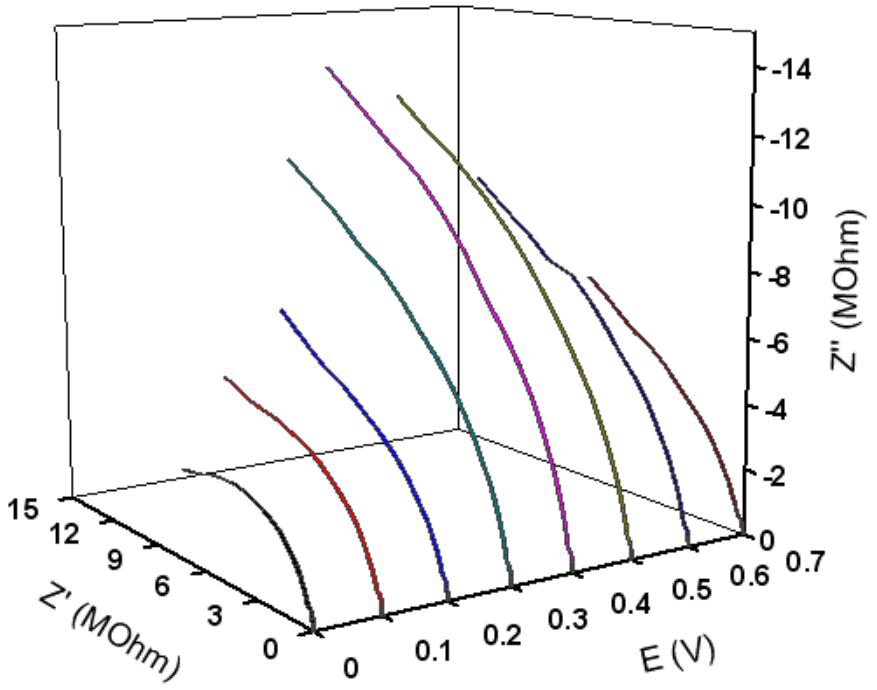

Fig. 132. Nyquist plot for gold bar electrode modified with DDT in $K_3Fe(CN)_6$ at variable potential vs reference.

As expected, the impedance was a maximum for the potential close to the potential cell, where the redox species was active. The application of potential different from the cell potential created perturbations at the SAM inducing the charge transfer resistance diminution. The charge transfer resistances and the capacitances of the monolayers were calculated from the equivalent circuit fitting the EIS plots. The charge transfer resistance for the DDT SAM was 30 MΩ and the capacitance was 90 nF. The Nyquist plot of the modified electrode had a partially circular shape indicating a charge transfer control as opposed to the straight line observed for a bare electrode, which was characteristic of mass transfer control. Those results corroborated the CV analyses; the charge transfer control occurrence for all the range of frequencies confirmed the good blocking properties of the monolayer and the absence of pinholes.

The structure of the SAM at the surface of the microdiscs was also studied and the same impedance analyses were conducted on MEA. Fig. 133 shows the Nyquist plot of the microelectrode array response at the analyte redox potential and Fig. 134 shows the response at potentials varying between 0.1 V and 0.7 V.

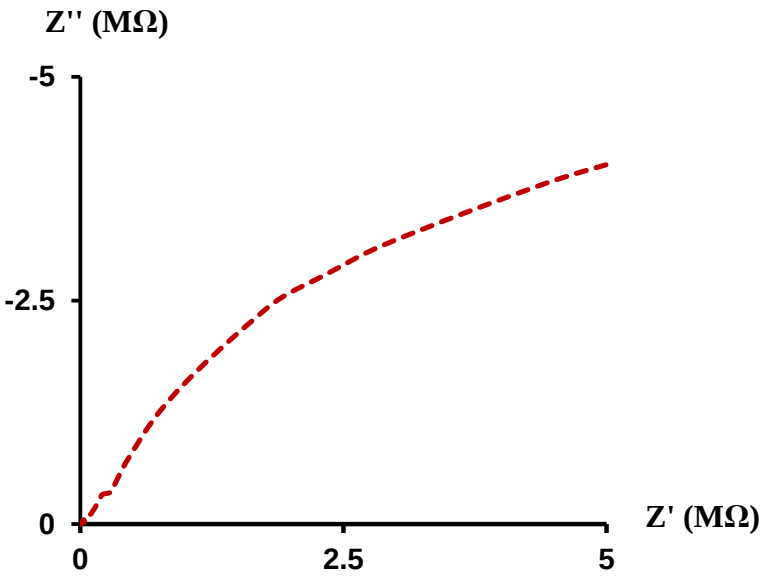

Fig. 133. Nyquist plot for gold MEA modified with DDT in $K_3Fe(CN)_6$ solution.

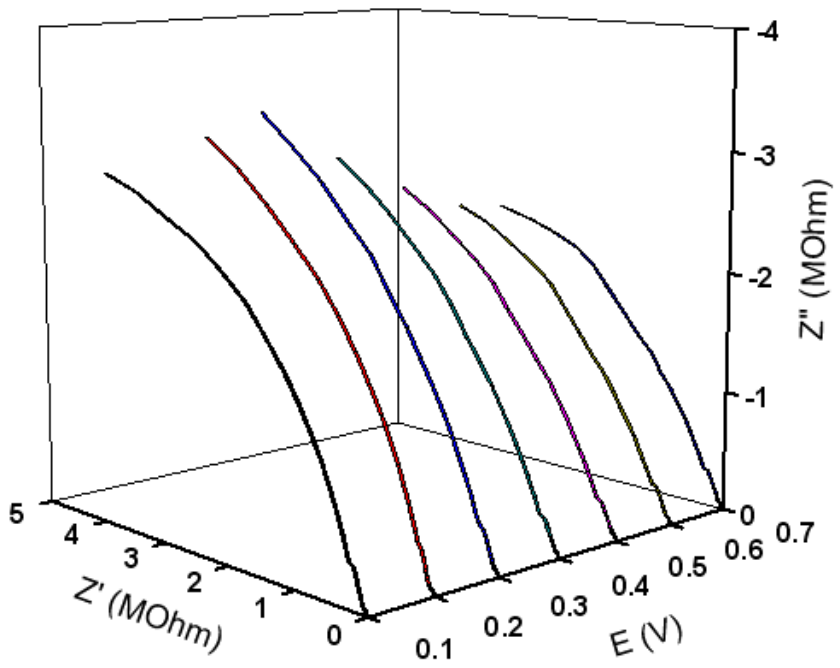

Fig. 134. Nyquist plot for gold MEA modified with DDT in $K_3Fe(CN)_6$. Variable potential vs reference.

The charge transfer resistances and the capacitances of the monolayers were calculated from the equivalent circuit fitting the EIS plots. The charge transfer resistance for the DDT SAM was 14 MΩ and the capacitance was 0.13 μF.

Similar to the responses of the macroelectrode, the Nyquist graphs of the MEA had curved shapes indicating charge transfer control, good blocking properties of the monolayer and an absence of pinholes.

6.4.2. Analysis

The surface coverage, θ, of the modified electrode represents the area of the electrode covered by the SAM[146,147]. It is calculated base on the experimental values of the charge transfer resistance of the bare and modified electrodes as shown in
Eq. 41. θ is comprised between 0 and 1, where 0 characterises a bare electrode and 1 characterises an electrode fully covered and pinhole free.

Eq. 41 $$\theta = 1 - (R_{ct}/R'_{ct})$$

where R_{ct} is the charge transfer resistance of the bare gold electrode and R'_{ct} is the charge transfer resistance of the SAM modified electrode.

The charge transfer resistance was 150 Ω for the bare gold macroelectrode and 30 MΩ for the SAM modified electrode. The resulting surface coverage was 0.99. The charge transfer resistance was 73 kΩ for the bare microelectrode array and 14 MΩ for the SAM modified electrode. The resulting surface coverage of the MEA was 0.99. These calculations confirmed the minimum presence of pinholes in the monolayer for both macro and micro electrodes.

Since the dodecanethiol monolayer was insulating and pinhole free, the only way for the electron to penetrate it was via tunneling. Following Marcus theory[87], the electron tunneling is expected to decrease exponentially with the layer thickness (Eq. 42).

Eq. 42 $$i = i_0 \exp(-\beta d)$$

where i_0 is the current measured at the bare electrode (A), β is the electrode tunneling coefficient which correlates the electron rate transfer with the chemical structure ($Å^{-1}$) and d is the length of the monolayer (Å).

For an electrochemical reaction in equilibrium, the apparent rate constant is also a function of the length of the molecule forming the monolayer (Eq. 43).

Eq. 43 $$K_{app\ Th.} = K_0 exp(-\beta d)$$

where K_{app} is the apparent electron transfer rate constant at the film covered electrode ($cm.s^{-1}$) and K_0 is the standard electron transfer rate constant at the bare electrode ($cm.s^{-1}$).

When the current is due to electron tunneling only, Eq. 43 gives access to the theoretical apparent electron transfer rate at the monolayer and Eq. 44 describes its calculation from experimental values.

Eq. 44 $$K_{app\ Exp.} = \frac{RT}{F^2 R_{ct} C}$$

where R is the gas constant (8.314 $J.K^{-1}.mol^{-1}$), T is the temperature (K), F is the Faraday constant (96484.6 $C.mol^{-1}$), C is the concentration of the redox analyte ($mol.L^{-1}$) and R_{ct} is the charge transfer resistance per unit geometric area ($\Omega.dm^2$).

The charge transfer resistances for the modified macro and microelectrode were accessed through the equivalent electronic circuit and are presented in Table 2 along with the theoretical and apparent electron transfer rate values for modified macro and micro array electrodes. The surface areas were 2 mm^2 for the macroelectrode and 0.39 mm^2 for the MEA. The length of dodecanethiol considered in the calculation was 1.4 nm. This value was corrected to 1.2 nm to take in account the 30º angle tilt of the molecule at the surface of the electrode. The β value used for the electron tunneling coefficient of an aliphatic chain[88,148] was 0.83 $Å^{-1}$. The standard electron transfer rate constant at the bare electrode, K_0, for a gold electrode in $K_3Fe(CN)_6$ solution[149] was 0.031 $cm.s^{-1}$.

	R_{ct} (Ohm)	**Theoretical K_{app} ($cm.s^{-1}$)**	**Experimental K_{app} ($cm.s^{-1}$)**
Macroelectrode	3×10^{7}	6.3×10^{-7}	4.43×10^{-7}
MEA	1.4×10^{7}	6.3×10^{-7}	4.8×10^{-6}

Table 2. Theoretical K_{app} and experimental K_{app} calculations for a DDT modified electrode.

For both macro and microelectrode, the theoretical and experimental electron transfer rates were not significantly different. The experimental transfer rate of the macroelectrode was closer to the theoretical value, and was easier to reproduce, than the one with the MEA. The variation between the experimental and the theoretical electron rates indicated that the thickness of the monolayer formed was not equal to the theoretical value of the dodecanethiol molecule tilted of 30º. By injecting the experimental apparent electron rate, $K_{app\ Exp.}$, in Eq. 43 an experimental value of the monolayer thickness could be calculated.

The thickness of the dodecanethiol SAM at the surface of the macroelectrode was found to be 12.3 Å, which was comparable to the theoretical value of 13 Å. These results confirmed that the protocol used allowed the formation of a well organised DDT molecule layer with minimum defects.

The thickness of the dodecanethiol monolayer at the microelectrode was 10 Å, which was lower to the theoretical length. As the CV and EIS analyses indicated no electron transfer, this lower value could be due to an increase of the tilt angle of the molecules or a disturbance in their organisation. The presence of defects in the SAM formed at the microelectrode surface were due to the recessed shape of the microdisc and the possible interactions between the DDT and the SU8 photoresist.

6.5. CYSTEINE AND GLUTATHIONE SAM

Following the results proving the formation of a well defined DDT SAM at the surface of macro and microelectrode, more thiolated molecules with different function groups were investigated. The initial purpose of the microdevice fabrication and development for electroanalysis is chiral recognition. The thiolated molecules tested in this section were the chiral cysteine and chiral glutathione (Fig. 135 and Fig. 136).

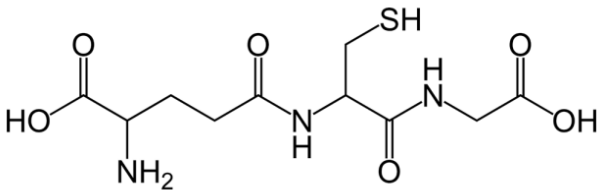

Fig. 135. Glutathione.

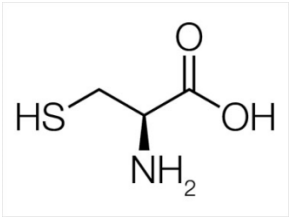

Fig. 136. Cysteine.

The spontaneous formation of self-assembled cysteine or glutathione monolayer at the surface of gold has already been studied. These molecules are of interest because of their capability to differentiate proline enantiomers (Fig. 137). The enantioselectivity of the SAMs was established using ATR-IR techniques[111,112] and the monolayer selectivity is based on preferential interactions between the molecules adsorbed at the electrode surface and the proline enantiomers in bulk solution as shown in Fig. 138. The following study looks to demonstrate this enantioselectivity using impedance spectroscopy.

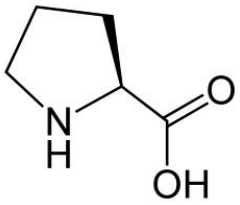

Fig. 137. Proline.

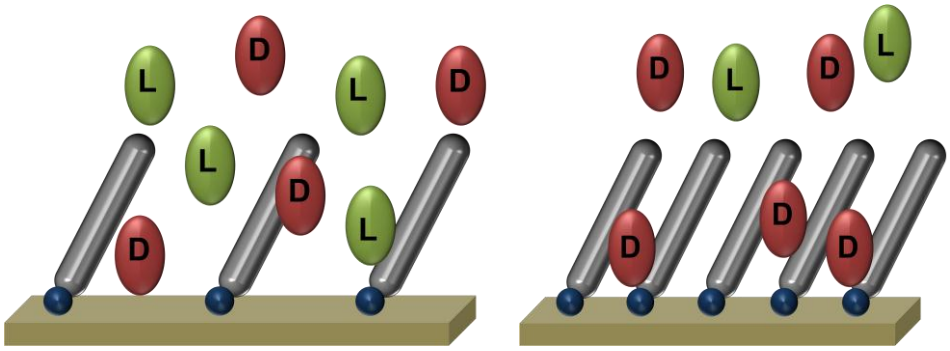

Diluted SAM with no selectivity Packed SAM with enantioselectivity

Fig. 138. Relationship between the SAM packing and the enantioselectivity.

All the cyclic voltammetry and impedance analyses related to cysteine and GSH were performed in buffer solution at pH = 6.8 in order to keep the monolayers stable. The thiol pKa value was 8.7 for GSH[150] and 9.4 for cysteine[151]. The pKa of the proline was 2.4 for the carboxylic acid group and 10.6 for the amino group[152].

The selectivity of proline enantiomer depends on its affinity with the monolayer. To be enantioselective the thiol composing the SAM must properly interact with the proline. The optimum SAM is the one which allows a maximum of interactions to take place. The organisation of the molecule at the surface of the electrode and the packing of the monolayer depend on the formation process. For the SAM formation of cysteine and GSH at the surface of gold, the main parameters influencing the resulting layer are the thiol concentration and the duration of adsorption. The smaller and shorter they are, the less dense the resulting monolayer is. Different durations of adsorption were considered in this study in order to reach the optimal packing allowing chiral selectivity.

Preliminary work consisted of examining the electroactivity of the proline molecule by CV analysis. Fig. 139 shows the CV voltammogram for proline in phosphate buffered solution (PBS) supported by a gold macroelectrode.

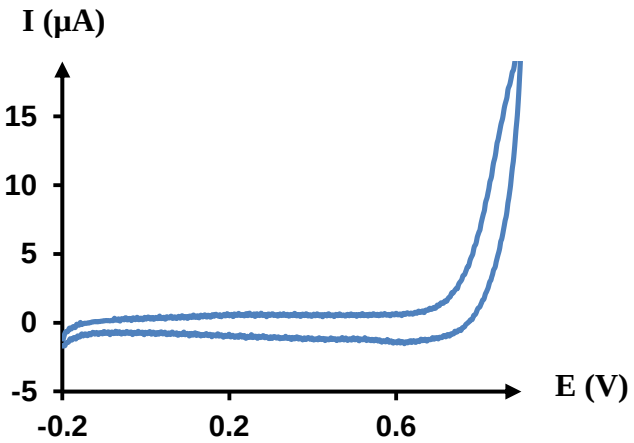

Fig. 139. CV analysis of proline in PBS solution at a gold macroelectrode with a scan rate of 100mV/s.

The flat CV response indicated the absence of electron transfer for the proline molecule within the potential window of the phosphate buffer solution.

6.5.1. Enantioselectivity at Glutathione SAM

The GSH molecule is redox active but the electron transfer at a gold electrode is a slow process that requires a high overpotential catalyst support[153]. Its electron transfer potential at a mercury drops working electrode is -0.4 V[100]. In this study the potential window considered was 0 to 0.5 V, where the GSH was inactive.

The different adsorption times considered for the SAM formation were 10 min and 16 hours. These times were chosen in order to compare the enantioselectivity at a diluted SAM (10 min) and at a well packed SAM (16 hrs). In the same manner as the dodecanethiol, the GSH molecule was not conductive and therefore a full coverage of the electrode surface was expected to prevent electron transfer. The cyclic voltammetry analyses were performed to control the occurrence of a redox reaction at the surfaces of

the modified macroelectrode. Fig. 140 and Fig. 141 show the CV responses of the modified macroelectrode for a 10 min and a 16 hours thiol deposition, on $K_3Fe(CN)_6$, in the presence of D- and L-proline. For comparison, the response of the unmodified macroelectrode on the same solution is also shown.

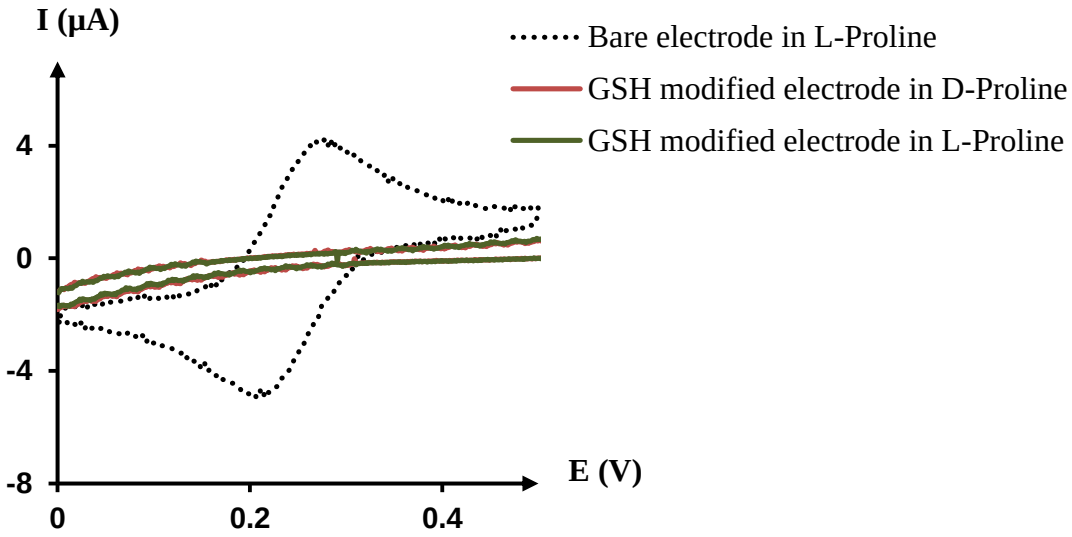

Fig. 140. CV of GSH modified (10 min) macroelectrode on $K_3Fe(CN)_6$ in the presence of proline in PBS solution.

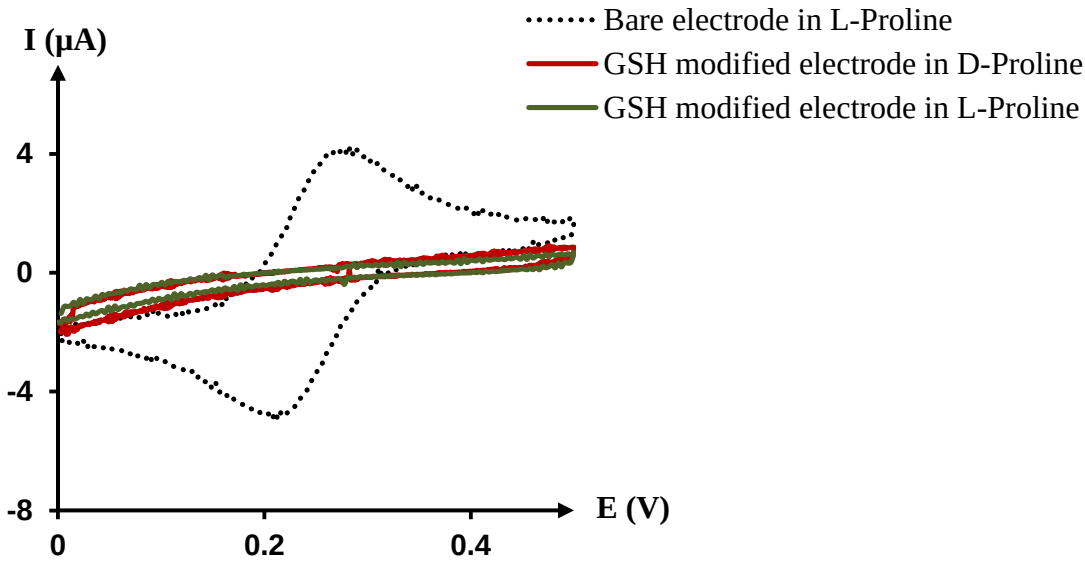

Fig. 141. CV of GSH modified (16 hrs) macroelectrode on $K_3Fe(CN)_6$ in the presence of proline in PBS solution.

In both voltammograms, the absence of peaks for the modified electrodes confirmed the complete covering of the surface, even for an adsorption time of only 10 minutes. In the absence of electron transfer the responses of the analyte in the presence of D- or L-proline were the same.

In the absence of electron transfer, impedance analysis was used to study further the structure of the SAM in the presence of proline enantiomers, for frequencies going from 100 kHz to 0.1 Hz. Fig. 142 shows the Nyquist plot of the macroelectrode at the analyte redox potential, for the GSH SAM formed in 10 min and 16 hrs and in the presence of D- and L-proline.

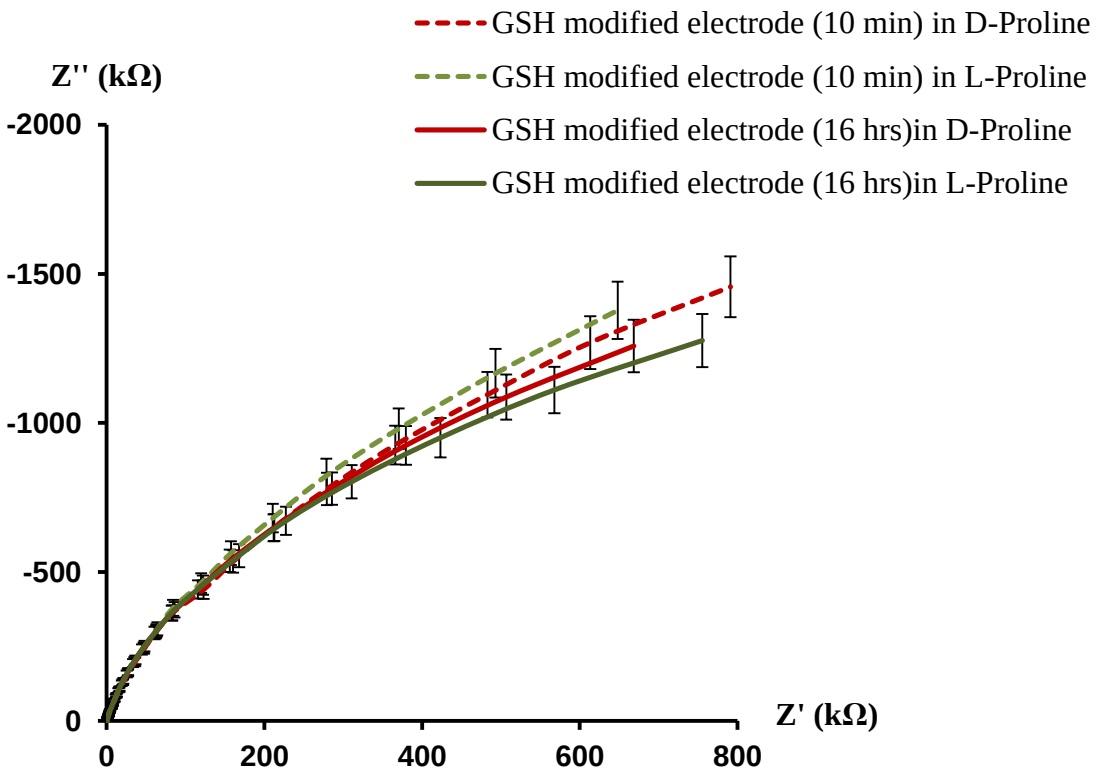

Fig. 142. Comparison of Nyquist plot for gold macroelectrode modified with GSH, during 10 min and 16 hrs, on $K_3Fe(CN)_6$ in the presence of proline in PBS solution.

The charge transfer resistances and the capacitances of the monolayers for the four different systems were accessed using equivalent circuit fitting and are presented in Table 3.

Thiol adsorption time	Proline enantiomer	R_{ct} (MΩ)	C (µF)
10 min	D	4.8	0.5
10 min	L	5	0.7
16 hrs	D	4	1
16 hrs	L	3.6	1

Table 3. Charge transfer resistance and capacitance of GSH monolayer.

The Nyquist plots of the modified electrodes all had curved shapes, comparable to a semi circle, indicating a charge transfer control as opposed to the straight line observed for a bare electrode, which was characteristic of mass transfer control. Those results corroborated the CV analyses; the charge transfer control occurrence confirmed the good electron blocking properties of the monolayer. The exact surface coverage was calculated from Eq. 41. The charge transfer resistance was 150 Ω for the bare gold macroelectrode and 4.8 MΩ, 5 MΩ, 4 MΩ and 3.6 MΩ for the GSH modified electrode. The resulting surface coverage was 0.99 for the four systems, which proved the quasi absence of pinhole or free space at the surface of the electrode already observed.

The Nyquist plots were presented with errors bars in order to point out the absence of tangible differences between the four responses. The error percentage was calculated from the reproducibility of the monolayer responses for different formation time and in the presence of (L)- or (D)-proline. It was estimated to be $\pm$7%.
The monolayer was already dense after 10 minutes of adsorption and its charge resistance and capacitance were similar to the one of a monolayer formed after 16 hours. The monolayer formation is quick and it was proven impossible to obtain a reproducible diluted monolayer permitting a partial electron transfer.

The charge transfer resistance of the monolayer was the same in the presence of L- or D-proline (Table 3). The preferential interaction between GSH and one of the enantiomers were not visible in the impedance characterisation of the SAM structure. The GSH monolayer was further studied by calculating the apparent and theoretical electron transfer rates (Table 4) following Eq. 43 and Eq. 44. The value used for the electron tunneling coefficient, β, [88,148] was 0.83 $Å^{-1}$ and the standard electron transfer rate constant at the bare electrode, K_0, for a gold electrode in $K_3Fe(CN)_6$ solution[149] was 0.031 $cm.s^{-1}$. The theoretical electron transfer rate couldn't be calculated in a straightforward manner due to the lack of information about the GSH molecular length once adsorbed at the gold surface. The thickness of the GSH monolayer was different from the molecule length mostly because the thiol anchoring group was located in the middle of the molecule (Fig. 135), but also because of the presence of other functional groups, such as amides or carboxylic acids, creating several side interactions. Burgi et al. investigated the structure of GSH SAM at a gold surface and showed structural transformation of the monolayer during its formation caused by interactions of the amide and carboxylic acid with the gold surface[107]. The complexity of the process doesn't permit accurate length estimation, although it can be accepted that the thickness of a GSH monolayer cannot exceed the size of the longest fragment of the molecule. The theoretical size of the GSH molecule was calculated using Chemdraw 3D and was 15 Å. The adsorbed molecule can be represented as schemed in Fig. 143. The fragment length considered for the experimental K_{app} calculation was 10 Å.

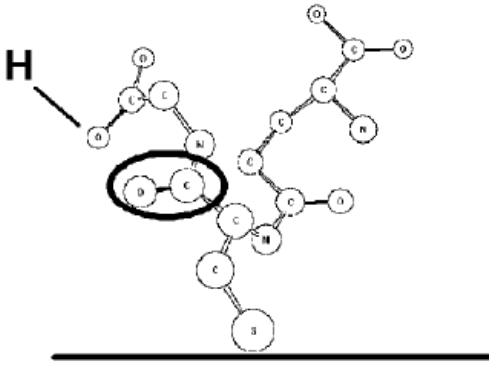

Fig. 143. Schematic representation of the adsorbed GSH molecule at gold surface[107].

R_{ct} (Ohm)	Theoretical K_{app} ($cm.s^{-1}$)	Experimental K_{app} ($cm.s^{-1}$)
4×10^{6}	7.7×10^{-6}	3.3×10^{-6}

Table 4. Theoretical K_{app} and experimental K_{app} calculations for a GSH modified electrode.

The experimental value of the apparent electron transfer rate was in agreement with the theoretical one. The experimental thickness of the monolayer calculated from the theoretical K_{app} was equal to 11 Å. This thickness was comparable to the estimated length of the fragment of the GSH molecule, which confirmed the formation a single monolayer.

6.5.2. Enantioselectivity at Cysteine SAM

The next molecule to be considered to modify the gold surface of the electrode was cysteine, which has also been reported as chirally selective toward proline enantiomers[112]. As explained previously different adsorption times were considered in order to compare the selectivity of a diluted cysteine monolayer (15 min) and at a well packed monolayer (24 hrs). CV analyses were performed to control the occurrence of a redox reaction at the surfaces of the modified macroelectrode. Fig. 144 and Fig. 145 show the CV responses of the modified macroelectrode for a 15 min and a 24 hours thiol deposition, on $K_3Fe(CN)_6$, in the presence of D- and L-proline. For comparison, the response of the unmodified macroelectrode on the same solution is also shown.

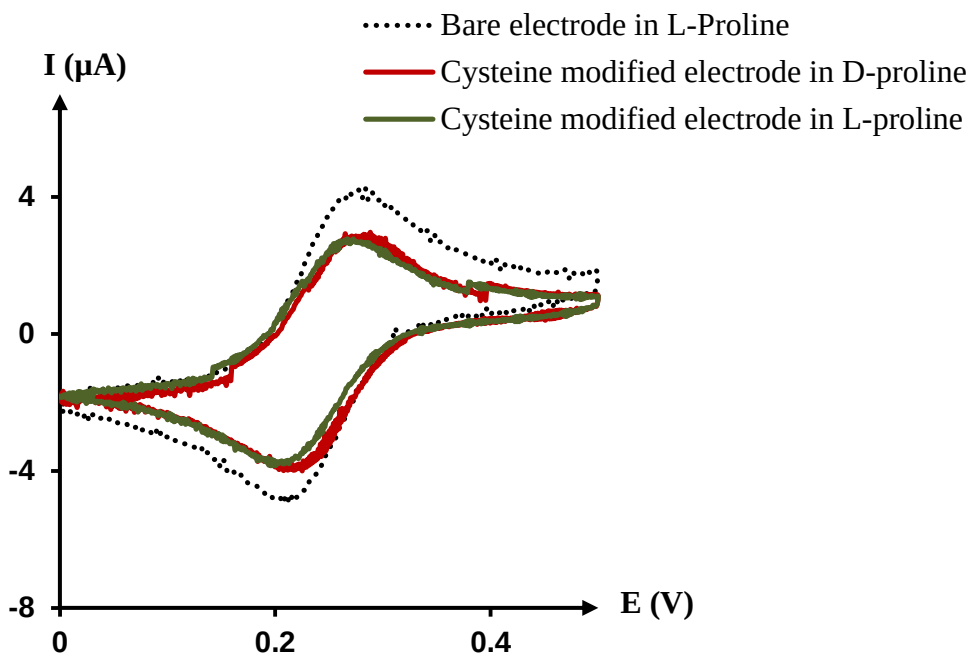

Fig. 144. CV of cysteine modified (15 min) macroelectrode on $K_3Fe(CN)_6$ in the presence of proline in PBS solution.

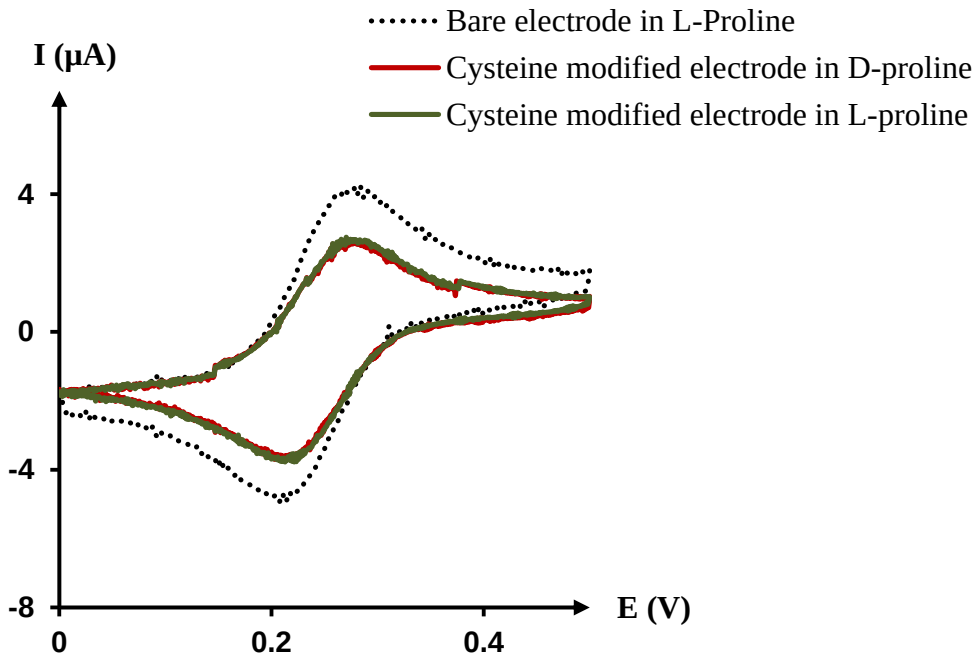

Fig. 145. CV of cysteine modified (24 hrs) macroelectrode on $K_3Fe(CN)_6$ in the presence of proline in PBS solution.

The voltammograms exhibited a reversible wave at 0.3 V characteristic of the electron transfer of ferricyanide. The cysteine SAMs formed after 15 minutes or 24 hours did not prevent the electron transfer to take place, show that the electrode surfaces were not fully modified. The oxidation peak intensity was 4 µA at the unmodified electrode and 2.25 µA at the cysteine modified electrode, i.e. 56 % of the full intensity. The responses of the modified electrodes were the same whether they were in the presence of L- or D-proline.

The structure of the SAM was studied further using impedance spectroscopy for frequencies going from 100 kHz to 0.1 Hz. Fig. 146 and Fig. 147 show the Nyquist plots of the electrode modified during 15 min and 24 hrs, in the presence of L- and D-proline. Both measurements were performed at the analyte redox potential. The plots were presented with errors bars in order to point out the reproducible differences between the four systems. The percentage of error was ±7%; it was estimated from reproducibility of the measurements.

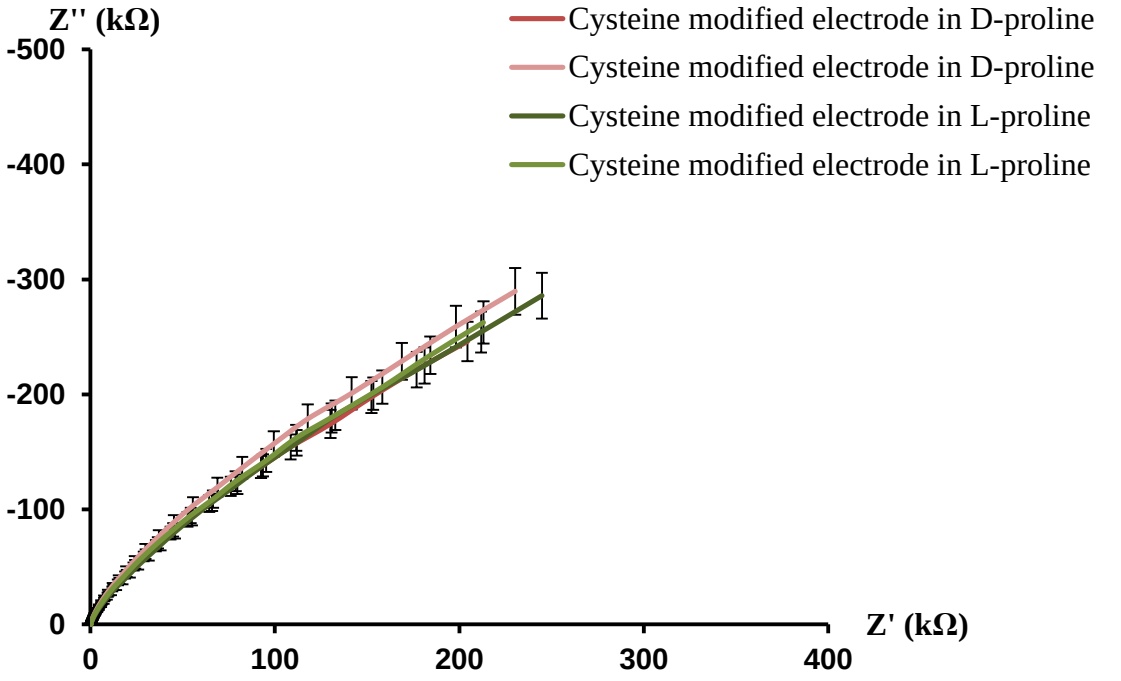

Fig. 146. Nyquist plot for gold macroelectrode modified with cysteine (15 min) on $K_3Fe(CN)_6$ in the presence of Proline in PBS solution.

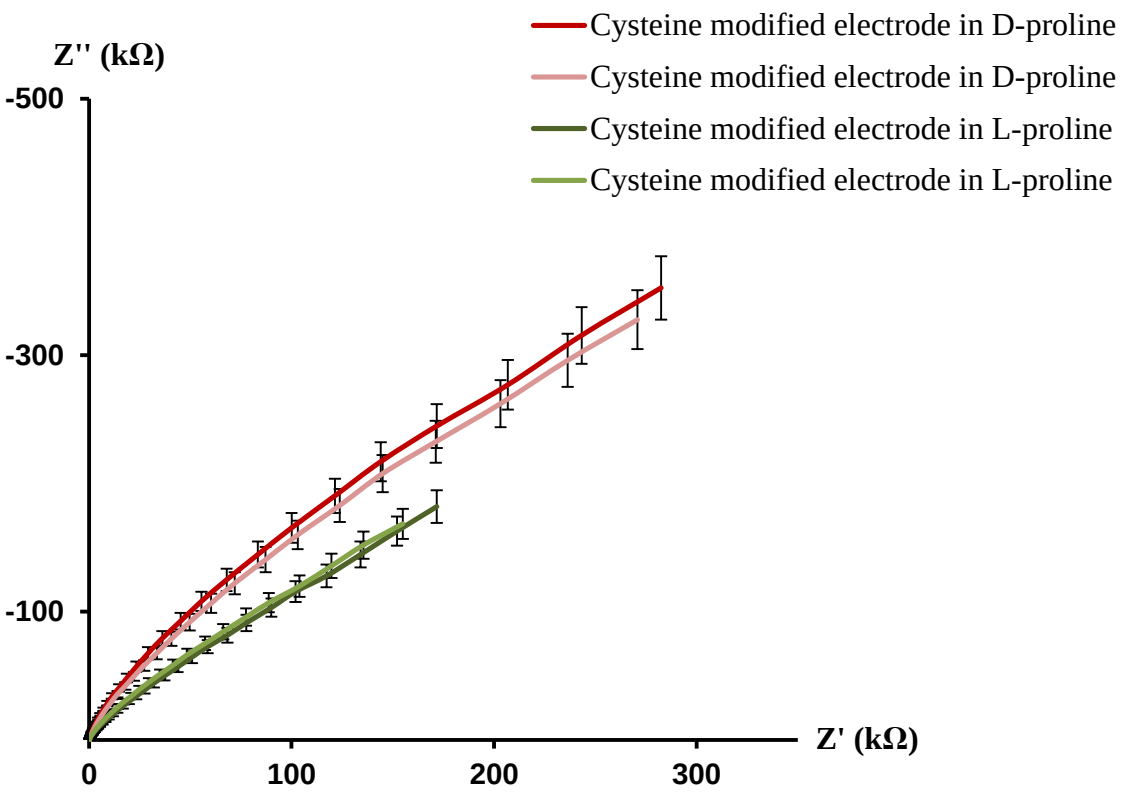

Fig. 147. Nyquist plot for gold macroelectrode modified with cysteine (24 hrs) on $K_3Fe(CN)_6$ in the presence of Proline in PBS solution.

All the Nyquist plots had the same shape consisting of a curved part in the high frequencies and a straight line part in the low frequencies, characterising the kinetic control of the electron and the mass transfer respectively. The large presence of mass transfer control corroborate with the CV analysis showing the occurrence of electron transfer. The charge transfer resistances and the capacitances of the monolayers were calculated by fitting an equivalent electronic circuit which had a Warburg element added to represent the diffusion through the monolayer. The values for the four different systems are presented in Table 5.

Thiol adsorption time	Proline enantiomer	R_{ct} (kΩ)	C (μF)
15 min	D	140	2.1
15 min	L	140	1.9
24 hrs	D	140	1.55
24 hrs	L	65	2.5

Table 5. Charge transfer resistance and capacitance of GSH monolayer.

CV and EIS analyses both showed that the electrodes were not fully covered with cysteine and that electron transfer was still taking place at their surface. The surface coverage value (Eq. 41) was 0.99 for the four systems indicating that most of the electrode surface was modified.

Fig. 146 shows that the responses of the monolayer formed after 15 min in the presence of D- or L-proline were similar. However, the cysteine monolayer formed after 24 hours gave different responses whether it was in the presence of the D- or the L- proline enantiomer (Fig. 147). The electron transfer rate at each monolayer was calculated following Eq. 43 and Eq. 44 (Table 6). The value used for the electron tunneling coefficient, β, [88,148] was 0.83 $Å^{-1}$ and the standard electron transfer rate constant at the bare electrode, K_0, for a gold electrode in $K_3Fe(CN)_6$ solution[149] was 0.031 $cm.s^{-1}$. The surface area of the macroelectrode was 2 mm^2. No studies were found concerning the structure of cysteine monolayer and the relation between the molecule size and the monolayer thickness. The length of the cysteine molecule was calculated from the software Chemdraw 3D and estimated to be 5 Å.

Adsorption time	Enantiomer	R_{ct} (kOhm)	Theoretical K_{app} ($cm.s^{-1}$)	Experimental K_{app} ($cm.s^{-1}$)	Experimental thickness (Å)
15 min	D-proline	140	4.9×10^{-4}	9.5×10^{-5}	7
	L-proline	140	4.9×10^{-4}	9.5×10^{-5}	7
24 hrs	D-proline	140	4.9×10^{-4}	9.5×10^{-5}	7
	L-proline	65	4.9×10^{-4}	2.0×10^{-4}	6

Table 6. Theoretical K_{app} and experimental K_{app} calculations for a cysteine modified electrode.

The experimental rates of electron transfer were 9.5×10^{-5} $cm.s^{-1}$ for the cysteine monolayer formed after 15 min in the presence of L- or D-proline and for the monolayer formed after 24 hrs in the presence of D-proline. The electron transfer rate at the monolayer formed in 24 hrs in the presence of L-proline was 2.0×10^{-4} $cm.s^{-1}$, which was in agreement with the theoretical electron rate transfer.

The identical values of the electron transfer rates at the monolayer formed in 15 min in the presence of D- and L-proline showed that there was no selective penetration of the proline enantiomer through the SAM. Those values were slightly lower than the theoretical electron transfer rate indicating that the resulting monolayer was denser as both D- and L- enantiomers could penetrate it. This phenomenon is represented in a simplified scheme in Fig. 148.

The electron transfer rates at the cysteine SAM formed in 24 hrs was smaller in the presence of D-proline than it was in the presence of L-proline. This showed that the density of the monolayer was higher in the presence of D-proline than it was with L-proline. The increase of the density was due to the penetration of the D-proline into the cysteine SAM. The monolayer formed after 24 hrs had a different structure than the one formed in 15 min and allowed selective interactions to take place between the cysteine and the D-proline. The higher electron transfer rate obtained in the presence of L-proline indicated that the enantiomer could not infiltrate the monolayer, whose density was therefore lower. This phenomenon is illustrated in a simplified scheme in Fig. 148.

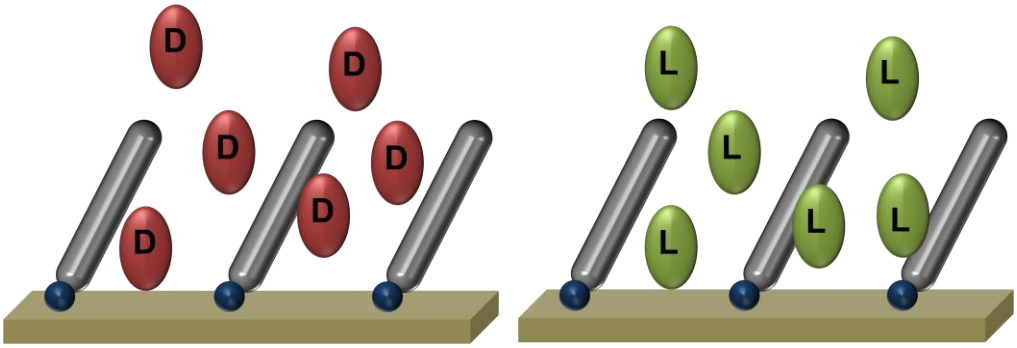

15 min cysteine SAM in the presence of D-proline (red) or L-proline (green)

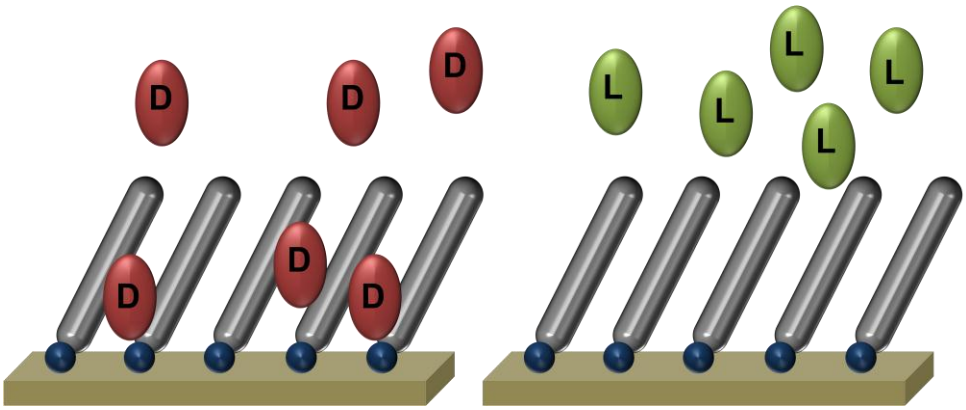

24 hrs cysteine SAM in the presence of D-proline (red) or L-proline (green)

Fig. 148. Proline selectivity at cysteine monolayer.

In all 4 cases the experimental electron transfer rates were slightly inferior to the theoretical ones. Those differences were reflected in the experimental average thickness calculations and the four monolayers formed were thicker than the cysteine molecule size. The average thickness of the cysteine monolayer formed after 24 hrs was 7 Å when tested in the presence of D-proline and 6 Å when tested in the presence of L-proline.

The differences between the electron transfer rates, and therefore differences of density and average layer thickness, illustrated the preferential interactions happening between the cysteine molecule and the D-proline enantiomers. It was showed that investigating the SAM structure using impedance spectroscopy could allow the identification of enantioselectivity.

6.6. DNA SAM

The last molecule to be considered to modify the gold surface was a thiolated single-stranded DNA. DNA is composed of nucleotide base units coordinated via a phosphate deoxyribose backbone. The four bases composing DNA are guanine (G), adenine (A), thymine (T) and cytosine (C) (Fig. 149). The oligonucleotide molecules are defined by the arrangement of the bases.

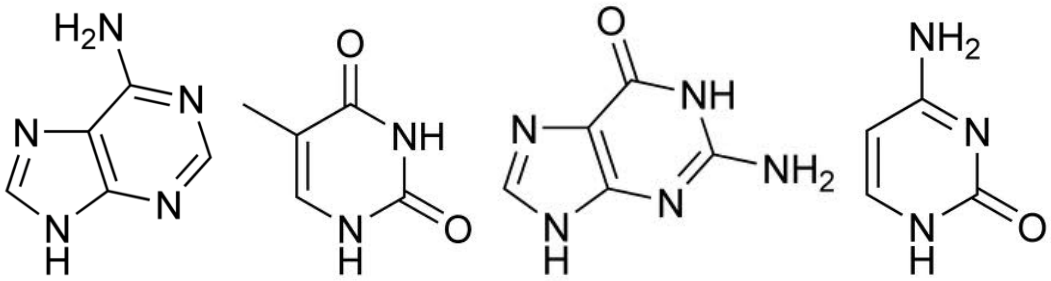

Adenine Thymine Guanine Cytosine

Fig. 149. Oligonucleotides bases.

The sequence of the molecule studied in this work was defined as follows:
5'-GGGAGTCAAGAACGAA$(CH_2)_3$SH-3'

6.6.1. DNA Monolayer on Gold Macroelectrode

Previous studies using the same molecule[154] recommended an immobilisation time of 24 hours for a concentration of oligonucleotides of 0.1 mmol/L. The DNA used for this study was supplied with a concentration of 0.04 mmol/L. To compensate for this low concentration, longer immersion times were also investigated and compared to the effect of a 24 hours immersion.

The monolayer was tested in the presence of the standard ferricyanide analyte and in the presence of methylene blue (Fig. 150). The methylene blue analyte is of interest in this study as it is known to interact with DNA and is commonly used to trace or functionalise adsorbed molecules at the electrode surface[155,156].

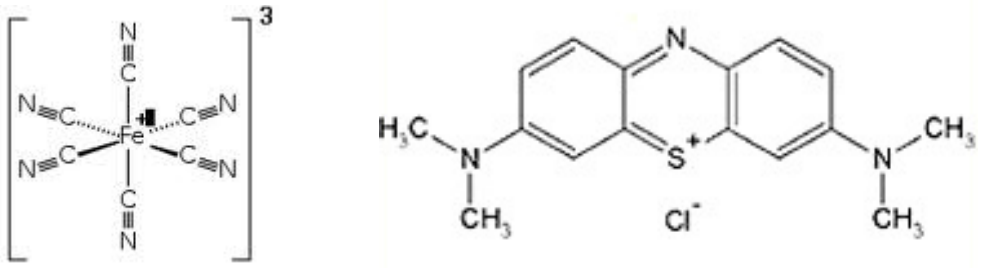

Ferricyanide Methylene Blue

Fig. 150. Analytes.

$K_3[Fe(CN)_6]$ analyte at DNA modified electrode

The first electroanalyses at the DNA modified electrode were performed in the presence of $K_3Fe(CN)_6$. Fig. 151 shows the CV responses of the modified macroelectrode for a 24 and a 48 hours DNA deposition. For comparison, the response of the unmodified macroelectrode on the same solution is also shown.

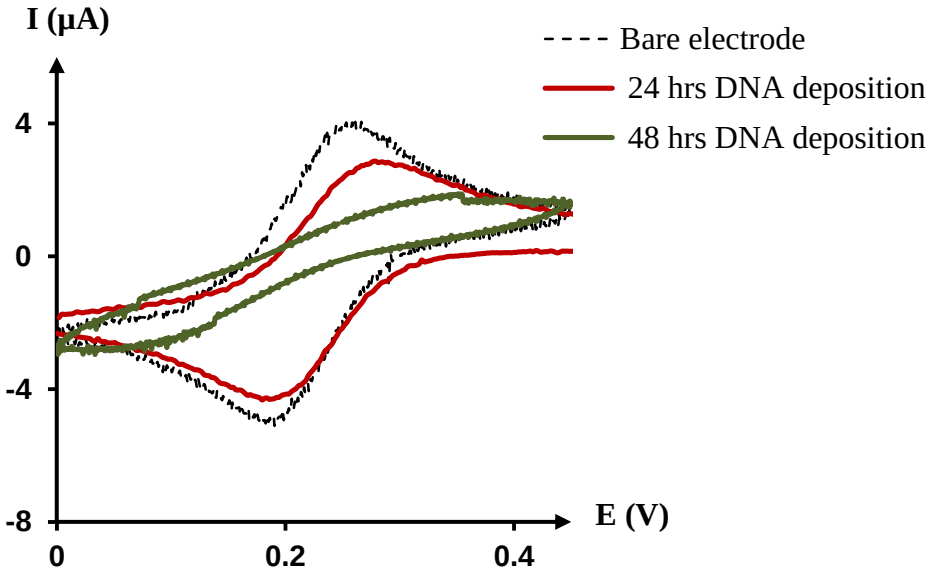

Fig. 151. CV of gold macroelectrode modified with DNA during 24 and 48 hrs on $K_3Fe(CN)_6$ in PBS solution containing NaCl.

The voltammograms exhibited a reversible wave around 0.25 V characteristic of the electron transfer of ferricyanide. The amplitudes of the peaks obtained using the modified electrodes were inferior to the one using the unmodified electrode in the same conditions. This reduction indicated an obstruction of the surface and a partial DNA covering of the electrode. The oxidation peak intensity of the unmodified electrode was 4 µA. After DNA surface modification this peak intensity was reduced to 2.86 µA for a 24 hours treatment and 1.85 µA for a 48 hours treatment. Increasing the time of surface modification limited the electron transfer further but did not prevent it entirely: 70% of the current was going through the monolayer after 24 hours and 46% after 48 hours. Leaving the electrode immersed for longer periods didn't improve the blocking properties of the layer much further and remaining electron transfer was happening. Moreover the quality of the SAM was irreproducible over long immersion times in thiol, as parallel interactions between the molecules compete with the adsorption process.

The adsorption of the ferricyanide ions at the DNA monolayer was studied by examining the relation between the current of the oxidation peak and the square root of the scan rate. When the ferricyanide analyte is freely diffused in solution and not adsorbed at the electrode surface, the anodic peak increases proportionally to $\sqrt{v}$ following the Randles-Sevcik equation (Eq. 5) where $I_{pa} = (2.69 \times 10^5) z^{3/2} C A D^{1/2} v^{1/2}$. In the case of adsorption of the analyte at the surface of the electrode the peak intensities are directly proportional to the scan rate. CV analyses were run at different scan rates between 5 and 200 mV/s and the relation between the oxidation peak current and the square root of the scan rate is showed in Fig. 152.

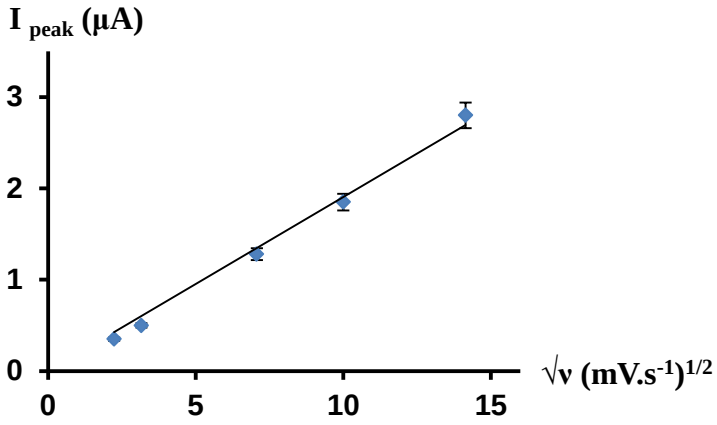

Fig. 152. Relation between $\sqrt{\nu}$ and I_{peak} at a DNA modified electrode, on $K_3Fe(CN)_6$ in PBS solution containing NaCl.

The anodic peak current appeared to increase linearly with $\sqrt{\nu}$ indicating that the analyte was accessing the metal surface of the electrode without being absorbed.

The monolayer was studied further using impedance spectroscopy for frequencies going from 100 kHz to 0.1 Hz. Fig. 153 and Fig. 154 show the Nyquist plots of the electrode modified during 24 and 48 hrs. Both measurements were performed at the analyte redox potential.

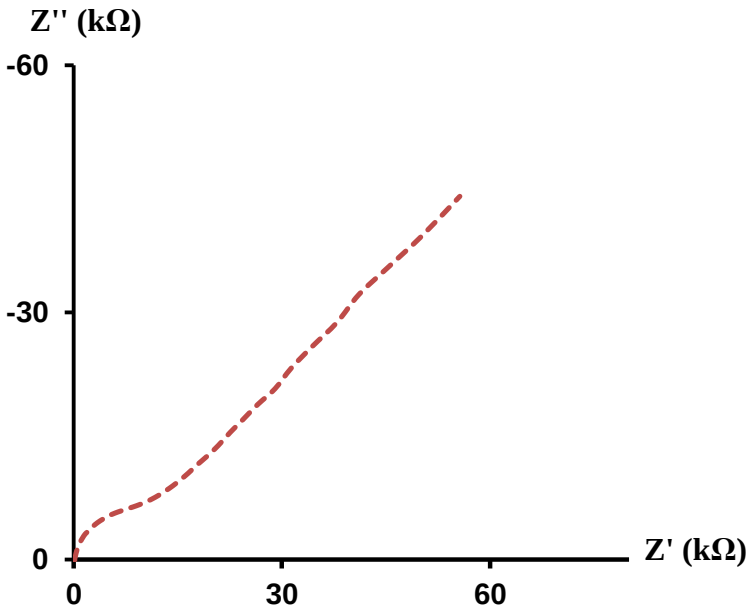

Fig. 153. Nyquist plot of gold macroelectrode modified with DNA for 24 hrs, on $K_3Fe(CN)_6$ in PBS solution containing NaCl.

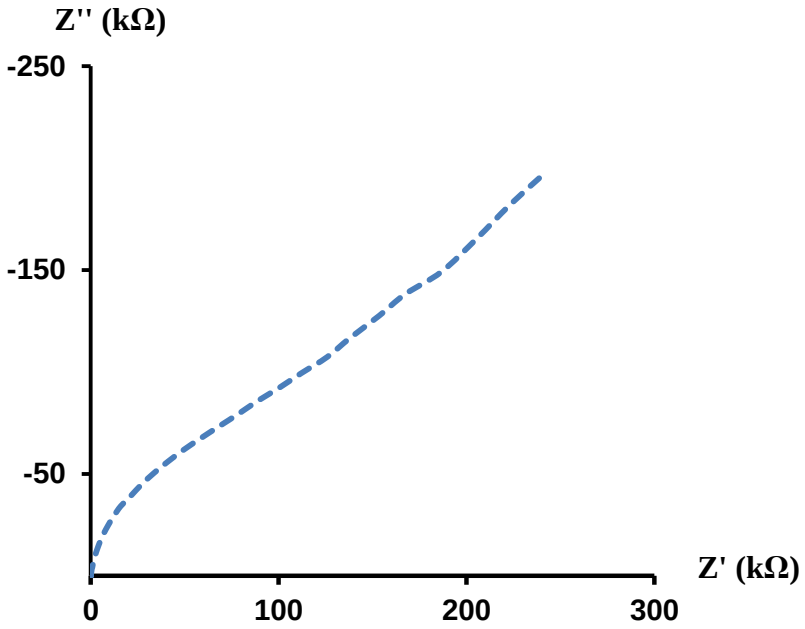

Fig. 154. Nyquist plot of gold macroelectrode modified with DNA for 48 hrs, on $K_3Fe(CN)_6$ in PBS solution containing NaCl.

The Nyquist plots for both the electrode modified after 24 and 48 hours showed that the process happening at the interface was partially charge transfer controlled (curved part of the plot) and mass transfer controlled (straight line part of the plot). Fitting with equivalent circuits gave a charge transfer resistance of 14 kΩ for the 24 hrs monolayer and 150 kΩ for the 48 hrs monolayer. The capacitance was 0.4 μF for the 24 hrs monolayer and 1.2 μF for the 48 hrs one. The charge transfer resistance of the monolayer formed after 48 hrs was higher than the one formed after 24 hrs only which corroborated with the CV analyses previously presented. The layer formed after 48 hrs was more packed and prevented more electron transfer.

Further impedance discussions and calculations of the theoretical electron transfer rates implied knowing the theoretical length of the DNA molecule and its tunneling coefficient. Such values could not be found in the literature where the complexity of oligonucleotides molecules limited the electroanalytical study of the DNA monolayer[157] or imposed the use of approximations[115]. The oligonuleotides used in this study consisted of 16 bases. The length of a base unit is 3.3 Å long[158], bringing the total length of the molecule to 53 Å. The electron tunneling coefficient depends on the structure of the

molecule. The backbone of the DNA was composed of phosphate deoxiribo groups (Fig. 155). The presence of heteroelements such as oxygen and phosphorus lowered the electron tunneling coefficient in comparison to the coefficient of alkyl chains. The β value used in the following calculations was the one of methylene equal to 0.67 $Å^{-1}$ [88].

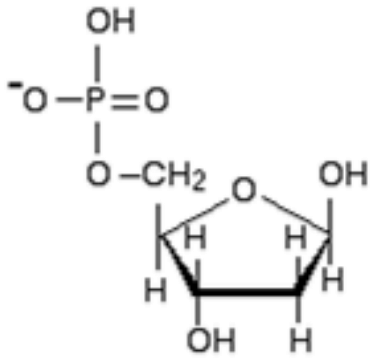

Fig. 155. DNA backbone structure.

The theoretical and experimental electron transfer rates were calculated for the 24 and 48 hrs monolayers using Eq. 43 and Eq. 44. The experimental average thickness of the film was calculated from those values (Table 7). The standard electron transfer rate constant at the bare electrode, K_0, for a gold electrode in $K_3Fe(CN)_6$ solution[149] was 0.031 $cm.s^{-1}$. The surface area of the macroelectrode was 2 mm^2.

Adsorption time	**R_{ct} (kOhm)**	**Theoretical K_{app} ($cm.s^{-1}$)**	**Experimental K_{app} ($cm.s^{-1}$)**	**Experimental thickness (Å)**
24 hrs	14	1.17×10^{-17}	9.5×10^{-4}	5.2
48 hrs	150	1.17×10^{-17}	8.9×10^{-5}	8.7

Table 7. Theoretical and experimental K_{app} calculations for a DNA modified electrode in the presence of ferricyanide.

As expected, the electron transfer rate decreased for longer adsorption time indicating an increase of the monolayer density at the electrode surface. The associated average thicknesses for those apparent electron transfer rate values were lower than 10 Å which

was not in agreement with the theoretical 53 Å. The large differences between the theoretical and experimental monolayer thickness indicated that not only the DNA molecules were not properly organised but they were also lying at the electrode surface as schemed in Fig. 156. This phenomenon is commonly noticed in DNA surface modification. Even though the experimental values did not fit the theory, they were in agreement with the literature, where the charge transfer resistances measured at DNA monolayers are in the range of kΩ [115,159].

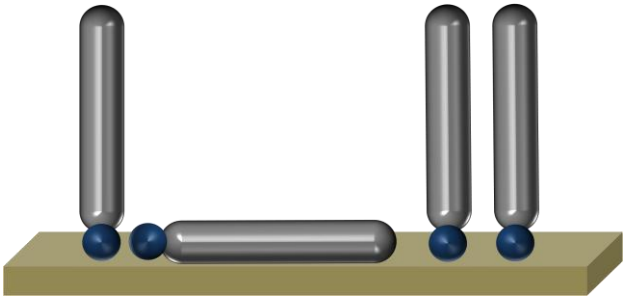

Fig. 156. Thiolated DNA monolayer at gold surface.

The surface of electrode could be modified but the DNA molecule were not properly organised and the resulting thickness of the monolayer was lower than the molecule length.

Methylene blue analyte at the DNA modified electrode

The DNA monolayer was also tested in the presence of methylene blue. The same analyses as for the ferricyanide were performed, starting with CV at different scan rates in order to identify if there was an electron transfer occurring at the electrode and, if so, if the methylene blue was adsorbed or not at the DNA monolayer. Fig. 157 shows the CV responses of the DNA modified macroelectrode for a 48 hours deposition. For comparison, the response of the unmodified macroelectrode on the same solution is also shown.

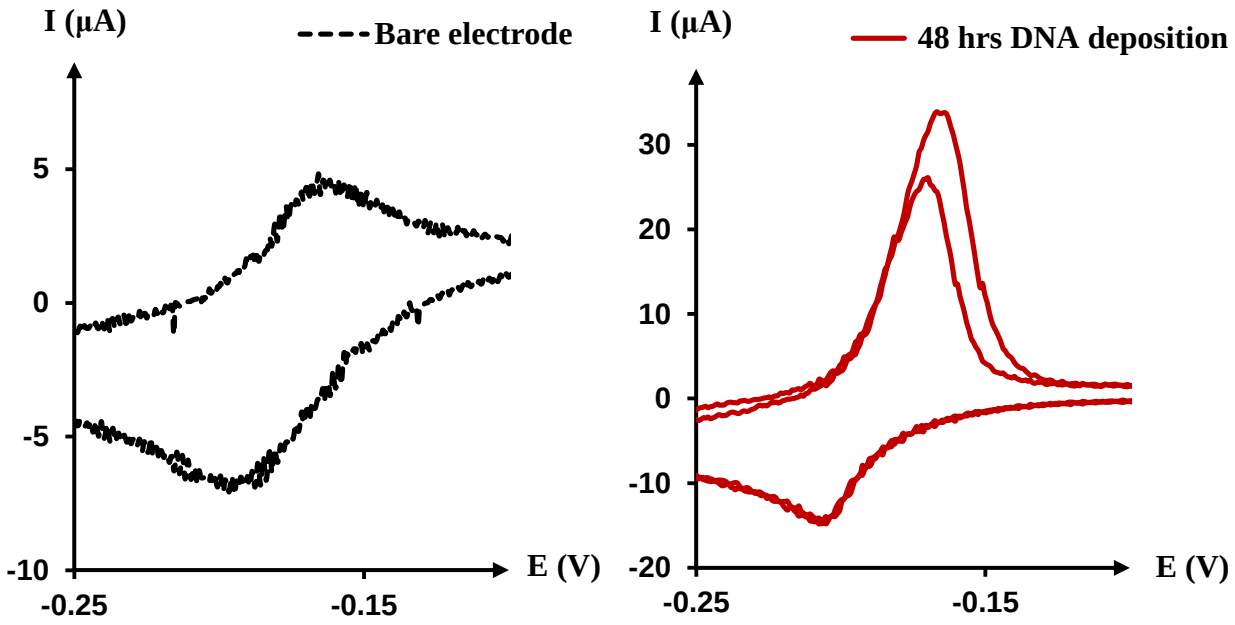

Fig. 157. CV of gold macroelectrode modified with DNA during 48 hrs on methylene blue in PBS solution containing NaCl.

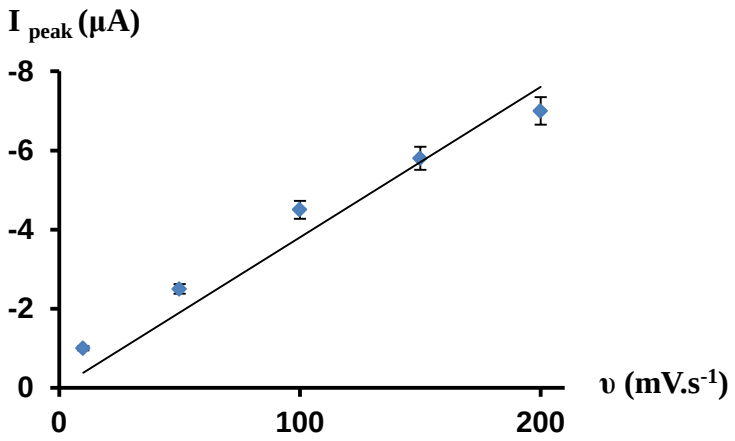

Fig. 158. Relation between ν and I_{peak} at a DNA modified electrode, in the presence of methylene blue in PBS solution containing NaCl.

The voltammograms exhibited a reversible wave around -0.17 V characteristic of the electron transfer of methylene blue. The amplitude of the peak obtained using the modified electrode was amplified and rather unstable through the cycles. The peak intensities were directly proportional to the scan rate as shown in Fig. 158, which characterised the adsorption of the methylene blue at the DNA surface. This adsorption is

described in the literature as a result of intercalation between the methylene blue and the bases of the DNA that are close to the bulk solution[102,156].

The monolayer was studied further using impedance spectroscopy for frequencies going from 100 kHz to 0.1 Hz. Fig.46 shows the Nyquist plots of the electrode modified during 48 hrs and performed at the analyte redox potential.

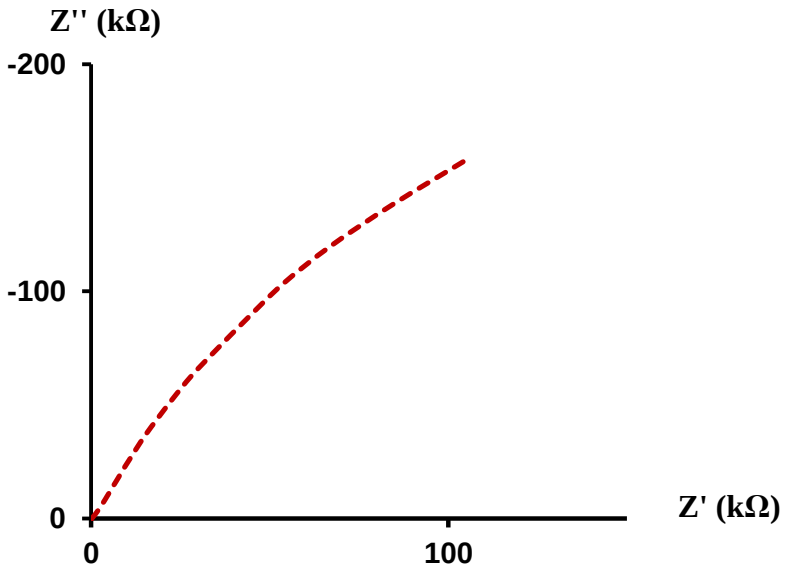

Fig. 159. Nyquist plot of gold macroelectrode modified with DNA during 48 hrs, on methylene blue in PBS solution containing NaCl.

Fitting the equivalent circuit gave values of the charge transfer resistance of the DNA monolayer in the presence of methylene blue as 700 kΩ, and the capacitance as 7 μF. The theoretical and experimental electron transfer rates were calculated from the charge transfer resistance using Eq. 43 and Eq. 44 (Table 8). The experimental average thickness of the film was calculated from them. The standard electron transfer rate constant at the bare electrode, K_0, for a gold electrode in methylene blue solution[155] was 0.07 cm.s^{-1}.

Adsorption time	R_{ct} (kOhm)	Theoretical K_{app} ($cm.s^{-1}$)	Experimental K_{app} ($cm.s^{-1}$)	Experimental thickness (Å)
48 hrs	700	2.65×10^{-17}	1.90×10^{-5}	12.3

Table 8. Theoretical and experimental K_{app} calculations
for a DNA modified electrode in the presence of methylene blue.

Similar to the analyses performed in ferricyanide, the experimental K_{app} was not in agreement with the theory. The average thickness of the DNA layer was much lower than the length of the molecule, corroborating the assumption that the DNA was poorly organised and some were lying at the surface of the electrode.

6.6.2. DNA Monolayer on Microelectrode Array

The DNA surface modification of the microelectrode array was also investigated in order to broaden the field of application of the microdevice presented in Chapter 4.
After a 48 hours immersion in DNA solution, the modified microarray was tested on a ferricyanide solution. Fig. 160 shows the responses of the unmodified and of the DNA-modified microelectrode array.

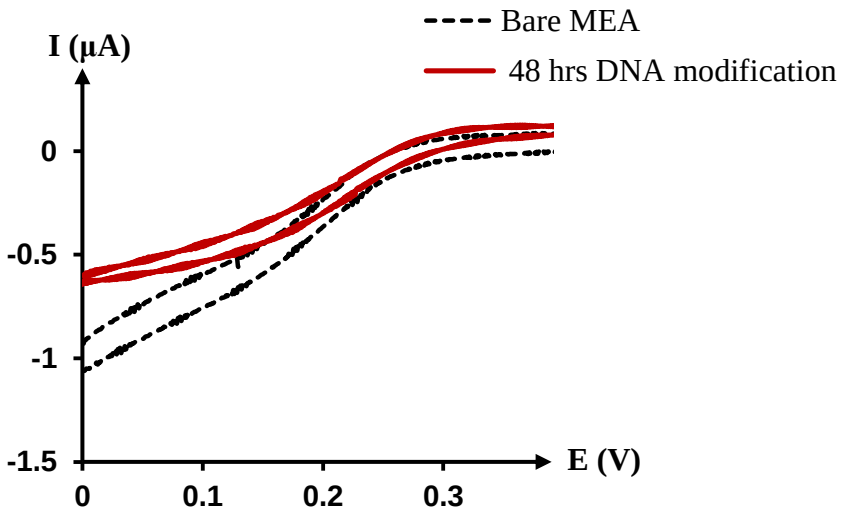

Fig. 160. CV of MEA modified with DNA during 48 hrs on $K_3Fe(CN)_6$
in PBS solution containing NaCl.

The voltammograms exhibited a reversible sigmoidal wave at 0.25 V, characteristic of the electron transfer of ferricyanide. The steady state current was 0.6 μA, i.e. 60% of the total current at the unmodified MEA. The reduction of the peak amplitude confirmed the occurrence of DNA modification and the partial obstruction to the electron transfer.

The monolayer was also defined using EIS for frequencies going from 100 kHz to 0.1 Hz. Fig. 161 shows the Nyquist plots of the electrode modified during 48 hrs and performed at the analyte redox potential.

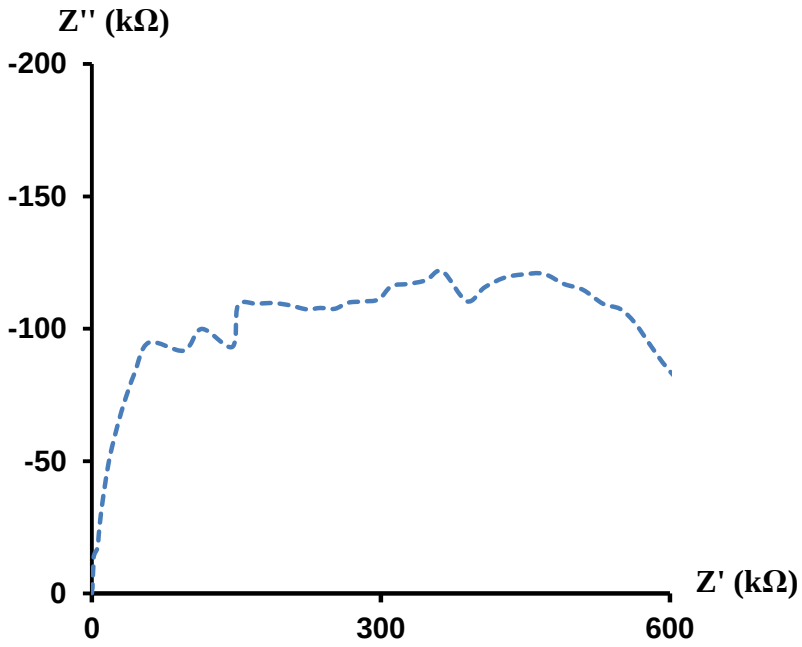

Fig. 161. Nyquist plot of MEA modified with DNA during 48 hrs, on $K_3Fe(CN)_6$ in PBS solution containing NaCl.

Although the measurements were very sensitive to external perturbations, which resulted in the presence of noise and experimental artefacts, the semi-circular shape of the response was clear and confirmed the electron transfer control. The charge transfer resistance measured at the DNA modified MEA was 400 kΩ and the capacitance was 0.04 μF.

In an attempt to complete the modification and increase the surface coverage of the electrodes, the microelectrode array was modified again with DDT. The total surface treatment consisted of 48 hours in DNA followed by 24 hours in DDT. The CV analyses of the resulting monolayer are showed in Fig. 162.

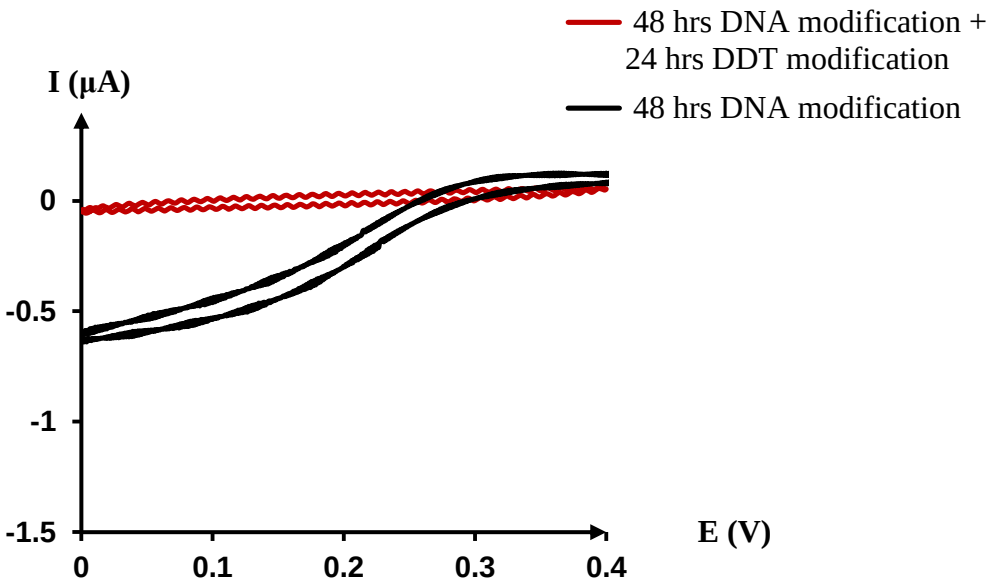

Fig. 162. CV of modified MEA on $K_3Fe(CN)_6$ in PBS solution containing NaCl.

The surface of the microelectrode array proved to be fully covered showing that the DNA pinholes could be filled with DDT molecules.

The monolayer was also analysed by EIS for frequencies going from 100 kHz to 0.1 Hz and performed at the analyte redox potential (Fig. 163).

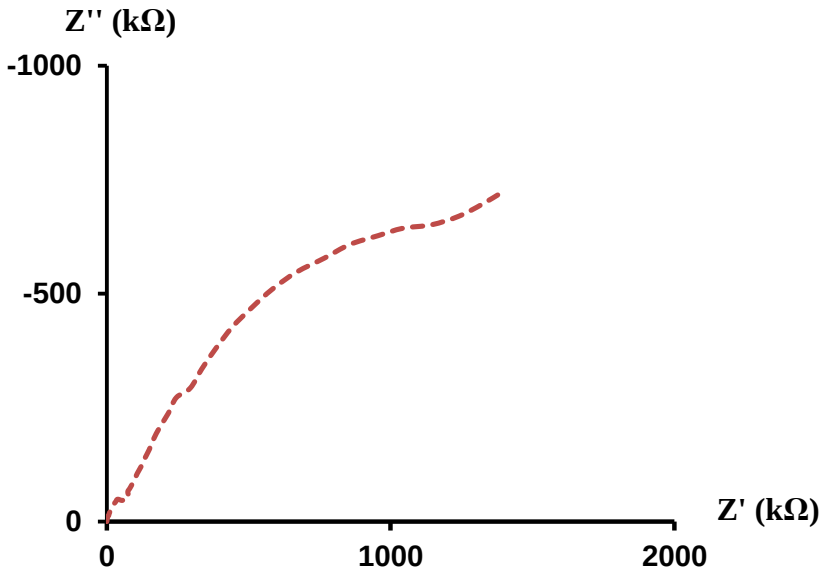

Fig. 163. Nyquist plot of MEA modified with DNA during 48 hrs and with DDT during 24 hrs on $K_3Fe(CN)_6$ in PBS solution containing NaCl.

The round Nyquist plot shape confirmed the dominance of the electron transfer control. The resulting charge transfer resistance after extra DDT modification was increased from 400 to 1500 kΩ and the capacitance went from 0.04 µF to 0.5 µF.

Modification	**R_{ct} (kOhm)**	**Theoretical K_{app} (cm.s^{-1})**	**Experimental K_{app} (cm.s^{-1})**	**Experimental thickness (Å)**
DNA	400	1.17×10^{-17}	1.70×10^{-4}	8
DNA + DDT	1500	1.70×10^{-19}	4.55×10^{-5}	8.8

Table 9. Theoretical and experimental and K_{app} calculations for a DNA modified electrode in the presence of methylene blue.

The decrease of the electron transfer rate after the additional DDT modification corroborated the increase of the surface coverage.

6.7. CONCLUSION

The surface of the microelectrode array was modified successfully with DDT. The cyclic voltammetry and impedance spetroscopy analyses showed full coverage of the surface. The preliminary analyses comparing the bare microelectrode array to the bare macroelectrode indicated that the resistance and capacitance at the microelectrode diffusion layer were not directly proportional to the surface area as for the macroelectrode. Side effects due to the drastic reduction of the electrode scale competed and altered the direct relation between the resistance (or capacitance) and the electrode surface area.

The impedance analyses of the glutathione modified electrode did not allow the measurement of selective interactions between the monolayer and proline enantiomers. The duration of GSH adsorption did not affect much the final resistance and capacitance of the monolayer. On the other hand, the presence of proline enantiomer affected the impedance responses of the cysteine modified electrode. The charge transfer resistance of the monolayer in the presence of L-proline was doubled in the presence of D-proline. The electron transfer rate was 9.50×10^{-5} cm.s^{-1} for D-proline and 2×10^{-4} cm.s^{-1} for L-proline. This increase confirmed the presence of preferential interactions between cysteine and the D-proline enantiomer and proved the possibility to characterise them using EIS.

Single-stranded DNA was immobilised at the surface of the macro and micro electrodes. CV and EIS analyses performed on ferricyanide showed partial coverage of the electrode surface with a rough organisation of the molecule. The monolayer at the macroelectrode had an electron transfer rate of 8.90×10^{-5} cm.s^{-1} instead of a theoretical 1.17×10^{-17} cm.s^{-1}. Analyses on methylene blue showed the characteristic immobilisation of the analyte at the DNA monolayer. The current measured at the modified electrode was directly proportional to the scan rate, and the electron transfer rate was slower (1.90×10^{-5} cm.s^{-1}).

The MEA was successfully modified with DNA and the incomplete surface coverage of the electrodes could be corrected by an additional DDT modification. The CV analyses confirmed the surface was fully covered and the electron transfer was totally prevented. The impedance study showed a decrease of the electron transfer rate from 1.70×10^{-4} cm.s^{-1} to 4.55×10^{-5} cm.s^{-1}.

7. General Conclusion

The aim of this project was to produce microelectrode arrays for industrial, biological and pharmaceutical applications, using electroanalytical techniques. In particular**,** chiral sensing was investigated with the chiral agent being in bulk solution or immobilised at the surface of the electrode. A list of publications, posters, talks, conferences attended, prizes and memberships resulting from this work is presented in Appendix 1.

7.1. Microelectrode Array

An array of 306 gold recessed microelectrodes (45 µm diameter) was fabricated using photolithography, metallisation and oxygen plasma treatment processes. The fabrication of the microdevice proved to be robust and reproducible. Using gold for working, pseudo reference and counter electrodes permitted the simplification of the fabrication process while remaining stable for electroanalysis. The well behaved nature of the microelectrode array was established by CV analysis where the responses of the microelelectrodes were in accordance with the theory, with a steady state current and no dependence on the scan rates. The influence of the method of fabrication on the final response of the electrode was established and the electro-activity of the electrode could be enhanced, while maintaining the microelectrode properties, by increasing the surface roughness of the electrodes. The increase of roughness was achieved by choosing electroplating over e-beam metallisation during the fabrication process. For an increase of the active surface of 18.6% the limited current measured was 33% higher. Nevertheless, the roughness increase had to be maintained low in order to not alter the spherical shapes of the diffusion layers of the microelectrodes. When combined with microfluidic channels, the MEA could be used for flow injection chronoamperometry measurement and was capable of monitoring a gradient of concentration.

In this project, the lowest current detected at the microelectrode array was 0.5 μA, which was obtained at the surface of DNA modified electrodes in the presence of $K_3Fe(CN)_6$. The lowest analyte concentration used was 1 mmol/L and the voltamogramms obtained for this concentration were clear and noise free, at both macro and micro electrode.

7.2. CHIRAL SENSING

Electrochemical sensing was used to discriminate phenylethanol and proline enantiomers. Working on the phenylethanol enantioselective oxidation appeared to be complicated from the beginning of the project. Even though a reproducible chiral difference could be obtained the effort to promote it proved to be unsuccessful (paragraph 4.5). With the purpose of valorising the use of electrochemical chiral discrimination and microelectrode array, the initial project of chiral detection at bare gold electrode was reoriented and the electrode surfaces were modified to give them intrinsic chiral properties. As this study gave encouraging results, more efforts were put into it to make it complete, and the electrochemical impedance was introduced at this time to characterise the monolayers. This explains why the first part of the project relates to chiral selectivity using CV analyses at bare gold electrode and the last chapter describes chiral selectivity at modified electrode using impedance measurements.

Phenylethanol

In the first case, CV analysis allowed estimating quantitatively the enantioselectivity of the phenylethanol oxidation in the presence of TEMPO and (-)-sparteine in bulk solution. The final results indicated that the (-)-sparteine interacted preferentially with (-)-PE, with a CV response which was 10 % higher than the (+)-PE one at macroelectrode. The CV analyses of the PE oxidation also showed that the transition state of the enantiomers was reached at different potentials. This difference of potentials proved that, in the presence of TEMPO and sparteine catalysts, the oxidation of (+)-PE required less activation energy than the (-)-PE oxidation.

Enantioselectivity was also observable through the potential difference between the (+)- and (-)-PE peaks. The average difference was 25 mV at Pt electrode and 21 mV at Au electrode.
Moreover, the oxidation enantioselectivity could be detected using the MEA with an average current difference of 10 %.

Proline

In a second series of experiments, impedance analysis was used to detect proline enantiomers at the surface of electrodes modified by a self-assembled monolayer, where the chiral molecules tested were glutathione and cysteine.
The EIS analyses of the glutathione modified electrode did not allow the measurement of selective interactions between the monolayer and proline enantiomers. The electron transfer rates at the glutathione layer were similar in the presence of (+) and (-)-proline.
On the other hand, the presence of proline enantiomer affected the impedance responses of the cysteine modified electrode. The charge transfer resistance of the monolayer in the presence of L-proline was doubled in the presence of D-proline. The electron transfer rate was 9.50×10^{-5} $cm.s^{-1}$ for D-proline and 2×10^{-4} $cm.s^{-1}$ for L-proline. This increase confirmed the presence of preferential interactions between cysteine and the D-proline enantiomer and proved the possibility of characterising them using EIS.

7.3. DNA SURFACE MODIFICATION

Single-stranded DNA was immobilised at the surface of the macro and micro electrodes. CV and EIS analyses performed on ferricyanide showed partial coverage of the electrode surface with a very rough organisation of the molecules. The monolayer at the macroelectrode had an electron transfer rate of 8.90×10^{-5} $cm.s^{-1}$ instead of a theoretical 1.17×10^{-17} $cm.s^{-1}$. Analyses on methylene blue showed the characteristic immobilisation of the analyte at the DNA monolayer. The current measured at the modified electrode was directly proportional to the scan rate, and the electron transfer rate was slower

(1.90×10^{-5} $cm.s^{-1}$). The MEA was successfully modified with DNA and the incomplete surface coverage of the electrode could be corrected by an additional DDT modification. The CV analyses confirmed the surface was fully covered and the electron transfer was totally prevented. The impedance study corroborated those results and showed a decrease of the electron transfer rate from 1.70×10^{-4} $cm.s^{-1}$ to 4.55×10^{-5} $cm.s^{-1}$.

7.4. FURTHER WORK

Microdevice

Following the characterisation of the surface area of the microelectrode, it would be of interest to characterise its limit of detection and define the minimum analyte concentration for this current limit.

The first inflow analysis showed the capability of the microdevice to probe the variation of the analyte concentration using chronoamperometry. Further work would be to optimise the measurement set up and to assess the theoretical current expected in order to relate it to the experimental one.

A simulation of the flow velocity partition within the microchannels was built using the laminar flow module of COMSOL. The shape of the diffusion layer at the microelectrode should be studied further by coupling laminar flow with electrochemical reaction module, where the current density and flow rate together would model the diffusion layer deformation.

Proline

The selective interaction between cysteine and (D)-proline was observed using impedance analysis supported by a gold macroelectrode. This aspect can be investigated further by trying new chiral species. The proline used in this project did not have any redox properties and the chiral discrimination was detected by impedance, where the structure of the monolayer was studied, but not by CV, where the redox reaction of ferrycianate was not affected by the proline interaction with the monolayer. It would be

of interest to see if the enantioselective interactions between a chiral species with redox properties and the monolayer can be detected by both impedance and CV analyses. Man would expect that interaction of the redox analyte with the monolayer would modify the electron transfer rate and therefore affect the CV answer. Furthermore, in a permanent interest of reducing the size of the device and the amount of chemical needed, it would be relevant to perform the same analysis using the microelectrode array.

DNA

The immobilisation of DNA at the surface of microelectrode array opened a path for further biological applications such as bio-sensing and DNA labelling. The results obtained in this study are preliminary results and proved that the microelectrode array surface could be modified with DNA and that this layer could be characterise using electroanalytical impedance measurements. The layer formed at the surface of the electrode was not optimal. The organisation of the DNA at the metal surface could be improved by investigating the role of the different parameters such as pH, supporting salts, electrolytes and duration of immobilisation.

APPENDIX 1

PUBLICATIONS

"**Chiral resolution of R and S 1-phenylethanol on glassy carbon electrodes"**, Journal of Electroanalytical Chemistry 633, 57-62 (2009)

"**Microelectrode Array Supported by Microfluidic Channel for High-Throughput Sensing: Fabrication and Characterisation**", ECS Transactions, 33 (8) 221-227 (2010)

"**Microelectrode Arrays for Electroanalytical Sensing: Comparison of Electroplating and Electron-Beam Metallisation**", Electrochemistry communication, 13 (5) 414-417 (2011)

CONFERENCES

- **Analytical Research Forum** (ARF), Manchester, 25-27 July 2011. ***Poster***: "SAM Functionalised Microelectrode Array Fabrication, Electrochemical Study and Application".
- **218th ECS (Electrochemical Society) Meeting**, Las Vegas, US, 10-15 October 2010. ***Talk***: "Microelectrode Array Supported by Microfluidic Channel for High-Throughput Sensing: Fabrication and Characterisation".
- **61st Annual Meeting of the International Society of Electrochemistry,** Nice, France, Sept 2010. ***Poster***: "Microelectrode Array integrated with Microfluidics for High-Throughput Chiral Sensing".
- **42nd IUPAC World Chemistry Congress,** Glasgow, 2-7 August 2009.

- **Electrochem09',** Manchester, 16-17 September 2009. ***Poster***: "Microelectrodes arrays in microfluidic systems for chiral sensing".
- **Analytical Research Forum (ARF),** Kent, 13-15 July 2009. ***Poster***: "Micro electrode sensor arrays in microfluidic systems for high-throughput sensing".
- **59th Annual Meeting of the International Society of Electrochemistry,** Seville, Spain, 7-12 September 2008. ***Poster***: "Flow-Through Micro Electrode Array For Electrochemical Chiral Sensors".
- **Analytical Research Forum (ARF),** Hull, 21-23 July 2008. ***Poster***: "Flow-through micro electrodes arrays for high-throughput electrochemical analyses".

PRIZES

- **Alvatek Poster Prize** at the Robin Hood Interdisciplinary Network in Electrochemistry workshop, **2011**, Hull University.
- **Best 2nd Year PhD Poster Presentation** at the Chemistry Department, Durham University, 2009.
- **Analyst Poster Prize** at the Analytical Research Forum, 2009, in Kent.

MEMBERSHIPS

Royal Society of Chemistry (RSC) Membership
ElectroChemical Society (ECS) Membership
International Society of Electrochemistry (ISE) Membership
Analytical Chemistry Trust Fund (ACTF) Membership

REFERENCES

(1) A. J. Bard; L. R. Faulkner *Electrochemical Methods: Fundamentals and Applications*; John Wiley and Sons Inc, **2001**.
(2) J. Wang *Analytical Electrochemistry*; Sec. ed.; Wiley-VCH, **2000**.
(3) C. M. A. Brett; A. M. O. Brett *Electrochemistry: Principles, Methods and Applications*; Oxford Science Publications, **1993**.
(4) A. M. Bond *Broadening Electrochemical Horizons, Principles and Illustration of Voltammetric and Related Techniques*; Oxford Science Publications, **2003**.
(5) P. Protti *Introduction to Modern Voltammetry and Polarographic Analysis Techniques*; fourth ed.; Amel electrochemistry, **2001**.
(6) IUPAC *Compendium of Chemical Terminology*; Sec. ed., 1997.
(7) Bioanalytical Systems; Instruction Manual for BASi Epsilon for ELectrochemistry; http://www.basinc.com/mans/EC_epsilon/index.html; BASi: 2009.
(8) R. G. Compton; C. E. Banks *Understanding Voltammetry*; Second ed.; Imperial College Press, **2011**.
(9) K. Stulik; C. Amatore; K. Holub; V. Marecek; W. Kutner *Pure & Appl. Chem.* **2000**, *72*, 1483.
(10) M. I. Montenegro; M. A. Queiros; J. L. Daschbach *Microelectrodes: Theory and Application*; Kluwer Academic, **1990**; Vol. 197.
(11) S. Bruckenstein; J. Janiszewska *J. Electroanal. Chem.* **2002**, *538-539*, 3.
(12) R. Lenigk; H. Zhu; T-C. Lo; R. Renneberg *J. Anal. Chem.* **1999**, *364*, 66.
(13) C. Beriet; R. Ferrigno; H. H. Girault *J. Electroanal. Chem.* **2000**, *486*, 56.
(14) J. Galceran; S. L. Taylor; P. N. Bartlett *J. Electroanal. Chem.* **1999**, *476*, 132.
(15) J. Guo; E. Lindner *J. Electroanal. Chem.* **2009**, *629*, 180.
(16) R. Ferrigno; P. F. Brevet; H. H. Girault *Electrochim. Acta* **1997**, *42*, 1895.
(17) J. Heinze *Angew. Chem. Int. Ed. Engl.* **1993**, *32*, 1268.
(18) O. Ordeig; J. del Campo; F. X. Muñoz; C. E. Banks; R. G. Compton *Electroanal.* **2007**, *19*, 1973.
(19) S. K. Lucas; R. Sipcic; H. A. Stone *J. Appl. Math.* **1997**, *57*, 1615.
(20) H-P. Nirmaier; G. Henze *Electroanal.* **1997**, *9*, 619.
(21) O. González-García; C. Ariño; J. M. Díaz-Cruz; M, E. *Electroanal.* **2007**, *19*, 429.
(22) F. A. Aguiar; A. J. Gallant; M. C. Rosamond; A. Rhodes; D. Wood; R. Kataky *Electrochem. Commun.* **2007**, *9*, 879.
(23) H. J. Lee; C. Beriet; R. Ferrigno; H. H. Girault *J. Electroanal. Chem.* **2001**, *502*, 138.
(24) C. Amatore; C. Pebay; L. Thouin; A. Wang *Electrochem. Commun.* **2009**, *11*, 1269.
(25) L. E. Fosdick; J. L. Anderson; T. A. Baginski; R. C. Jaeger *Anal. Chem.* **1986**, *58*, 2750.
(26) M. Kudera; H. A. O. Hill; P. J. Dobson; P. A. Leigh; W. S. McIntire *Sensors* **2001**, *1*, 18.
(27) O. Ordeig; C. E. Banks; T. J. Davies; J. DelCampo; F. X. Muñoz; R. G. Compton *J. Electroanal. Chem.* **2006**, *592*, 126.

(28) T. J. Davies; R. G. Compton *J. Electroanal. Chem.* **2005**, *585*, 63.
(29) T. J. Davies; S. Ward-Jones; C. E. Banks; J. del Campo; R. Mas; F. X. Muñoz; R. G. Compton *J. Electroanal. Chem.* **2005**, *585*, 51.
(30) J. Guo; E. Lindner *Anal. Chem.* **2009**, *81*, 130.
(31) D. Aurbach *Nonaqueous Electrochemistry*; First ed.; CRG, **1999**.
(32) H. Lund; O. Hammerich *Organic Electrochemistry*; Fourth ed.; CRC, **2000**.
(33) K. Izutsu *Electrochemistry in Nonaqueous Solutions*; First ed.; Wiley-VCH, **2002**.
(34) A. Lasia In *Modern Aspects of Electrochemistry*; B. E. Conway, J. O-M. Bockris, R. E. White, Eds.; Kluwer Academic/Plenum **1999**; Vol. 32, p 143.
(35) G. Neuss *IB Diploma Programme: Chemistry Course Companion*; Oxford University Press, **2007**.
(36) IUPAC; Compendium of Chemical Terminology (Gold Book); http://goldbook.iupac.org/index.html 2010.
(37) S. Ahuja *Chiral separation methods for pharmaceutical and biotechnological products*; Wiley, **2010**.
(38) L. Kott; W. B. Holzheuer; M. M. Wong; G. K. Webster *J. Pharmaceut. Biomed.* **2007**, *43*, 57.
(39) J. B. Arterburn *Tetrahedron* **2001**, *57*, 9765.
(40) Y. Kashiwagi; T. Nishimura; J-I. Anzai *Electrochim. Acta* **2002**, *47*, 1317.
(41) R. A. Sheldon; I. W. C. E. Arends *Adv. Synth. Catal.* **2004**, *346*, 1051.
(42) D. Liaigre; T. Breton; E-M. Belgsir *Electrochem. Comm.* **2005**, *7*, 312.
(43) G. Palmisano; R. Ciriminna; M. Pagliaro *Adv. Synth. Catal.* **2006**, *348*, 2033.
(44) S-Y. Kishioka; T. Ohsaka; K. Tokuda *Anglais* **1998**, 343.
(45) S-Y. Kishioka; S. Ohki; T. Ohsaka; K. Tokuda *J. Electroanal. Chem.* **1998**, *452*, 179.
(46) R. Barhdadi; C. Comminges; A. Doherty; J. Nédélec; S. O'Toole; M. Troupel *J. Appl. Electrochem.* **2007**, *37*, 723.
(47) C. Comminges; R. Barhdadi; A. P. Doherty; S. O'Toole; M. Troupel *J. Phys. Chem. A* **2008**, *112*, 7848.
(48) R. Kataky; L. Murphy; A. Delcourt Lancon; S. Kalakuntla; P. Lopes *J. Electroanal. Chem.* **2009**, *633*, 57.
(49) S-Y. Kishioka; T. Ohsaka; K. Tokuda *Electrochim. Acta* **2003**, *48*, 1589.
(50) A. Deronzier; D. Lìmosin; J-C. Moutet *Electrochim. Acta* **1987**, *32*, 1643.
(51) T. Osa; Y. Kashiwagi; K. Mukai; A. Ohsawa; J. M. Bobbitt *Anglais* **1990**, 75.
(52) Y. Hahn; S. K. Song *Anal. Sci.* **1997**, *13*, 329.
(53) T. Siu; S. Yekta; A. K. Yudin *J. Am. Chem. Soc.* **2000**, *122*, 11787.
(54) F. Geneste; C. Moinet; S. Ababou-Girard; F. Solal *New J. Chem.* **2005**, *29*, 1520.
(55) G. K. Budnikov; G. Evtyugin; Y. Budnikova; V. Al'fonsov *J. Anal. Chem.* **2008**, *63*, 2.
(56) C. F. McFadden; P. S. Cremer; A. J. Gellman *Langmuir* **1996**, *12*, 2483.
(57) O. A. Hazzazi; G. A. Attard; P. B. Wells *J. Mol. Catal. A-Chem.* **2004**, *216*, 247.
(58) G. A. Attard *J. Phys. Chem. B* **2001**, *105*, 3158.
(59) A. Vargas; T. Bürgi; A. Baiker *J. Catal.* **2004**, *226*, 69.
(60) T. Osa; Y. Kashiwagi; Y. Yanagisawa; J. M. Bobbitt *J. Chem. Soc.* **1994**, 2535.
(61) Y. Yanagisawa; Y. Kashiwagi; F. Kurashima; J. Anzai; T. Osa; J. M. Bobbitt *Anglais* **1996**, 1043.
(62) A. Ramanavicius; A. Ramanaviciene; A. Malinauskas *Electrochim. Acta* **2006**, *51*, 6025.
(63) Y. Kashiwagi; S. Chiba; J-I. Anzai *J. Electroanal. Chem.* **2004**, *566*, 257.

(64) Y. Kashiwagi; Y. Yanagisawa; F. Kurashima; J. Anzai; T. Osa; J. M. Bobbitt *Chem. Commun.* **1996**, 2745.
(65) Y. Kashiwagi; K. Uchiyama; F. Kurashima; C. Kikuchi; J-I. Anzai *Chem. Pharm. Bull* **1999**, *47*, 1051.
(66) Y. Kashiwagi; F. Kurashima; C. Kikuchi; J-I. Anzai; T. Osa; J. M. Bobbitt *Tetrahedron Lett.* **1999**, *40*, 6469.
(67) Z. Ma; Q. Huang; J. M. Bobbitt *J. Org. Chem.* **1993**, *58*, 4837.
(68) S. D. Rychnovsky; T. L. McLernon; H. Rajapakse *J. Org. Chem.* **1996**, *61*, 1194.
(69) M. Kuroboshi; H. Yoshihisa; M. N. Cortona; Y. Kawakami; Z. Gao; H. Tanaka *Tetrahedron Lett.* **2000**, *41*, 8131.
(70) E. M. Belgsir; H. J. Schafer *Chem. Commun.* **1999**, 435.
(71) D. Hoppe; F. Hintze; P. Tebben; M. Paetow; H. Ahrens; J. Schwerdtfeger; P. Sommerfeld; J. Haller; W. Guarnieri; S. Kolczewski; T. Hense; I. Hoppe *Pure & Appl. Chem.* **1994**, *66*, 1479.
(72) K. B. Blodgett *J. Am. Chem. Soc.* **1935**, *57*, 1007.
(73) K. B. Blodgett; I. Langmuir *J. Am. Chem. Soc.* **1937**, *51*, 964.
(74) I. Langmuir *J. Am. Chem. Soc.* **1917**, *39*, 1848.
(75) W. C. Bigelow; D. L. Pickett; W. A. Zisman *J. Coll. Sci.* **1946**, *1*, 513.
(76) J. Sagiv *J. Am. Chem. Soc.* **1980**, *102*, 92.
(77) R. G. Nuzzo; D. L. Allara *J. Am. Chem. Soc.* **1983**, *105*, 4481.
(78) H. O. Finklea; S. Avery; M. Lynch; T. Furtsch *Langmuir* **1987**, *3*, 409.
(79) H. O. Finklea; D. A. Snider; J. Fedyk; E. Sabatani; Y. Gafni; I. Rubinstein *Langmuir* **1993**, *9*, 3660.
(80) L. H. Dubois; R.G. Nuzzo *Annu. Rev. Phys. Chem.* **1992**, *43*, 437.
(81) A. Ulman *Chem. Rev.* **1996**, *96*, 1533.
(82) F. Schreiber *J. Phys.: Condens. Matter* **2004**, *16*.
(83) C. D. Bain; E. B. Troughton; Y. T. Tao; J. Evall; G. M. Whitesides; R. G. Nuzzo *J. Am. Chem. Soc.* **1989**, *111*, 321.
(84) A. Ulman; J. E. Eilers; N. Tillman *Langmuir* **1989**, *5*, 1147.
(85) M. D. Porter; T. B. Bright; D. L. Allara; C. E. D. Chidsey *J. Am. Chem. Soc.* **1987**, *109*, 3559.
(86) L. Y. He; B. J. Xiang; Y. J. Yang *Russ. J. Electrochem.* **2004**, *40*, 849.
(87) R. A. Marcus; N. Sutin *Biochimica et Biophysica Acta (BBA) - Reviews on Bioenergetics* **1985**, *811*, 265.
(88) M. A. Rampi; G. M. Whitesides *Chem. Phys.* **2002**, *281*, 373.
(89) L. M. Tender; R. L. Worley; H. Fan; G. P. Lopez *Langmuir* **1996**, *12*, 5515.
(90) S-P. Lin; J-J. J. Chen; J-D. Liao; S. -F. Tzeng *Biomed. Microdevices* **2008**, *10*, 99.
(91) S. K. Arya; G. Chornokur; M. Venugopal; S. Bhansali *Procedia Engineering* **2010**, *5*, 804.
(92) E. Gatto; M. Venanzi; A. Palleschi; L. Stella; B. Pispisa; L. Lorenzelli; C. Toniolo; F. Formaggio; G. Marletta *Mater. Sci. Eng.: C* **2007**, *27*, 1309.
(93) J. Wang; M. Jiang; A. M. Kawde; R. Polsky *Langmuir* **2000**, *16*, 9687.
(94) Y. Wu; S. Hu *Bioelectrochem.* **2006**, *68*, 105.
(95) H. McCormick; R. McMillan; K. Merrett; F. Bensebaa; Y. Deslandes; M. A. Dubé; H. Sheardown *Colloid. Surface. B* **2002**, *26*, 351.
(96) M. Bieri; T. Bürgi *J. Phys. Chem. B* **2005**, *109*, 22476.
(97) R. Di Felice; A. Selloni; E. Molinari *The Journal of Physical Chemistry B* **2002**, *107*, 1151.
(98) R. M. Petoral; K. Uvdal *Colloid. Surface B* **2002**, *25*, 335.
(99) H. Sies *Free Radical Bio. Med.* **1999**, *27*, 916.

(100) R. Kizek; J. Vacek; L. Trnková; F. Jelen *Bioelectrochem.* **2004**, *63*, 19.
(101) S. Kanagaraja; S. Alaeddine; C. Eriksson; J. Lausmaa; P. Tengvall; A. Wennerberg; H. Nygren *J. Biomed. Mater. Res.* **1999**, *46*, 582.
(102) F. Zhao; B. Zeng; D. Pang *Electroanal.* **2003**, *15*, 1060.
(103) C. Fang; X. Zhou *Electroanal.* **2003**, *15*, 1632.
(104) M. Aihara; F. Tanaka; Y. Miyazaki; K. Takehara *Anal. Lett.* **2002**, *35*, 759.
(105) A. Zhou; Q. Xie; Y. Wu; Y. Cai; L. Nie; S. Yao *J. Colloid. Interf. Sci.* **2000**, *229*, 12.
(106) M. Bieri; T. Bürgi *Langmuir* **2005**, *21*, 1354.
(107) M. Bieri; T. Burgi *Phys. Chem. Chem. Phys.* **2006**, *8*, 513.
(108) J. Wang; P. Gründler *Electroanal.* **2003**, *15*, 1756.
(109) M. Bieri; C. Gautier; T. Burgi *Phy. Chem. Chem. Phys.* **2007**, *9*, 671.
(110) C. Gautier; T. Bürgi *J. Am. Chem. Soc.* **2006**, *128*, 11079.
(111) M. Bieri; T. Burgi *J. Phys. Chem.* **2005**, *B*, 10243.
(112) M. Bieri; T. Bürgi *Chem. Phys. Chem.* **2006**, *7*, 514.
(113) M. Matsunaga; T. Nakanishi; T. Asahi; T. Osaka *Chirality* **2007**, *19*, 295.
(114) T. M. Herne; M. J. Tarlov *J. Am. Chem. Soc.* **1997**, *119*, 8916.
(115) G. Sánchez-Pomales; L. Santiago-Rodríguez; N. E. Rivera-Vélez; C.. R. Cabrera *J. Electroanal. Chem.* **2007**, *611*, 80.
(116) A. A. Gorodetsky; A. Ebrahim; J. K. Barton *J. Am. Chem. Soc.* **2008**, *130*, 2924.
(117) K. Kasem; S. Jones *Electrode in Electrochemical Measurments*, 2008; Vol. 52.
(118) S-Y Kishioka; A. Yamada *Electrochim. Acta* **2005**, *51*, 462.
(119) M. Gerard; A. Chaubey; B. D. Malhotra *Biosens. Bioelectron.* **2002**, *17*, 345.
(120) P. H. Aubert; L. Groenendaal; F. Louwet; L. Lutsen; D. Vanderzande; G. Zotti *Synthetic Met.* **2002**, *126*, 193.
(121) S. P. Mishra; K. Krishnamoorthy; R. Sahoo; A. Kumar *J. Polym. Sci. A1* **2005**, *43*, 419.
(122) F. G. Guler; A. S. Sarac *Polym. Lett.* **2011**, *5*, 493.
(123) B. Bohl; R. Steger; R. Zengerle; P. Koltay *J. Micromech. Microeng.* **2005**, *15*, 1125.
(124) N. J. Key; V. Cindro; M. Lozano *Radiat. Phys. Chem.* **2004**, *71*, 1003.
(125) R. Feng; R. J. Farris *J. Micromech. Microeng.* **2003**, *13*, 80.
(126) M. J. Madou *Fundamentals of Microfabrication: The Science of Miniaturization*; Second ed.; CRC Press, 2002.
(127) P. Yao; G. J. Schneider; D. W. Prather *J. Microelectromech. Syst.* **2005**, *14*, 799.
(128) Negative Tone Photoresist Formulations SU8 2-25 Data Sheet *Micro-Chem, Chestech*.
(129) S. Matthews; G. Du; A. Fisher *J. Solid State Electrochem.* **2006**, *10*, 817.
(130) C. Amatore; N. Da Mota; C. Sella; L. Thouin *Anal. Chem.* **2008**, *80*, 4976.
(131) R. Feeney; S. P. Kounaves *Electroanal.* **2000**, *12*, 677.
(132) G. Grancharov; E. Khosravi; D. Wood; A. Turton; R. Kataky *Analyst* **2005**, *130*, 1351.
(133) A. L. Bogdanov *Proc. SPIE* **2000**, *3999*, 1215.
(134) G. P. Zhigal'skii; B. K. Jones *The Physical Properties od Thin Metal Films*; First ed.; CRC, 2003.
(135) N. Kanani *Electroplating: Basic Principles, Processes and Practice*; First ed.; Elsevier Science, 2005.
(136) Negative Tone Photoresist Formulations SU8 50-100 Data Sheet *Micro-Chem, Chestech*.
(137) Y. Xia; G. M. Whitesides *Angew. Chem. Int. Ed.* **1998**, *37*, 550.

(138) D. Armani; C. Liu; N. Aluru In *Micro Electro Mechanical Systems, 1999. MEMS '99. Twelfth IEEE International Conference on* **1999**, p 222.
(139) A. M. Christensen; D. A. Chang-Yen; B. K. Gale *J. Micromech. Microeng.* **2005**, *15*, 928.
(140) M. Dineen *Plasma Etching An Essential Tool for Failure Analysis*; Oxford Instruments Plasma Technology, **2004**.
(141) S. B. Brummer; A. C. Makrides *J. Electrochem. Soc.* **1964**, *111*, 1122.
(142) G. K. Batchelor *An introduction to fluid dynamics*; Third ed.; Cambridge University Press, **2000**.
(143) R. T. Kissinger; W. R. Heineman *Laboratory Techniques in Electroanalytical Chemistry*; second ed.; Marcel Dekker: New York, 1996.
(144) S. Campuzano; M. Pedrero; C. Montemayor; E. Fatás; J. M. Pingarrón *J. Electroanal. Chem.* **2006**, *586*, 112.
(145) Y. F. Xing; S. J. O'Shea; S. F. Y. Li *J. Electroanal. Chem.* **2003**, *542*, 7.
(146) R. P. Janek; W. R. Fawcett; A. Ulman *Langmuir* **1998**, *14*, 3011.
(147) V. Ganesh; S. K. Pal; S. Kumar; V. Lakshminarayanan *J. Colloid Interf. Sci.* **2006**, *296*, 195.
(148) L. V. Protsailo; W. R. Fawcett *Electrochim. Acta* **2000**, *45*, 3497.
(149) P. Diao; M. Guo; D. Jiang; Z. Jia; X. Cui; D. Gu; R. Tong; B. Zhong *J. Electroanal. Chem.* **2000**, *480*, 59.
(150) U. Srinivasan; P. A. Mieyal; J. J. Mieyal *Biochemistry* **1997**, *36*, 3199.
(151) S. G. Tajc; B. S. Tolbert; R. Basavappa; B. L. Miller *J. Am. Chem. Soc.* **2004**, *126*, 10508.
(152) D. D. Perrin; B. Dempsey; E. P. Serjeant *pKa prediction for organic acids and bases*; Chapman and Hall, **1981**.
(153) J. Raoof; R. Ojani; H. Karimi-Maleh *J. App. Electrochem.* **2009**, *39*, 1169.
(154) R. Freeman; Y. Li; R. Tel-Vered; E. Sharon; J. Elbaz; I. Willner *Analyst* **2009**, *134*, 653.
(155) S. E. Salamifar; M. A. Mehrgardi; S. H. Kazemi; M. F. Mousavi *Electrochim. Acta* **2010**, *56*, 896.
(156) S. O. Kelley; J. K. Barton; N. M. Jackson; M. G. Hill *Bioconjugate Chem.* **1997**, *8*, 31.
(157) A. Mehdinia; S. H. Kazemi; S. Z. Bathaie; A. Abdolhamid; M. Shamsipur; M. F. Mousavi *Anal. Biochem.* **2008**, *375*, 331.
(158) M. Mandelkern; J. G. Elias; D. Eden; D. M. Crothers *J. Mol. Bio.* **1981**, *152*, 153.
(159) Y. T. Long; C. Z. Li; H. B. Kraatz; J. S. Lee *Biophys. J.* **2003**, *84*, 3218.